

1

# UNIVERSITY OF BRISTOL

2

## DOCTORAL THESIS

3

---

4

# **Investigating, implementing, and creating methods for analysing large neuronal ensembles**

5

---

6

*Author:*

Thomas J. DELANEY

*Supervisors:*

Dr. Cian O'DONNELL

Dr. Michael C. ASHBY

7

*A thesis submitted in fulfillment of the requirements  
for the degree of Doctor of Philosophy*

8

*in the*

9

Biological Intelligence & Machine Learning Unit  
Department of Computer Science

10

11

July 10, 2020



## <sup>15</sup> Declaration of Authorship

<sup>16</sup> I, Thomas J. DELANEY, declare that this thesis titled, "Investigating, implementing, and  
<sup>17</sup> creating methods for analysing large neuronal ensembles" and the work presented in it are  
<sup>18</sup> my own. I confirm that:

- <sup>19</sup> • This work was done wholly or mainly while in candidature for a research degree at this  
<sup>20</sup> University.
- <sup>21</sup> • Where any part of this thesis has previously been submitted for a degree or any other  
<sup>22</sup> qualification at this University or any other institution, this has been clearly stated.
- <sup>23</sup> • Where I have consulted the published work of others, this is always clearly attributed.
- <sup>24</sup> • Where I have quoted from the work of others, the source is always given. With the  
<sup>25</sup> exception of such quotations, this thesis is entirely my own work.
- <sup>26</sup> • I have acknowledged all main sources of help.
- <sup>27</sup> • Where the thesis is based on work done by myself jointly with others, I have made  
<sup>28</sup> clear exactly what was done by others and what I have contributed myself.

<sup>29</sup>

<sup>30</sup> Signed:

<sup>31</sup> \_\_\_\_\_

<sup>32</sup> Date:

<sup>33</sup> \_\_\_\_\_



34

UNIVERSITY OF BRISTOL

35

*Abstract*

36

Engineering

37

Department of Computer Science

38

Doctor of Philosophy

39

**Investigating, implementing, and creating methods for analysing large neuronal  
ensembles**

41

by Thomas J. DELANEY

42

The Thesis Abstract is written here (and usually kept to just this page). The page is kept centered vertically so can expand into the blank space above the title too...



44

## *Acknowledgements*

45 The acknowledgments and the people to thank go here, don't forget to include your project

46 advisor...



# <sup>47</sup> Contents

<sup>48</sup>	<b>Declaration of Authorship</b>	iii
<sup>49</sup>	<b>Abstract</b>	v
<sup>50</sup>	<b>Acknowledgements</b>	vii
<sup>51</sup>	<b>1 Introduction</b>	1
<sup>52</sup>	1.1 Overview . . . . .	1
<sup>53</sup>	1.2 Modelling the fluorescence of calcium indicators . . . . .	1
<sup>54</sup>	1.3 Functional networks . . . . .	4
<sup>55</sup>	1.4 A new statistical model for capturing correlated behaviour . . . . .	5
<sup>56</sup>	<b>2 Sensitivity of the spikes-to-fluorescence transform to calcium indicator and neuron properties</b>	7
<sup>57</sup>	2.1 Introduction . . . . .	8
<sup>58</sup>	2.2 Methods . . . . .	10
<sup>59</sup>	2.2.1 Calcium dynamics model . . . . .	10
<sup>60</sup>	Photon release & capture . . . . .	12
<sup>61</sup>	2.2.2 Parameter optimisation . . . . .	13
<sup>62</sup>	Fixed parameters . . . . .	14
<sup>63</sup>	2.2.3 Julia . . . . .	14
<sup>64</sup>	2.2.4 Spike inference . . . . .	16
<sup>65</sup>	Comparing spike inference quality . . . . .	18
<sup>66</sup>	2.2.5 Perturbation analysis . . . . .	18
<sup>67</sup>	2.2.6 Signal-to-noise ratio . . . . .	18
<sup>68</sup>	2.2.7 Data sources . . . . .	19
<sup>69</sup>	2.3 Results . . . . .	19
<sup>70</sup>	2.3.1 A biophysical computational model can generate accurate fluorescence traces from spike trains . . . . .	19

73	2.3.2	Spike inference algorithms perform similarly on real data compared with time series simulated from the model . . . . .	20
74	2.3.3	Relative effects of various buffers to the fluorescence signal . . . . .	21
75	2.3.4	Spike inference accuracy is sensitive to indicator properties, and likely varies within and between cells . . . . .	22
76	2.3.5	Single spike inference accuracy drops for high firing rates, but firing rate itself can be estimated from mean fluorescence amplitude . . . . .	27
77	2.4	Discussion . . . . .	29
81	<b>3</b>	<b>Functional networks expand across anatomical boundaries as correlation timescale increases</b>	<b>33</b>
82	3.1	Introduction . . . . .	34
83	3.2	Data . . . . .	35
84	3.2.1	Brain regions . . . . .	35
85	3.2.2	Video recordings . . . . .	36
86	3.3	Methods . . . . .	36
87	3.3.1	Binning data . . . . .	36
88	3.3.2	Correlation coefficients . . . . .	37
89		Total correlations, $r_{SC}$ . . . . .	37
90		Shuffled total correlations . . . . .	38
91		Separating Correlations & Anti-correlations . . . . .	38
92	3.3.3	Conditioning on behavioural data . . . . .	38
93		Linear regression . . . . .	38
94		Elastic net regularisation . . . . .	39
95		Conditional covariance . . . . .	39
96		Measures of conditional correlation . . . . .	40
97	3.3.4	Information Theory . . . . .	41
98		Entropy $H(X)$ . . . . .	41
99		Maximum entropy limit . . . . .	41
100		Mutual Information $I(X; Y)$ . . . . .	42
101		Variation of Information $VI(X, Y)$ . . . . .	44
102		Measuring entropies & mutual information . . . . .	44
103	3.3.5	Network analysis . . . . .	44
104		Correlation networks . . . . .	44

106	Rectified correlations . . . . .	45
107	Sparsifying data networks . . . . .	45
108	Communities . . . . .	45
109	Weighted configuration model . . . . .	46
110	Sparse weighted configuration model . . . . .	46
111	Spectral rejection . . . . .	46
112	Node rejection . . . . .	47
113	Community detection . . . . .	48
114	<b>3.3.6 Clustering Comparison</b> . . . . .	48
115	Adjusted Rand Index . . . . .	48
116	Clusterings as random variables . . . . .	49
117	Information based similarity measures . . . . .	50
118	Information based metrics . . . . .	50
119	Comparing detected communities and anatomical divisions . . . . .	51
120	<b>3.4 Results</b> . . . . .	51
121	<b>3.4.1 Average correlation size increases with increasing time bin width</b> . . . . .	52
122	<b>3.4.2 Goodness-of-fit for Poisson and Gaussian distributions across increasing time bin widths</b> . . . . .	54
123	<b>3.4.3 Differences between and inter- and intra- regional correlations decrease with increasing bin width</b> . . . . .	54
124	<b>3.4.4 Connected and divided structure in correlation based networks reduces in dimension with increasing bin width</b> . . . . .	57
125	<b>3.4.5 Detecting communities in correlation based networks</b> . . . . .	58
126	<b>3.4.6 Functional communities resemble anatomical division at short timescales</b>	61
127	<b>3.4.7 Conditional correlations &amp; signal correlations</b> . . . . .	61
128	<b>3.4.8 Absolute correlations and negative rectified correlations</b> . . . . .	66
129	<b>3.5 Discussion</b> . . . . .	67
130	<b>4 A simple two parameter distribution for modelling neuronal activity and capturing neuronal association</b>	73
131	<b>4.1 Introduction</b> . . . . .	74
132	<b>4.2 Data</b> . . . . .	75
133	<b>4.2.1 Experimental protocol</b> . . . . .	75
134	<b>4.3 Methods</b> . . . . .	76

139	4.3.1	Binning data . . . . .	76
140	4.3.2	Number of <i>active</i> neurons . . . . .	76
141	4.3.3	Moving windows for measurements . . . . .	76
142	4.3.4	Fano factor . . . . .	78
143	4.3.5	Probability Distributions suitable for modelling ensemble activity . . . . .	78
144	Association . . . . .	78	
145	Binomial distribution . . . . .	79	
146	Beta-binomial distribution . . . . .	79	
147	Conway-Maxwell-binomial distribution . . . . .	80	
148	4.3.6	Fitting . . . . .	82
149	4.3.7	Goodness-of-fit . . . . .	84
150	4.4	Results . . . . .	84
151	4.4.1	Increases in mean number of active neurons and variance in number of active neurons at stimulus onset in some regions . . . . .	84
152	Primary visual cortex . . . . .	85	
153	Hippocampus . . . . .	85	
154	Thalamus . . . . .	85	
155	4.4.2	Conway-Maxwell-binomial distribution is usually a better fit than binomial or beta-binomial . . . . .	85
156	4.4.3	Conway-Maxwell-binomial distribution captures changes in association at stimulus onset . . . . .	90
157	4.4.4	Replicating stimulus related quenching of neural variability . . . . .	90
158	4.5	Discussion . . . . .	92
162	<b>5</b>	<b>Studies with practical limitations &amp; negative results</b>	<b>95</b>
163	5.1	Dynamic state space model of pairwise and higher order neuronal correlations	96
164	5.2	A multiscale model for hierarchical data applied to neuronal data . . . . .	96
166	<b>6</b>	<b>Discussion</b>	<b>99</b>
167	<b>Bibliography</b>		<b>107</b>

# 168 List of Figures

169	2.1 A: Example spike train (blue) and the corresponding GCaMP6s fluorescence	
170	trace (green), data replotted from (Berens et al., 2018). Inset shows zoomed	
171	section of traces to highlight slow decay of GCaMP6s fluorescence relative	
172	to spike time intervals. B: Schematic diagram of the neuron calcium and	
173	GCaMP computational model. C: Good visual match of data fluorescence	
174	trace (green) and model simulated fluorescence (orange) in response to an	
175	identical spike train (blue). . . . .	9
176	2.2 A: Workflow to compare spike inference for real versus simulated fluores-	
177	cence data. B: True positive rates achieved by three different spike inference	
178	algorithms when applied to observed spike trains, and simulated spike trains.	
179	Data points overlaid as blue circles. The performance is similar from real	
180	and simulated data for each of the algorithms. . . . .	21
181	2.3 <b>Calcium Buffering Dynamics</b> (a) The proportions of bound and free cal-	
182	cium concentrations within a cell, with the associated spike train. (b)-(f) The	
183	dynamics of the concentration of (b) excited indicator bound calcium, (c) in-	
184	dicator bound calcium, (d) immobile endogenous buffer bound calcium, (e)	
185	mobile endogenous buffer bound calcium, and (f) free calcium in response to	
186	an action potential at $\sim 23.2\text{s}$ . . . . .	23
187	2.4 (a) An example trace for each of the five pairs of values used for the binding	
188	and unbinding rates of the fluorescent calcium indicator. (b) The signal-to-	
189	noise ratio of the modelled fluorescence traces using each of the four per-	
190	turbed value pairs, and the experimental value. The SNRs for the value pairs	
191	perturbed downward are lower than that for the unperturbed value pair or	
192	the higher value pairs. (c) The true-positive rates of the deconvolution al-	
193	gorithm's predictions when inferring from the observed data, and inferring	
194	from modelled traces using the perturbed and experimental values. . . . .	25

195	2.5 (a) An example trace for each of the five perturbed values for the concentration of fluorescent calcium indicator. The top two traces are produced by the lower perturbed values, the middle trace is produced by the experimental value, and the lowest two traces are produced when using the higher perturbed values. (b) The signal-to-noise ratio of the modelled fluorescence traces using each of the four perturbed values, and the experimental value. Extreme perturbations of the concentration either above or below the experimental level lowered the SNR. (c) The true-positive rates of the deconvolution algorithm's predictions when inferring from the observed data, and inferring from modelled traces using the perturbed and experimental values. We found that the algorithms performs equally badly on the two most extreme values, and performs equally well on the experimental value, and the next higher perturbed value. . . . .	26
208	2.6 (a) An example trace for each of the five perturbed values for the concentration of immobile endogenous buffer. (b) The signal-to-noise ratio of the modelled fluorescence traces using each of the four perturbed values, and the experimental value. The lower values for the immobile buffer produce the same SNR as the experimental value. But the higher perturbed values produce fluorescence traces with a lower SNR. (c) The true-positive rates of the deconvolution algorithm's predictions when inferring from the observed data, and inferring from modelled traces using the perturbed and experimental values. . . . .	28
217	2.7 <b>Simulating fluorescence traces at different firing rates</b> Example modelled traces created using simulated spike trains with a mean firing rate of 1Hz (left column), 5Hz (middle column), and 10Hz (right column). Note the difference in amplitude with different mean firing rates. . . . .	29
221	2.8 <b>Inference quality and <math>\Delta F/F_0</math> vs Firing rate</b> (left) The spike inference accuracy when applied to 30 traces created using simulated spike trains with mean firing rates of 1, 5, and 10 Hz. (right) The mean $\Delta F/F_0$ across those 30 traces for each frequency. . . . .	30
225	3.1 <b>Probe Locations:</b> The locations of the probes in each of the three mouse brains (Stringer et al., 2019). . . . .	36

227	3.2 <b>Entropy Limit:</b> The upper limit on entropy of binned spike count data as 228 a function of the maximum observed spike count. The orange line is the 229 analytical maximum. The blue line is the entropy of samples with $N = 1000$ 230 data points taken from the discrete uniform distribution. . . . .	42
231	3.3 (A) An example of the correlation coefficients between two different pairs 232 of cells, one where both cells are in the same brain region (intra-regional 233 pair), and one where both cells are in different brain regions (inter-regional 234 pair). The correlation coefficients have been measured using different time 235 bin widths, ranging from 5ms to 3s. Note the increasing amplitude of the 236 correlations with increasing bin width. (B) A raster plot showing the spike 237 times of each pair of cells. . . . .	52
238	3.4 Mean correlation coefficients measured from pairs of 50 randomly chosen 239 neurons. (A) All possible pairs, (B) positively correlated pairs, and (C) neg- 240 atively correlated pairs. (D) Mean and standard error of $\chi^2$ test statistics for 241 Poisson and Gaussian distributions fitted to neuron spike counts. . . . .	53
242	3.5 (Left)The mean intra-region and inter-region correlations using all possible 243 pairs of $\sim 500$ neurons, spread across 9 different brain regions. (Right) 244 Courtesy of Stringer et al. (2019), mean inter-regional (out-of-area) correla- 245 tion coefficients vs mean intra-regional (within-area) correlation coefficients 246 for a bin width of 1.2s. Note that the intra-regional coefficients are higher in 247 each case. . . . .	55
248	3.6 The mean intra-regional correlations (coloured dots) and mean inter-regional 249 correlations (black dots) for a given region, indicated on the x-axis, for dif- 250 ferent time bin widths. Each black dot represents the mean inter-regional 251 correlations between the region indicated on the x-axis and one other region. 252 (A) shows these measurements when we used a time bin width of 5ms. (B) 253 shows these measurements when we used a time bin width of 1s. Note that 254 the difference between the mean inter-regional correlations and mean intra- 255 regional correlations is smaller for 1s bins. . . . .	56
256	3.7 Mean inter-regional (main diagonal) and intra-regional (off diagonal) corre- 257 lation coefficients. (A) Shows these measurements when spike times were 258 binned using 5ms time bins. (B) Shows the same, using 1s time bins. Note 259 that the matrices are ordered according to the main diagonal values, therefore 260 the ordering is different in each subfigure. . . . .	57

261	3.8 The number of dimensions in the $k$ -partite and connected structure in the cor-	
262	relation based networks beyond the structure captured by a sparse weighted	
263	configuration null network model (see section 3.3.5), shown for different time	
264	bin widths. Note that the $k$ -partite structure disappears for time bin width	
265	greater than 200ms for all three subjects. The dimension of the connected	
266	structure reduces with increasing bin width for 2 of the 3 subjects (top row). . . . .	59
267	3.9 (A-B) Correlation matrices with detected communities indicated by white	
268	lines. Each off main diagonal entry in the matrix represents a pair of neu-	
269	rons. Those entries within a white square indicate that both of those neurons	
270	are in the same community as detected by our community detection proce-	
271	dure. Matrices shown are for 5ms and 1s time bin widths respectively. Main	
272	diagonal entries were set to 0. (C-D) Matrices showing the anatomical dis-	
273	tribution of pairs along with their community membership. Entries where	
274	both cells are in the same region are given a colour indicated by the colour	
275	bar. Entries where cells are in different regions are given the grey colour also	
276	indicated by the colour bar. . . . .	60
277	3.10 (A) The variation of information is a measure of distance between cluster-	
278	ings. The distance between the anatomical ‘clustering’ and community de-	
279	detection ‘clustering’ increases with increasing time bin width. (B) The ad-	
280	justed Rand index is a normalised similarity measure between clusterings.	
281	The anatomical and community detection clusterings become less similar as	
282	the time bin width increases. . . . .	62
283	3.11 Comparing the components of the total covariance across different values for	
284	the time bin width. We observed a consistent increase in $E[\text{cov}(X, Y Z)]$ as	
285	the time bin width increased. But we saw different trends for $\text{cov}(E[X Z], E[Y Z])$	
286	for each mouse. . . . .	63
287	3.12 Comparing the components of the total covariance across different values for	
288	the time bin width. We saw a consistent increase in $\rho_{X,Y Z}$ as the time bin	
289	width increased in all three subjects. But we saw different trends in $\rho_{\text{signal}}$ for	
290	each of the subjects. . . . .	64

291	3.13 Matrices showing the regional membership of pairs by colour, and the com-	
292	munities in which those pairs lie. (A-B) Detected communities and regional	
293	membership matrix for network based on rectified spike count correlation	
294	$\rho_{X,Y Z}$ , using time bin widths of 0.005s and 1s respectively. (C-D) Detected	
295	communities and regional membership matrix for network based on rectified	
296	signal correlation $\rho_{\text{signal}}$ , using time bin widths of 0.005s and 1s respectively.	65
297	3.14 Distance and similarity measures between the anatomical division of the neu-	
298	rons, and the communities detected in the network based on the spike count	
299	correlations $\rho_{X,Y Z}$ . (A) The variation of information is a ‘distance’ mea-	
300	sure between clusterings. The distance between the anatomical ‘clustering’	
301	and the community clustering increases as the time bin width increases. (B)	
302	The adjusted Rand index is a similarity measure between clusterings. The	
303	detected communities become less similar to the anatomical division of the	
304	cells as the time bin width increases. . . . .	66
305	3.15 Distance and similarity measures between the anatomical division of the neu-	
306	rons, and the communities detected in the network based on the signal cor-	
307	relations $\rho_{\text{signal}}$ . (A) The variation of information is a ‘distance’ measure be-	
308	tween clusterings. The distance between the anatomical ‘clustering’ and the	
309	community clustering increases as the time bin width increases. (B) The ad-	
310	justed Rand index is a similarity measure between clusterings. The detected	
311	communities become less similar to the anatomical division of the cells as	
312	the time bin width increases. . . . .	67
313	3.16 (A-B) Absolute correlation matrices with detected communities indicated by	
314	white lines. These communities are based on the absolute value of the total	
315	correlation between each pair of cells. Those entries within a white square in-	
316	dicate that both of those neurons are in the same community. Matrices shown	
317	are for 5ms and 1s time bin widths respectively. Main diagonal entries were	
318	set to 0. (C-D) Matrices showing the anatomical distribution of pairs along	
319	with their community membership. Regional membership is indicated by the	
320	colour bar. (E) Variation of information between the anatomical division of	
321	the cells, and the detected communities. (F) Adjusted Rand index between	
322	the anatomical division, and the detected communities. . . . .	68

323	3.17 (A-B) Sign reversed rectified correlation matrices with detected communities indicated by white lines. Those entries within a white square indicate that both of those neurons are in the same community. Matrices shown are for 5ms and 1s time bin widths respectively. Main diagonal entries were set to 0. (C-D) Matrices showing the anatomical distribution of pairs along with their community membership. Regional membership is indicated by the colour bar. (E) Variation of information between the anatomical division of the cells, and the detected communities. (F) Adjusted Rand index between the anatomical division, and the detected communities. . . . .	69
332	4.1 Figures showing the over-dispersion possible for a beta-binomial distribution relative to a binomial distribution. Parameters are shown in the captions. . .	80
334	4.2 Figures showing (A) the under-dispersion and (B) over-dispersion permitted by the COMb distribution relative to a binomial distribution. (C) illustrates that the $p$ parameter of the COMb distribution does not correspond to the mean of the distribution, as it does for the binomial and beta-binomial distributions. (D) shows a heatmap for the value of the Kullback-Liebler divergence between the COMb distribution and the standard binomial distribution with same value for $n$ , as a function of $p$ and $\nu$ . Parameters are shown in the captions. . . . .	83
342	4.3 (A) Raster plot showing the spikes fired by 33 randomly chosen neurons in the primary visual cortex. (B-C) (B) average and (C) variance of the number of active neurons, measured using a sliding window 100ms wide, split into 100 bins. The midpoint of the time interval for each window is used as the timepoint (x-axis point) for the measurements using that window. The grey shaded area indicates the presence of a visual stimulus. The opaque line is an average across the 160 trials that included a visual stimulus of any kind. We can see a transient increase in the average number of active neurons and the variance of this number, followed by a fluctuation and another increase. .	86

351	4.4 (A) Raster plot showing the spikes fired by 33 randomly chosen neurons in 352       the hippocampus. (B-C) (B) average and (C) variance of the number of active 353       neurons, measured using a sliding window 100ms wide, split into 100 bins. 354       The midpoint of the time interval for each window is used as the timepoint (x- 355       axis point) for the measurements using that window. The grey shaded area 356       indicates the presence of a visual stimulus. The opaque line is an average 357       across the 160 trials that included a visual stimulus of any kind. We can see 358       a transient increase in the average number of active neurons and the variance 359       of this number at stimulus onset. . . . .	87
360	4.5 (A) Raster plot showing the spikes fired by 33 randomly chosen neurons in 361       the thalamus. (B-C) (B) average and (C) variance of the number of active 362       neurons, measured using a sliding window 100ms wide, split into 100 bins. 363       The midpoint of the time interval for each window is used as the timepoint (x- 364       axis point) for the measurements using that window. The grey shaded area 365       indicates the presence of a visual stimulus. The opaque line is an average 366       across the 160 trials that included a visual stimulus of any kind. We can 367       see in immediate increase at stimulus onset, a subsequent fall, and another 368       sustained increased until the stimulus presentation ends. . . . .	88
369	4.6 (A) An example of the binomial, beta-binomial, and Conway-Maxwell-binomial 370       distributions fitted to a sample of neural activity. The Conway-Maxwell- 371       binomial distribution is the best fit in this case. The histogram shows the 372       empirical distribution of the sample. The probability mass function of each 373       distribution is indicated by a different coloured line. (B) Across all samples 374       in all trials, the proportion of samples for which each fitted distribution was 375       the the best fit. The Conway-Maxwell-binomial distribution was the best fit 376       for 93% of the samples taken from V1 using a bin width of 1ms. . . . .	89

377	4.7 (A) We fit a Conway-Maxwell-binomial distribution to the number of active	
378	neurons in 1ms time bins of a 100ms sliding window. We did this for all	
379	trials with a visual stimulus and took the average across those trials. We	
380	see a transient drop in value for the distribution's $\nu$ parameter at stimulus	
381	onset. This shows an increase in association between the neurons. (B) We	
382	measured the correlation coefficient between the spike counts of all possible	
383	pairs of neurons in the same sliding window. The took the average of those	
384	coefficients. We also did this for every visually stimulated trial, and took	
385	the average across trials. The increase in association is not reflected with an	
386	increase in average correlation. . . . .	91
387	4.8 (A) The mean Fano factor of the spike counts of the cells in the primary visual	
388	cortex. Means were taken across cells first, then across trials. There was a	
389	significant decrease in the Fano factors immediately after stimulus onset. (B)	
390	The mean Fano factor of the spike counts of the cells in the motor cortex. No	
391	significant change in measurements at any point. . . . .	92

# 392 List of Tables

393	2.1	Fixed parameters A table of the parameters fixed before optimising the model. The values of these parameters could be changed to model different fluorescent calcium indicators. . . . .	15
394	4.1	Details of the different bin width and analysis window sizes used when binning spike times, and analysing those data. . . . .	77
395	4.2	Relative dispersion of the COMb distribution, and association between Bernoulli variables as represented by the value of the $\nu$ parameter. . . . .	82
396	4.3	Proportion of samples for which each distribution was the best fit, grouped by bin width. The COMb distribution is the best fit most of the time. . . . .	90
397			
398			
399			
400			
401			



<sup>402</sup> **List of Abbreviations**

**COMb** Conway-Maxwell-binomial (distribution)

**OASIS** Online active set method to infer spikes

**SNR** Signal to noise ratio



<sup>403</sup> **List of Symbols**

$[Ca^{2+}]$	Free calcium concentration	mol
$[BCa]$	Fluorescent indicator bound calcium	mol
$[ECa]$	Endogenous mobile buffer bound calcium	mol
$[ImCa]$	Immobile mobile buffer bound calcium	mol
$[BCa^*]$	excited fluorescent indicator bound calcium	mol
$k_{X_f}$	binding (affinity) rate	$s^{-1}$
$k_{X_b}$	unbinding (dissociation) rate	$s^{-1}$



*For/Dedicated to/To my...*



405 **Chapter 1**

406 **Introduction**

407 **1.1 Overview**

408 Since Hodgkin and Huxley's squid experiments featuring a single axon (Hodgkin and Hux-  
409 ley, 1939), to more recent research with spike sorted data from  $\sim 24000$  neurons from 34  
410 brain regions from 21 mice (Allen et al., 2019), the number of neurons contributing to elec-  
411 trophysiological datasets has been growing. Recording methods using two-photon calcium  
412 imaging have also been used to extract data from populations containing over 10000 neurons  
413 (Peron et al., 2015). This dramatic growth in the number of neurons available for analysis  
414 requires a dramatic change in analysis methods. In this project, we have attempted to address  
415 some of the difficulties in collecting data from these large ensembles, and analysing these  
416 data.

417 Our next chapter describes a biophysical model for the fluorescence trace induced by  
418 a given spike train in a cell containing a fluorescent calcium indicator. Our third chapter  
419 describes our investigations into the correlated activity across different regions of a mouse  
420 behaving spontaneously. We applied a novel community detection method (Humphries et  
421 al., 2019) from network science to correlation based networks of neurons, and observed  
422 differences in the structure of these correlations at different timescales. In our fourth chapter,  
423 we detail a new statistical model for the number of neurons spiking in a neuronal ensemble  
424 at any given moment. With this model, we attempted to capture correlated activity in a new  
425 way.

426 **1.2 Modelling the fluorescence of calcium indicators**

427 To focus on calcium imaging for a start, a neuron that contains a fluorescent calcium indicator  
428 in its cytoplasm will fluoresce when bombarded with photons. The amount that the cell  
429 will fluoresce is dependent on the concentration of fluorescent indicator within the cell, and

430 the concentration of calcium within the cell. When a neuron fires an action potential, the  
431 influx of free calcium ions causes an increase in fluorescence when those ions bond with the  
432 fluorescent indicator and those bounded molecules are bombarded with photons. After the  
433 action potential, as calcium is extruded from the cell the fluorescence returns to a baseline  
434 level. This is the basic mechanism of fluorescent calcium indicator based imaging.

435 This method has some advantages over electrophysiology as measure of neuronal ensemble  
436 activity. Many of the problems with electrophysiology are within the processes used to  
437 isolate spikes in the extracellular voltage readings, and assign these spikes to individual cells.  
438 These processes are collectively called ‘spike sorting’. A comparison of many different spike  
439 sorting algorithms found that these algorithms only agreed on a fraction of cases (Buccino  
440 et al., 2019). Furthermore, because electrodes measure extracellular voltage, neurons that do  
441 not spike will not be detected. Isolating individual neurons is easier and more reliable when  
442 using calcium imaging data, because cells will emit a baseline level of fluorescence when not  
443 firing action potentials. Another advantage is that calcium imaging sites can be re-used for  
444 weeks for longitudinal studies (Chen et al., 2013). One of the methods of delivering the flu-  
445 orescent indicator is by adeno-associated viruses, consequently there can be problems with  
446 indicator gradients around the infection site, and expression levels will change in individual  
447 cells over weeks (Tian et al., 2009; Chen et al., 2013). This delivery method can also cause  
448 cell pathology, and nuclear filling (Zariwala et al., 2012), but these problems can be solved by  
449 using lines of transgenic mice (Dana et al., 2014). The fluorescence signal itself can serve as a  
450 good indicator of cell activity, but similarly to electrophysiology, the aim of calcium imaging  
451 is often spike detection.

452 If the imaging data is collected at a high enough frequency, and the signal-to-noise ratio  
453 of the fluorescence trace is high enough, it should be possible to infer the spike times to some  
454 level of accuracy. For example, the calmodulin based indicator GCaMP6s has a sufficiently  
455 high signal-to-noise ratio that isolated action potentials can be detected and inferred (Chen  
456 et al., 2013). Many spike inference algorithms exist (Vogelstein et al., 2010; Pnevmatikakis  
457 et al., 2016; Friedrich and Paninski, 2016; Pnevmatikakis et al., 2013; Pnevmatikakis et al.,  
458 2014; Deneux et al., 2016; Greenberg et al., 2018), and some of these can perform both cell  
459 isolation and spike detection simultaneously (Vogelstein et al., 2010; Pnevmatikakis et al.,  
460 2016; Pnevmatikakis et al., 2014; Deneux et al., 2016). But the relationship between spik-  
461 ing and fluorescence change is not fully understood. For example, the fluorescent indicator  
462 will act like an additional calcium buffer within the cell cytoplasm and will compete with  
463 the other endogenous buffers to bind with free calcium ions. Therefore, the concentration of

464 those endogenous buffers, and the binding dynamics of those buffers will have an effect on  
465 the change in fluorescence in response to an action potential. Furthermore, the binding dy-  
466 namics of the fluorescent indicator itself will have an effect on the change in fluorescence. For  
467 example, the GCaMP series of fluorescence indicators are based on the calcium buffer pro-  
468 tein calmodulin. This protein has four binding sites, whose affinities interact non-linearly.  
469 But most of the spike inference algorithms model the fluorescence as a linear function of a  
470 calcium trace, and they model this calcium trace as a first or second order autoregression with  
471 a pulse input to represent action potentials. Deneux et al. (2016) developed a spike inference  
472 algorithm with a bit more biological inspiration, but this amounted to a very similar process.  
473 While this autoregression idea appears to be a reasonable approximation, the algorithms that  
474 use this approximation are outperformed by the most recently published spike inference algo-  
475 rithm (Greenberg et al., 2018). This algorithm does take into account the binding dynamics  
476 of both the endogenous buffers and fluorescent calcium indicator, and the concentrations of  
477 free calcium, indicator, and endogenous buffer within the cell cytoplasm. The performance  
478 of this algorithm shows that there is value in more biologically inspired models of fluorescent  
479 calcium indicators.

480 In light of the growing popularity of two-photon calcium imaging, and the lack of biolog-  
481 ically inspired spike inference algorithms (Greenberg et al. developed their spike inference  
482 algorithm in parallel to our work), we decided to develop a biologically inspired model for  
483 fluorescent calcium indicator fluorescence. The idea being that our model would take a spike  
484 train, or simply spike times, provided by the user, and return the fluorescence trace that would  
485 be induced by this spike train or spike times. The model contains parameters for concentra-  
486 tions of indicator and endogenous buffers, as well as affinity and unbinding rates for these  
487 buffers. There are also parameters for the baseline concentration of free calcium in the cell  
488 cytoplasm, and the cell radius (as a means for calculating the cell volume). With this model,  
489 we hoped that experimentalists would be able to test out different calcium indicators on the  
490 types of spike trains that they expect to encounter. This way they could decide ahead of time  
491 which indicator suited their situation best. Since the output of our model is a fluorescence  
492 trace, the spike inference models mentioned above can be applied to the modelled fluores-  
493 cence. This means that the model could also be used to benchmark the performance of these  
494 spike inference algorithms, and to investigate the impact of variations in the model on spike  
495 inference accuracy.

### 496 1.3 Functional networks

497 We have outlined some of the advantages that calcium imaging has over electrophysiology.  
498 But electrophysiology is more useful in some situations. One particular drawback for two-  
499 photon calcium imaging is that usually it can only be used for imaging near to the surface  
500 of the brain. This problem can be solved by removing the tissue around the area to be im-  
501 aged, and custom building a two-photon microscope Dombeck et al., 2010. Imaging with  
502 three (or presumably more) photons may solve this problem in the future (Ouzounov et al.,  
503 2017). A better option for reading activity from neurons beyond the surface of the brain is to  
504 use Neuropixels probes (Jun et al., 2017). These probes can be used to read from thousands  
505 of neurons simultaneously in many different areas of the brain (Allen et al., 2019; Stringer  
506 et al., 2019; Steinmetz, Carandini, and Harris, 2019; Steinmetz et al., 2019). This brings us  
507 to another problem for which we require new innovations in our analysis methods. Specif-  
508 ically, analysing correlated behaviour in neural ensembles consisting of neurons from many  
509 different brain regions.

510 Until the invention of new technologies such as the Neuropixels probes, most elec-  
511 trophysiology datasets read from neurons in only one or two regions. Therefore most of  
512 the research on interactions between neurons in different regions is limited to two regions  
513 (Wierzyński et al., 2009; Patterson et al., 2014; Girard, Hupé, and Bullier, 2001). In chapters  
514 3 and 4 we used datasets with neurons from 9 and 5 different brain regions respectively.

515 In light of recent findings based on correlated behaviour showing that spontaneous be-  
516 haviours explain activity in many different parts of the brain that would otherwise be regarded  
517 as noise (Stringer et al., 2019), that satiety is represented brain wide (Allen et al., 2019), and  
518 that exploratory and non-exploratory states are represented in the amygdala (Gründemann  
519 et al., 2019), it was clear that state representation or motor control had an influence on cor-  
520 related behaviour in areas of the brain not usually associated with these tasks. Also, given  
521 differences in timescales of fluctuations in different brain regions (Murray et al., 2014), and  
522 different timescales for event representation in different brain regions (Baldassano et al.,  
523 2017), we decided to investigate brain wide correlated behaviour at timescales ranging from  
524 5ms up to 3s.

525 We started off measuring the correlations in spike counts between individual neurons in  
526 our ensemble. These measurements induced a weighted undirected graph where each node  
527 represented a neuron, and the weight of each edge was the strength of the correlation be-  
528 tween the neurons represented by the nodes at either end of that edge. In order to put the

529 neurons into groups with correlated behaviour, we applied a novel community detection al-  
530 gorithm (Humphries et al., 2019) to this graph. We repeated this analysis for timescales  
531 from milliseconds to seconds. Bear in mind that our correlation based graph was completely  
532 agnostic of the anatomical regions in which our cells resided. We then compared our corre-  
533 lated communities to their anatomy at each timescale. In this way, we used a novel method,  
534 never applied neuronal data before, to analyse the makeup of correlated communities across  
535 different regions at different timescales.

## 536 1.4 A new statistical model for capturing correlated behaviour

537 Many important findings have been made by measuring the correlations between binned  
538 spike counts, but there are some problems with this method of analysis. Firstly, the width  
539 of the bins used to bin spike times into spike counts has an effect on the magnitude of the  
540 correlations measured. Using a short bin width can cause your measurements to be artificially  
541 small (Cohen and Kohn, 2011). This may not be an issue if one is considering relative size of  
542 correlations when using the same bin width, but it is still not ideal. Secondly, while pairwise  
543 correlations can capture most of the information in a small network (up to 40 cells) of highly  
544 correlated cells (Schneidman et al., 2006), a model based on pairwise correlations alone will  
545 fail to capture the activity of larger ( $\sim 100$  cells) networks, higher order correlated activity  
546 is required (Ganmor, Segev, and Schneidman, 2011). One problem with these higher order  
547 correlations is that they may be defined in different ways (Staude, Grün, and Rotter, 2010).  
548 Furthermore if we want to include them in a model this usually involves greatly increasing the  
549 number of parameters to fit, which increases the dimension of the parameter space leading  
550 to the ‘curse of dimensionality’. Some models attempt to sidestep these problems while  
551 still capturing higher-order correlations. These models attempt to capture the relationship  
552 between each individual neuron in the ensemble, and the ensemble as a whole. Okun et al  
553 (2015) called the strength of this relationship the ‘population coupling’, and demonstrated  
554 that this quantity can predict an individual neuron’s response to optogenetic stimulation of  
555 the whole ensemble. They also showed that this quantity was an indicator of the neuron’s  
556 synaptic connectivity (Okun et al., 2015). With the ‘population tracking model’, O’Donnell  
557 et al. (2016) linked the probability of firing an action potential for each individual neuron  
558 with the distribution of the number of active neurons. This allowed model fitting for a large  
559 number of neurons, as well as calculation of full pattern probabilities, and population entropy  
560 (O’Donnell et al., 2017).

561 In this work, we also aimed to capture correlated behaviour between the neurons in a  
562 neuronal ensemble without measuring correlations directly. Correlation coefficients capture  
563 the linear component of the relationship between two random variables, but will not mea-  
564 sure any relationship beyond linearity. Also, measuring correlation coefficients using short  
565 timebins can be difficult for neuronal data (Cohen and Kohn, 2011). We decided to abandon  
566 correlation, and we aimed to quantify a more general concept of association by modelling  
567 the number of active neurons in the ensemble using a Conway-Maxwell-binomial (COMb)  
568 distribution (Kadane, 2016).

569 The COMb distribution is a probability distribution over the number of successes in a  
570 sequence of Bernoulli trials, where these trials can be associated in some way. The COMb  
571 distribution is an extension of the standard binomial distribution, with an additional parameter  
572 to model association between the Bernoulli variables. Using this additional parameter the  
573 distribution can capture positive association, where the Bernoulli variables tend to take the  
574 same value, negative association, where the Bernoulli variables tend to take opposite values,  
575 or no association i.e. the standard binomial distribution.

576 We fit a COMb distribution to spike sorted electrophysiological data taken from five  
577 different regions in the brain of an awake mouse exposed to visual stimuli (Steinmetz et al.,  
578 2019). We examined whether or not a model based on the COMb distribution was able to  
579 capture changes in the number of active neurons in these neuronal ensembles in response to  
580 the stimuli. We also investigated the relationship between the changes as captured by the  
581 COMb model and the change in neural variability as measured by Churchland et al. in their  
582 famous paper (Churchland et al., 2010).

583 Our overall aim was to investigate some of the challenges in analysing large ensembles  
584 of neurons present today. That included collecting the data to analyse (via calcium imaging),  
585 and subsequently analysing these data. We felt that this was a worthwhile project because  
586 the size of datasets, in terms of numbers of neurons and data collected, is growing rapidly.  
587 Consequently these challenges will only become greater unless they are addressed. This is  
588 our attempt at addressing them.

589 **Chapter 2**

590 **Sensitivity of the**  
591 **spikes-to-fluorescence transform to**  
592 **calcium indicator and neuron**  
593 **properties**

594 *Abstract*

595 Fluorescent calcium indicators such as GCaMP are widely used to monitor neuronal activity.  
596 However the relationship between the fluorescence signal and the underlying action potential  
597 firing is poorly understood. This lack of knowledge makes it difficult for experimenters  
598 to decide between different indicator variants for a given application. We addressed this  
599 problem by studying a basic biophysical model of calcium dynamics in neuronal soma. We  
600 fit the model parameters to publicly available data where GCaMP6s fluorescence and whole-  
601 cell electrophysiological recordings were made simultaneously in the same single neurons.  
602 We systematically varied the model's parameters to characterise the sensitivity of spike train  
603 inference algorithms to the calcium indicator's main biophysical properties: binding rate,  
604 dissociation rate, and molecular concentration. This model should have two potential uses:  
605 experimental researchers may use it to help them select the optimal indicator for their desired  
606 experiment; and computational researchers may use it to generate simulated data to aid design  
607 of spike inference algorithms.

608 **2.1 Introduction**

609 Although fluorescent calcium indicators such as GCaMP are widely used to monitor neuronal  
610 activity, the relationship between the fluorescence signal and the underlying action potential  
611 firing is imperfect. The fluorescence signal has a low signal-to-noise ratio, and most indica-  
612 tors' kinetics are slow relative to the millisecond-timescale dynamics of the membrane volt-  
613 age (example in figure 2.1A). This makes spike inference difficult. Furthermore, the effects  
614 of the indicator and cell properties on the fluorescence signal are unknown. For example,  
615 genetically encoded indicators can accumulate within neurons over weeks and months (Chen  
616 et al., 2013). Studies using calcium-sensitive fluorescent dyes have shown that indicator con-  
617 centration has substantial effects on the spike-to-fluorescence relationship (Maravall et al.,  
618 2000). Therefore spike rates inferred from GCaMP fluorescence signals may give mislead-  
619 ing results if comparing across imaging sessions. More generally, the poor understanding of  
620 the spike-to-fluorescence transform means experimenters may not know whether to trust the  
621 outputs of spike train inference methods in any given application.

622 Spike trains are usually inferred from the time series of intensity values of one pixel of the  
623 fluorescence image, where the pixel is located at the cell's soma. The problems of identifying  
624 these pixels, and inferring spikes from their time series can solved separately or together.  
625 When attempting to infer spikes, the fluorescence trace is modelled as a linear combination of  
626 calcium concentration dynamics, a baseline calcium concentration, and some Gaussian noise.  
627 The calcium concentration dynamics are modelled as an autoregressive process of degree 1  
628 or 2 with a pulse input corresponding to the spike train, or the number of spikes fired in a  
629 time step. The model includes no dynamics for the fluorescent indicator itself. Furthermore,  
630 in order to make this model into an easily solvable linear programming problem the number  
631 of spikes fired in a timestep is not restricted to non-negative integers but to arbitrary non-  
632 negative values (Vogelstein et al., 2010; Pnevmatikakis et al., 2016; Friedrich and Paninski,  
633 2016; Pnevmatikakis et al., 2013; Pnevmatikakis et al., 2014). More biologically inspired  
634 spike inference models do exist (Deneux et al., 2016), but their fundamentals are very similar.  
635 In this work, we investigated the effect of changing dynamics and buffer concentrations on  
636 the accuracy of the inference algorithms based on these models.

637 The aim of this project was to model the fluorescence traces produced by a fluorescent  
638 calcium indicator in a neuron soma resulting from a specific spike train, given calcium indi-  
639 cator parameters such as binding rate, dissociation rate, and molecular concentration. Such

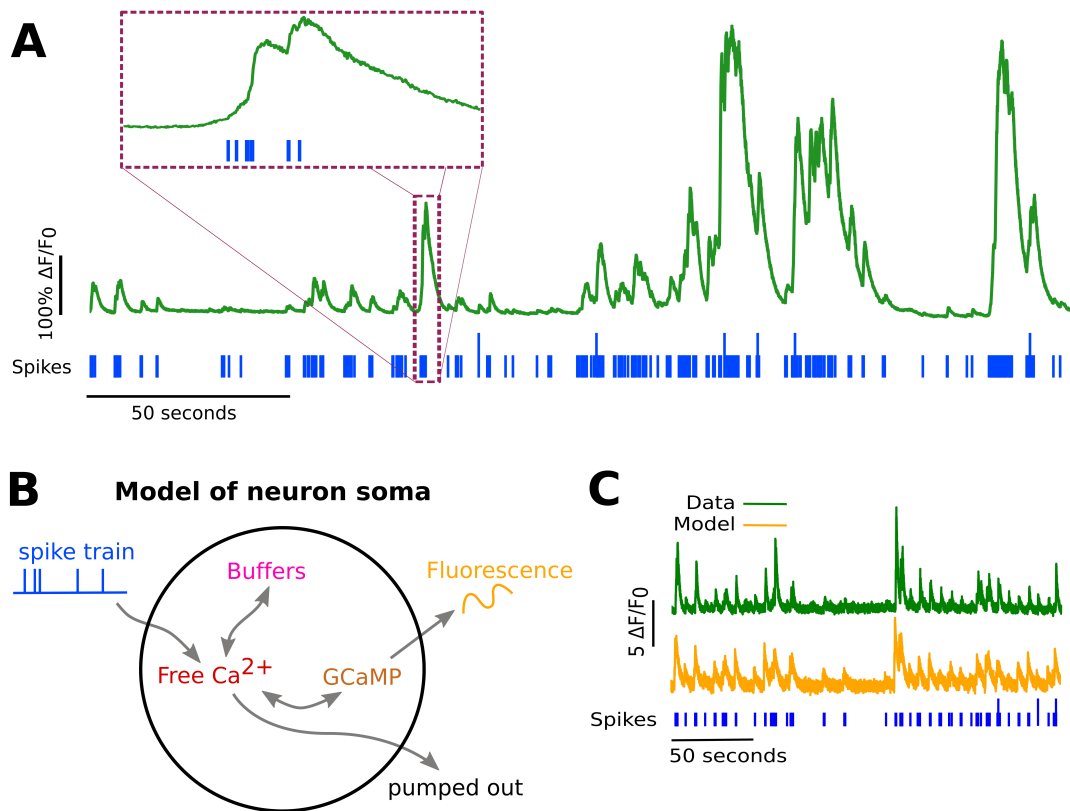


FIGURE 2.1:

A: Example spike train (blue) and the corresponding GCaMP6s fluorescence trace (green), data replotted from (Berens et al., 2018). Inset shows zoomed section of traces to highlight slow decay of GCaMP6s fluorescence relative to spike time intervals.

B: Schematic diagram of the neuron calcium and GCaMP computational model.

C: Good visual match of data fluorescence trace (green) and model simulated fluorescence (orange) in response to an identical spike train (blue).

640 a model would allow benchmarking of various spike inference algorithms, and enable under-  
641 standing of how indicator characteristics affect the quality of spike train inference.

642 The model we developed consisted of free calcium, fluorescent indicator molecules, and  
643 mobile and immobile endogenous calcium buffers. The indicator molecules which were  
644 bound to a calcium molecule could be either excited, i.e. able to release a photon, or relaxed.  
645 In order to reproduce the noise inherent in the data collection, we modelled the release of  
646 photons from the excited indicator bound calcium as a stochastic process.

647 The fluorescence traces produced by the simulation were calibrated to reproduce the  
648 signal-to-noise ratio observed in experimental data. Previously published spike inference  
649 algorithms were then used to infer spike trains from the experimental fluorescence traces and  
650 the modelled fluorescence traces. The parameters of the model were then varied in order to  
651 determine the effect on the system dynamics and the effects on spike inference.

## 652 2.2 Methods

### 653 2.2.1 Calcium dynamics model

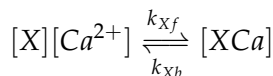
654 We wrote a biophysical model of the calcium dynamics within a cell soma. When a neu-  
655 ron fires an action potential, voltage-dependent calcium ion-channels open up that allow a  
656 current of  $\text{Ca}^{2+}$  to flow into the neuron (Koch, 1999). The increase in the free calcium ion  
657 concentration inside of the cell, along with changes in the concentration of potassium and  
658 sodium, causes the change in cell membrane potential, which must be depolarised. The de-  
659 polarising process consists of free calcium ions leaving the cell through open ion channels,  
660 or binding to molecules within the cell called buffers, or calcium storage by organelles such  
661 as the endoplasmic reticulum. A diagram illustrating the cell, its channels, and its buffers  
662 can be seen in figure 2.1A. There are several different types of calcium buffer, each with  
663 different dynamics and different concentrations within different types of excitable cell. The  
664 fluorescent calcium indicator is another calcium buffer, with the useful property that when it  
665 is bound to a calcium ion, the bound molecule may become excited by a photon and release  
666 a photon in return. This is what creates the fluorescence. After the action potential has taken  
667 place, the free calcium concentration within the cell will return to a baseline level (Maravall  
668 et al., 2000).

669 We modelled the the dynamics of five molecular concentrations,

- 670 • Free calcium ion concentration,  $[\text{Ca}^{2+}]$

- 671     • Fluorescent indicator bound calcium,  $[BCa]$
- 672     • Endogenous mobile buffer bound calcium,  $[ECa]$
- 673     • Endogenous immobile buffer bound calcium,  $[ImCa]$
- 674     • Excited buffered calcium,  $[BCa^*]$

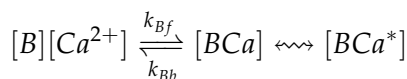
The term ‘buffering’ refers to free calcium ions coming into contact with buffer molecules and binding together. Diagrammatically:



675 where  $[X]$  represents any buffer molecule, and  $k_{X_f}$  and  $k_{X_b}$  represent the binding and un-  
 676 binding (dissociation) rates in units of per molar concentration per second ( $M^{-1} s^{-1}$ ) and per  
 677 second ( $s^{-1}$ ) respectively. The speed of this chemical reaction is determined by the binding  
 678 and unbinding rates.

679 There are a number different endogenous buffers in any neuron. Which buffers are  
 680 present, and the buffers’ concentrations vary from cell to cell. In order to capture the ef-  
 681 fects of mobile and immobile endogenous buffers without introducing several parameters,  
 682 they were modelled as two buffers. One representing mobile buffers and the other represent-  
 683 ing immobile buffers. Each with their own binding and unbinding rates.

The fluorescent calcium indicator behaves similarly to the other calcium buffers. The calcium is buffered by the indicator in the same way. But an indicator bound calcium molecule can become excited by absorbing the energy from a photon. An excited indicator bound calcium molecule can then release a photon to go back to its ‘relaxed’ state.



684 The released photons are captured by a photon collector. This gives us the fluorescence trace.  
 685 Ignoring the baseline level of free calcium in a neuron, the system of equations we used  
 686 to model all of these interactions is as follows:

$$\begin{aligned} \frac{d[Ca^{2+}]}{dt} = & k_{Bb}[BCa] + k_{Eb}[ECa] + k_{Imb}[ImCa] \\ & - k_{Bf}[B][Ca^{2+}] - k_{Ef}[E][Ca^{2+}] - k_{Imf}[Im][Ca^{2+}] \\ & + \beta([Ca_0^{2+}] - [Ca^{2+}]) \end{aligned} \quad (2.1)$$

$$\frac{d[BCa]}{dt} = k_{Bf}[B][Ca^{2+}] - k_{Bb}[BCa] + r[BCa^*] - e[BCa] \quad (2.2)$$

$$\frac{d[ECa]}{dt} = k_{Ef}[E][Ca^{2+}] - k_{Eb}[ECa] \quad (2.3)$$

$$\frac{d[ImCa]}{dt} = k_{Imf}[Im][Ca^{2+}] - k_{Imb}[ImCa] \quad (2.4)$$

$$\frac{d[BCa^*]}{dt} = \eta[BCa] - r[BCa^*] \quad (2.5)$$

687 where  $[Ca_0^{2+}]$  is the baseline calcium concentration within the cell soma,  $\beta$  is a rate defining  
688 how quickly free calcium enters or leaves the cell in the absence of an action potential,  $\eta$   
689 is the excitation rate for indicator bound calcium,  $r$  is the photon release rate for the excited  
690 indicator bound calcium, and  $f$  and  $b$  are used to indicate the forward and backward rates  
691 for chemical reactions respectively. The excitation rate defines the proportion of indicator  
692 bound calcium that becomes excited at each time step. The photon release rate defines the  
693 proportion of excited indicator bound calcium that releases a photon and returns to its relaxed  
694 state at each time step. An action potential is modelled as a discontinuous increase in the free  
695 calcium concentration to an appropriate value (Maravall et al., 2000).

696 Note that each of the three pairs of binding and unbinding terms in the first equation has a  
697 corresponding pair in one of the subsequent three equations. Binding removes a free calcium  
698 molecule and adds a bound calcium molecule, and unbinding does the opposite.

699 When using this model to simulate a fluorescence trace, the system of equations above are  
700 first solved over a period of 25s without action potentials. This lets each of the five tracked  
701 chemical concentrations reach their steady state. Then we use the given spike train and the  
702 parameters to model the fluorescence trace.

703 Note that since the model has no spatial component, the mobile and immobile buffers  
704 only differ in their binding and unbinding rates.

## 705 Photon release & capture

706 We used a simple model for the photon release. The number of photons released at each time  
707 step was controlled by the number of excited indicator bound calcium molecules in the cell  
708 and a parameter called the ‘release rate’. The release rate is an optimised free parameter of  
709 the model.

710 As for the photon capture, in two-photon excitation microscopy the photons scattered  
711 by the fluorescent indicator get scattered in all directions. Therefore the number of photons  
712 detected is stochastic. This made the process for capturing photons the natural source of  
713 noise in the system. The number of photons captured, and therefore the intensity of the

714 fluorescence, is modelled using a binomial distribution. The number of photons released was  
715 used as the number of trials. The probability of success, or ‘capture rate’ was a free parameter  
716 of the model that we optimised.

717 **2.2.2 Parameter optimisation**

718 The free parameters of the model are as follows:

719 **Calcium rate,  $\beta$**  Controls how quickly the concentration of free calcium will be driven to  
720 the baseline concentration.

721 **Capture rate,  $p$**  The average proportion of photons captured by the photon detector.

722 **Excitation rate,  $\eta$**  The number of indicator bound calcium molecules that become excited  
723 by photon bombardment at each time step.

724 **Release rate,  $r$**  The number of excited indicator bound calcium molecules that release a  
725 photon at each time step.

726 To optimise the free parameters given a fluorescence trace, we applied the following proce-  
727 dure:

- 728 1. The frequency power spectrum of the trace was measured.
- 729 2. The power spectrum was smoothed using a boxcar smoother (aka. sliding average, box  
730 smoother).
- 731 3. The log of the smoothed power spectrum was measured.
- 732 4. Use the model to create a modelled fluorescence trace.
- 733 5. Apply steps 1, 2, and 3 to the modelled fluorescence trace.
- 734 6. Calculate the root mean squared difference between the log power of the actual fluo-  
735 rescence trace, and the log power of the modelled fluorescence trace.
- 736 7. Calculate the root mean squared difference between the actual fluorescence trace and  
737 the modelled fluorescence trace.
- 738 8. Use an optimisation algorithm to reapply this process, attempting to minimize the sum  
739 of the two root mean squared differences at each iteration.

740 Using the root mean squared difference of the log power spectra as part of the objective  
741 function forces the model to match the noise frequency of the actual fluorescence. Using  
742 the root mean squared difference of the traces themselves forces the model to match the  
743 amplitude of the fluorescence trace more accurately.

744 In order to minimise the objective function, a suite of meta-heuristic optimisation (aka.  
745 black-box optimisation) algorithms were implemented on each of the traces in the dataset.  
746 These methods were chosen because they don't require a gradient for the objective function  
747 (gradient-free) and they are particularly useful for minimising stochastic objective functions  
748 like the one we used here. The free parameters were optimised for each individual fluores-  
749 cence trace. The most successful method for each trace was recorded. The method that was  
750 most often successful was probabilistic descent, and the second most successful method was  
751 generating set search. Both of these methods are examples of pattern search. These two  
752 methods were the best optimisers on about 75% of the traces in the dataset.

753 Although this optimisation procedure minimises the value of the optimisation function,  
754 the value never reaches zero for a number of reasons. Firstly, the fluorescence traces carry low  
755 frequency fluctuations that cannot be captured by the model. Secondly, the model assumes  
756 that the process of calcium binding to the fluorescent indicator is linear in time (see equation  
757 1), but there are more complicated dynamics involved here. Fluorescent calcium indicators  
758 are often built upon the calcium binding protein called 'calmodulin'. This protein has four  
759 calcium binding sites. These sites are locally split into two pairs. Each pair has a different  
760 affinity for calcium, and the affinity of the binding sites is affected by the occupancy of  
761 the other binding sites (Kilhoffer et al., 1992). So the calcium to calcium indicator binding  
762 process is non-linear, but the model does not take this into account.

763 **Fixed parameters**

764 As well as the optimised parameters mentioned in section 2.2.2, the model also has thirteen  
765 fixed parameters. Please see table 2.1 for details of these parameters and their values. In  
766 an application of the model, these parameters can be changed in order to model any given  
767 fluorescent calcium indicator.

768 **2.2.3 Julia**

769 The programming language used to write and execute the model was 'Julia'. Julia is a dy-  
770 namic programming language designed for technical computing. Julia was designed specif-  
771 ically to provide a convenient high-level dynamic language similar to MATLAB, or Python,

Parameter	Description	Value	Source
baseline	The baseline concentration of free calcium within the cell soma	$4.5 \times 10^{-8} M$	(Maravall et al., 2000)
cell radius	The radius of the soma (assumed to be spherical)	$10^{-5} M$	(Fiala and Harris, 1999)
endogenous	The concentration of endogenous mobile buffer within the cell soma	$10^{-4} M$	(Faas et al., 2011)
frequency	The frequency at which the spike trains are sampled.	100Hz	
immobile	The concentration of endogenous immobile buffer within the cell soma	$7.87 \times 10^{-5} M$	(Bartol et al., 2015)
indicator	The concentration of fluorescent indicator within the cell soma	$10^{-4} M$	(Maravall et al., 2000)
$k_{Bb}$	The unbinding rate of the fluorescent calcium indicator	$160 s^{-1}$	(Bartol et al., 2015)
$k_{Bf}$	The binding rate of the fluorescent calcium indicator	$7.77 \times 10^8 s^{-1} M^{-1}$	(Bartol et al., 2015)
$k_{Eb}$	The unbinding rate of the endogenous mobile buffer	$10^4 s^{-1}$	(Bartol et al., 2015)
$k_{ef}$	The binding rate of the endogenous mobile buffer	$10^8 s^{-1} M^{-1}$	(Bartol et al., 2015)
$k_{Imb}$	The unbinding rate of the endogenous immobile buffer	$524 s^{-1}$	(Bartol et al., 2015)
$k_{Imf}$	The binding rate of the endogenous immobile buffer	$2.47 \times 10^8 s^{-1} M^{-1}$	(Bartol et al., 2015)
peak	The increase in free calcium concentration within the cell induced by an action potential	$2.9 \times 10^{-7} M$	(Maravall et al., 2000)

TABLE 2.1: **Fixed parameters** A table of the parameters fixed before optimising the model. The values of these parameters could be changed to model different fluorescent calcium indicators.

772 with improved performance. Julia’s type system and Julia’s direct interfaces with C and  
773 Fortran allow this aim to be achieved (Bezanson et al., 2012). The Julia version of the  
774 ‘Sundials’ package for ODE solving was used to solve the system of equations above. The  
775 BlackBoxOptim.jl package for Julia was used to perform the optimisation.

776 **2.2.4 Spike inference**

777 We used spike inference algorithms to compare the quality of spike inference using the mod-  
778 elled traces to the quality of spike inference using the observed traces. We also used the  
779 spike inference algorithms to assess the effect of parameter perturbation on the spike infer-  
780 ence. Three algorithms were used:

781 **Constrained non-negative deconvolution algorithm (aka Pnevmatikakis algorithm)** This  
782 algorithm uses a constrained version of non-negative Weiner deconvolution to infer a  
783 calcium signal and a ‘spiking activity signal’ from the fluorescence trace (Vogelstein  
784 et al., 2010; Pnevmatikakis et al., 2016). The spiking activity signal is a non-negative  
785 vector of real numbers reflecting the cell’s activity rather than an actual spike train. We  
786 inferred a spike train by choosing an optimised threshold for the spiking activity sig-  
787 nal. Whenever the spiking activity signal exceeded that threshold, an action potential  
788 was inferred. The threshold was optimised by minimising the difference between the  
789 number of spikes observed and the number of spikes predicted.

790 **ML-Spike algorithm** This algorithm uses a generalised version of the Viterbi algorithm to  
791 return the spike train that maximises the likelihood of producing the given fluorescence  
792 trace. The Viterbi algorithm is an algorithm for estimating the most likely sequence  
793 of hidden states resulting in a sequence of observed states in a discrete-time finite-  
794 state Markov process (Forney, 1973). In this case, each hidden state is defined by the  
795 presence or absence of an action potential, and each observed state is the value of the  
796 fluorescence trace at each time step. This algorithm assumes that the concentration of  
797 calcium within the cell will decay to a drifting baseline, rather than a fixed baseline  
798 (Deneux et al., 2016).

799 **Online Active Set method to Infer Spikes (OASIS)** This algorithm is once again based on  
800 an auto-regressive model of the fluorescence trace, but can be generalised to any or-  
801 der. The algorithm itself is a generalisation of the pool adjacent violators algorithm  
802 (PAVA) that is used in isotonic regression. The OASIS algorithm works through the

803 fluorescence trace from beginning to end, this combined with the speed of the algo-  
804 rithm means that it could be used for real-time online spike inference (Friedrich and  
805 Paninski, 2016). Given a fluorescence trace, the algorithm will return the most likely  
806 spike train and an inferred denoised fluorescence signal.

807 In order to quantify the quality of spike inference for a given algorithm, we ran that algorithm  
808 on all of the fluorescence traces in dataset number eight of the spike finder datasets. Then we  
809 measured some binary classification measures on the results. These measures included

- 810     ● Accuracy
- 811     ● True positive rate (aka recall, sensitivity, hit rate)
- 812     ● True negative rate (aka specificity)
- 813     ● Precision
- 814     ● Negative predicted value
- 815     ● False negative rate (aka miss rate)
- 816     ● False positive rate (aka fall-out)
- 817     ● False discovery rate
- 818     ● False omission rate

819 In making these measurements, we allowed a tolerance of two subsequent time bins for spike  
820 prediction. For example, the spike train data is a vector of 0s and 1s, with one element for  
821 each time bin. A ‘0’ denotes inactivity, a ‘1’ denotes the presence of at least one action  
822 potential. The inferred spike trains produced by the spike inference algorithms take the same  
823 form. In our analysis, if a spike appeared in the inferred spike train up to two time frames  
824 after a spike in the observed spike train, that spike was considered correctly inferred i.e. a true  
825 positive. However, once a spike in the inferred spike train was matched to a spike from the  
826 observed spike train, the inferred spike could not be matched to another observed spike. To  
827 illustrate, if two spikes were inferred in the two time bins following an isolated observed  
828 spike, the first inferred spike was considered correctly inferred, but the second inferred spike  
829 was considered incorrectly inferred, i.e. a false positive.

830 The most useful measure was the true positive rate. This is because the spiking is sparse  
831 and this measurement is sensitive to the number of spikes observed and inferred, but is not  
832 affected by the true negative or false negative rates. After optimising the parameters for each

833 fluorescence trace we measured the spike inference quality for the observed fluorescence  
834 traces, and compared this to the spike inference quality for the modelled traces.

835 When measuring the spike inference quality for higher frequency spike train (1 – 10Hz),  
836 we used the accuracy as our binary classification measure. At these frequencies the variance  
837 of the fluorescence trace was much higher than for sparser spiking regimes, therefore we  
838 wanted to take into account the number of false negatives inferred by the algorithm.

839 **Comparing spike inference quality**

840 In order to compare spike inference quality we had to use methods for comparing samples.  
841 When comparing the true positive rate distributions arising from two different datasets, or  
842 two different algorithms on the same dataset, we compared the distributions using a paired  
843 t-test.

844 **2.2.5 Perturbation analysis**

845 In order to measure the sensitivity of spike inference to changes in a given model parameter,  
846 we perturbed the parameter and compared the quality of spike inference with the perturbed  
847 parameters to the quality of spike inference with the experimental or optimised parameters.  
848 In order to maximise the possibility of observing a difference due to the perturbation, we  
849 perturbed the chosen parameter by a relatively large amount. For example, the experimen-  
850 tal value for the molar concentration of the fluorescent indicator within the cell was  $10^{-4}\text{M}$   
851 (Maravall et al., 2000). The perturbed values used for this parameter were  $10^{-2}\text{M}$ ,  $10^{-3}\text{M}$ ,  
852  $10^{-5}\text{M}$ , and  $10^{-6}\text{M}$ . The quality of the inference was compared by measuring the true posi-  
853 tive rate for each perturbed value and using a t-test to compare the distributions of the results.

854 This analysis was performed firstly without any optimisation of the free parameters for  
855 use with the perturbed parameters. Then the analysis was performed after the optimised  
856 parameters for each perturbed value were calculated.

857 **2.2.6 Signal-to-noise ratio**

858 To assess the effect of perturbation on the modelled traces, we measured and compared the  
859 signal to noise ratio (SNR) on each of the modelled traces. We calculated the SNR as the  
860 peak change in fluorescence divided by the standard deviation of the baseline fluctuation of  
861 the fluorescence trace (Tada et al., 2014). We measured these values by running the model  
862 on a spike train consisting a long period of inactivity followed by one action potential. We  
863 ran the model on this spike train one hundred times. We then measured the mean change

864 in fluorescence and standard deviation of baseline activity across the one hundred modelled  
865 fluorescence traces, and calculated the SNR.

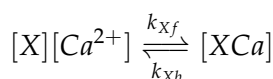
866 **2.2.7 Data sources**

867 All of the data used in this project was sourced from the ‘Spike Finder’ project ([spikefinder.codeneuro.org](http://spikefinder.codeneuro.org)).  
868 The data consisted of a collection of datasets with simultaneously measured fluorescence  
869 traces and action potentials (Berens et al., 2018).

870 **2.3 Results**

871 **2.3.1 A biophysical computational model can generate accurate fluorescence  
872 traces from spike trains**

To study the relationship between action potential firing and calcium fluorescence, we built a computational model of calcium dynamics in a neuronal soma. The model consisted of four dynamic variables: the concentration of free calcium, two types of endogenous buffer, and the calcium-sensitive fluorescent indicator. Each of the buffers and the indicator could independently bind and unbind with calcium. These reactions were modelled as



873 where  $X$  is the buffer concentration and  $Ca^{2+}$  is the calcium concentration. Each species  
874 could therefore exist in two states: either bound with calcium or unbound. To model the  
875 imaging process, we also added a third, excited state to the indicator. When in the calcium-  
876 bound state, the indicator could be converted to an excited state, corresponding to the absorp-  
877 tion of a photon. The rate of this excitation process could be interpreted as the intensity of  
878 the light illuminating the sample. Once excited, the species decayed back to the unexcited  
879 state at a fixed rate, corresponding to the spontaneous emission of photons. The total emitted  
880 fluorescence signal was interpreted as proportional to this de-excitation flux. To represent  
881 experimental noise in the photon capture process, we drew a random number of captured  
882 photons at each time step from a binomial distribution, parameterised by a number  $p$  that  
883 corresponds to the mean fraction of released photons that are captured.

884 The model had 17 parameters in total describing the molecules’ concentrations and re-  
885 action rates (Methods). We set 13 of these parameters to values from the literature. The  
886 remaining 4 parameter values we fit to publicly-available data (Berens et al., 2018), briefly

explained as follows (see Methods for full details). Single neurons from acute rat cortical slices expressing GCaMP6f were imaged with two-photon microscopy while the membrane potentials of the somata of the same neurons were simultaneously recorded via whole-cell patch clamp electrophysiology. In this dataset, the electrical recordings give unambiguous information about neurons' spike times. To do the parameter fitting, we feed these spike trains as inputs to the computational model. After running, the model returns a simulated fluorescence trace. We aimed to find the model parameter values that give the best match between this simulated fluorescence trace and the real fluorescence time series recorded in the corresponding neuron. To do this we used a suite of optimisation procedures to jointly fit both the real neuron's fluorescence time series and power spectrum, which capture complementary information about the spikes-to-fluorescence mapping (Methods). We performed the fitting procedure independently for each of the 20 neurons in the spikefinder dataset (<http://spikefinder.org>). After fitting, the model produced realistic-looking fluorescence time series (Figure 2.1).

901 **2.3.2 Spike inference algorithms perform similarly on real data compared with  
902 time series simulated from the model**

903 Researchers often pass the fluorescence time series through a spike inference tool before per-  
904 forming further statistical analyses. These spike inference algorithms take the fluorescence  
905 trace as input and attempt to estimate the neuronal spike train that triggered them (Vogelstein  
906 et al., 2010; Pnevmatikakis et al., 2016; Friedrich and Paninski, 2016; Pnevmatikakis et al.,  
907 2013; Pnevmatikakis et al., 2014; Deneux et al., 2016). Part of our motivation for building  
908 this model was to allow us to ask the questionon-linearitiesproperties of the cell and the cal-  
909 cium indicator affect the quality of spike inference? In order to trust the conclusions from  
910 our model, we should first be confident that spike inference from our simulated fluorescence  
911 traces is similar to that from the real data. To test this we passed each of the simulated fluores-  
912 cence traces through three previously published spike inference algorithms, quantified their  
913 performance against the ground-truth electrophysiology data, repeated the procedure for the  
914 real calcium fluorescence time series, and compared the accuracy of the inference processes  
915 in all cases. The *true positive rate*, also known as the *recall*, the *sensitivity*, or the *probabi-*  
916 *lity of detection* of spike inference varied across the three inference algorithms we tried (p  
917 value and statistical test here). The constrained non-negative matrix deconvolution algorithm  
918 (Pnevmatikakis et al., 2016) (CNMD algorithm) correctly detected approximately 45% of the

919 true spikes, the OASIS algorithm (Friedrich and Paninski, 2016) correctly detected approx-  
 920 imately 35% of the true spikes, and the ML spike algorithm (Deneux et al., 2016) correctly  
 921 detected approximately 15% of the true spikes (see figure 2.2). Notably, for two of the three  
 922 inference algorithms, the quality of inference was also fairly consistent for individual spike  
 923 trains, not just the group means ( $p > 0.05$ , paired t-test). This demonstrates that the models  
 924 were generating fluorescence time series that were similarly difficult to decode as the real  
 925 data, in ways that were not specific to any one inference algorithm. This is evidence that the  
 models captured real aspects of the spikes-to-fluorescence transform.

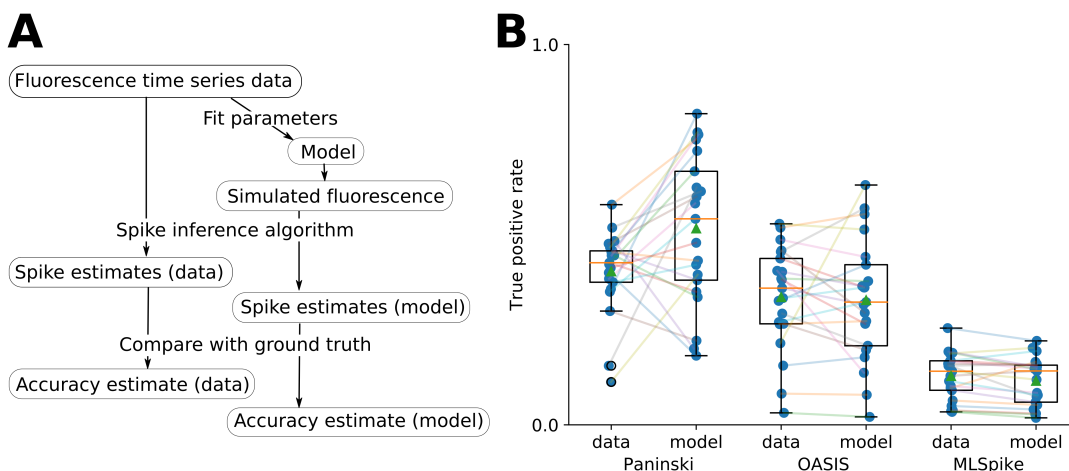


FIGURE 2.2:  
 A: Workflow to compare spike inference for real versus simulated fluorescence data.  
 B: True positive rates achieved by three different spike inference algorithms when applied to observed spike trains, and simulated spike trains. Data points overlaid as blue circles. The performance is similar from real and simulated data for each of the algorithms.

926

### 927 2.3.3 Relative effects of various buffers to the fluorescence signal

928 One of the benefits of computational models over laboratory experiments is that we can  
 929 observe all the variables in the simulation to gain insight into the system's dynamics, which  
 930 can be difficult to do in the lab. We plotted the concentrations of the various species over  
 931 time for a version of the model fit to one data set, in response to the same train of spikes used  
 932 for fitting (figure 2.3). Figure 2.3a shows the absolute values of the species concentrations,  
 933 summed. Consistent with experimental estimates (Maravall et al., 2000), only a small fraction  
 934 ( $\sim 0.1\%$ ) of calcium is free and unbound to any buffer. Of the bound calcium, the vast  
 935 majority, ( $\sim 96\%$ ) is bound to the GCaMP indicator. The two types of endogenous buffer

936 are bound to the remaining calcium ( $\sim 4\%$ ). An influx of calcium from a single spike adds  
937 very little to the total calcium, in relative terms (red line in Figure 3a).

938 When calcium entered the model neuron it was rapidly buffered (Bartol et al., 2015).  
939 However the relative fractions of which buffer molecules bound to the influxed calcium was  
940 dynamic, and changed over time. Figure 2.3 (b-f) shows the time course of the various  
941 species over time in response to a calcium influx event from a single action potential. Cru-  
942 cially, the indicator  $[BCa]$  competed with the endogenous buffers  $[ImCa]$  and  $[ECa]$  – all  
943 three bind calcium on similar timescales. This implies that the timecourse and amplitude of  
944 the  $[BCa]$  variable will also depend on the binding rates and availabilities of the endogenous  
945 buffers. For example if we decreased the concentration of an endogenous buffer, we might  
946 expect both a faster rise time and greater peak amplitude of the  $[BCa]$  signal in response to  
947 a calcium influx event. The slowest component of the decay had a similar time constant for  
948  $[BCa]$ ,  $[ImCa]$  and  $[ECa]$ , which in turn matched the  $[Ca]$  extrusion time constant in our  
949 model ( $\sim 6.29 \times 10^{-22} \text{Ms}^{-1}$ ). This implies that the buffers and the indicator had reached  
950 a dynamic equilibrium and were jointly tracking the free calcium concentration as calcium  
951 was slowly extruded from the cell.

952 Interestingly the excited bound calcium species ( $[BCa^*]$ ) showed a qualitatively different  
953 timecourse in response to a calcium influx event. This concentration is subject to the added  
954 ‘excitation and release’ dynamic, where a certain proportion of the concentration absorbs the  
955 energy from an incoming photon and goes into an ‘excited state’ at each time step. A certain  
956 proportion of the concentration releases a photon and reverts to a ‘relaxed state’ at each  
957 timestep also. This means that the excited bound calcium lags behind the bound calcium  
958 trace. We could think of the excited bound calcium trace as a low pass filtered version of the  
959 bound calcium trace.

960 **2.3.4 Spike inference accuracy is sensitive to indicator properties, and likely  
961 varies within and between cells**

962 The above results imply that the fluorescence signal depends on the relative properties of  
963 both GCaMP and the endogenous buffers. We next used the model to directly ask how  
964 sensitive spike inference was to these components. We focused on three key parameters that  
965 likely vary from cell to cell and experiment to experiment: GCaMP binding kinetics, GCaMP  
966 concentration, and endogenous buffer concentration.

967 Several variants of GCaMP itself have been made that differ in calcium binding kinetics,  
968 baseline fluorescence, fluorescence efficiency, and other factors. For example, GCaMP6f has

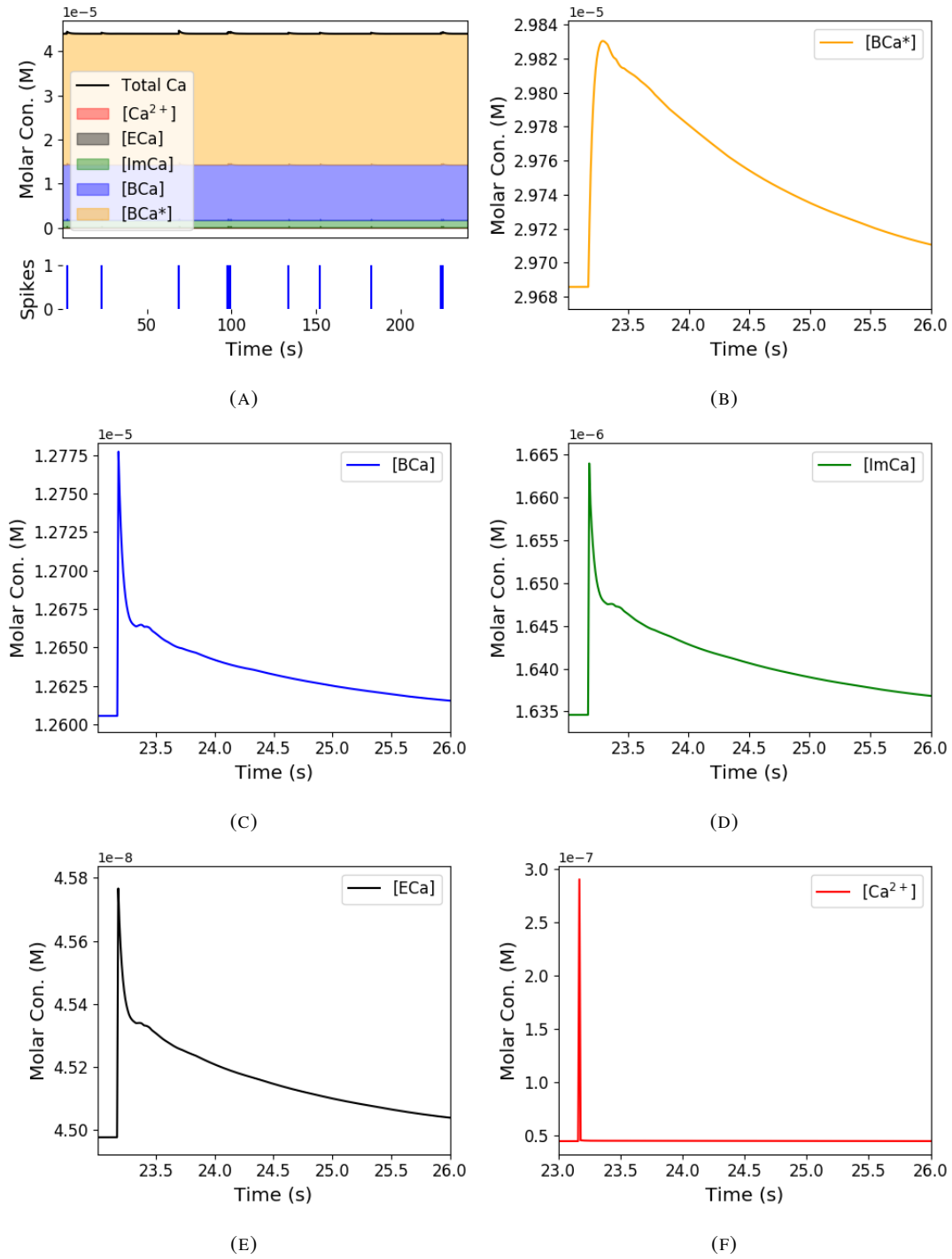


**FIGURE 2.3: Calcium Buffering Dynamics** (a) The proportions of bound and free calcium concentrations within a cell, with the associated spike train. (b)-(f) The dynamics of the concentration of (b) excited indicator bound calcium, (c) indicator bound calcium, (d) immobile endogenous buffer bound calcium, (e) mobile endogenous buffer bound calcium, and (f) free calcium in response to an action potential at  $\sim 23.2$ s.

969 a decay time constant of  $\sim 1$ s, while GCaMP6s has a decay time constant of  $\sim 2$ s (Chen  
970 et al., 2013). Here we asked how these differences in binding kinetics affect spike inference.  
971 We jointly varied the calcium binding and unbinding rates of the indicator by the same factor  
972 over a range from 100-fold slower to 100-fold faster from the fitted values, and simulated the  
973 fluorescence response for each of the parameter settings in response to the same spike trains  
974 as before (figure 2.4). Notably this manipulation does not affect the indicators affinity, and  
975 therefore would not affect steady-state responses to prolonged changes in calcium. Instead  
976 it is likely to affect its sensitivity to the spike train dynamics. We computed two summary  
977 measures from the simulated fluorescence traces: the signal-to-noise ratio for a single spike  
978 (Methods, section 2.2.6), and the accuracy of spike inference for each of the spike trains. We  
979 observed a reduction in the signal-to-noise ratio and the spike inference quality when we set  
980 the binding and unbinding rates were set to one hundredth of their fitted values, and to one  
981 tenth of their fitted values. When we increased the value of both binding rates, we observed  
982 no change in these measurements. The reduction in both rates lead to smaller increases in  
983 fluorescence in response to an action potential and a longer decay time (figure 2.4a), this  
984 caused the reduction in signal-to-noise ratio. As both rates were increased, the change in  
985  $\Delta F/F_0$  in response to an action potential increased and the decay time decreased slightly,  
986 but the fluorescence trace created by these values was very similar to the trace created by the  
987 fitted values.

988 Second, the overall concentrations of GCaMP often varies from cell to cell. For exam-  
989 ple different cells, even of the same type in the same tissue, can express different levels of  
990 GCaMP, due to proximity to the infection site, or the cell becoming ‘nuclear-filled’ (Tian et  
991 al., 2009; Chen et al., 2013). Also, GCaMP is often used for longitudinal experiments where  
992 the same cells are re-imaged across multiple days or weeks. However since GCaMP expres-  
993 sion typically ramps up over time (Chen et al., 2013), the accuracy of spike inference may  
994 differ across multiple longitudinal recordings in the same cell. We addressed this by varying  
995 the concentration of calcium indicator in the model, simulating spike trains and measuring  
996 signal-to-noise ratio and spike inference accuracy on the resulting fluorescence traces. Both  
997 increasing and decreasing the concentration of the indicator had effects on the fluorescence  
998 trace, signal-to-noise ratio, and spike inference. The signal-to-noise ratio and spike inference  
999 quality decreased with decreased indicator concentration, and both showed a decrease when  
1000 the indicator concentration was increased to 100 times its fitted value (figure 2.5). The signal-  
1001 to-noise ratio showed an increase when the indicator concentration was increased to 10 times  
1002 its fitted value, but there was no corresponding change in the spike inference quality. The

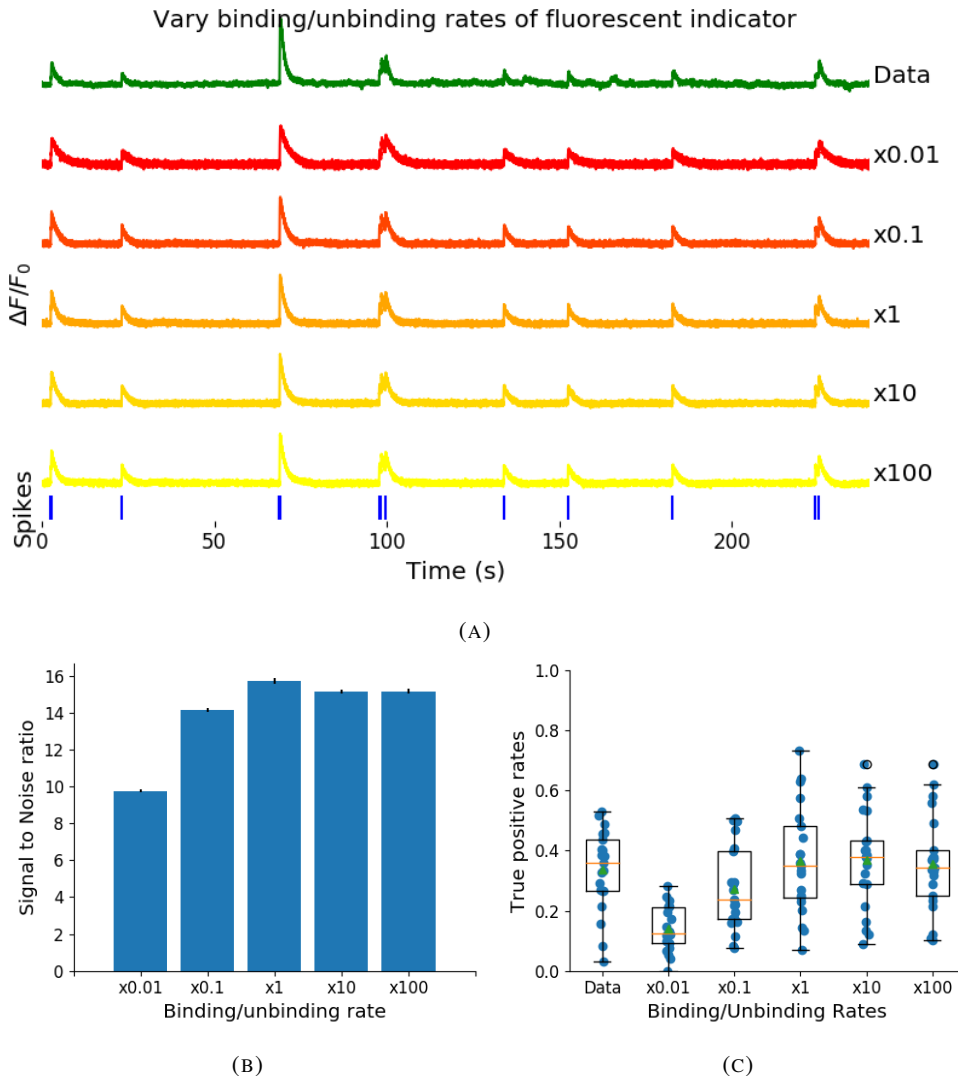


FIGURE 2.4: (a) An example trace for each of the five pairs of values used for the binding and unbinding rates of the fluorescent calcium indicator. (b) The signal-to-noise ratio of the modelled fluorescence traces using each of the four perturbed value pairs, and the experimental value. The SNRs for the value pairs perturbed downward are lower than that for the unperturbed value pair or the higher value pairs. (c) The true-positive rates of the deconvolution algorithm's predictions when inferring from the observed data, and inferring from modelled traces using the perturbed and experimental values.

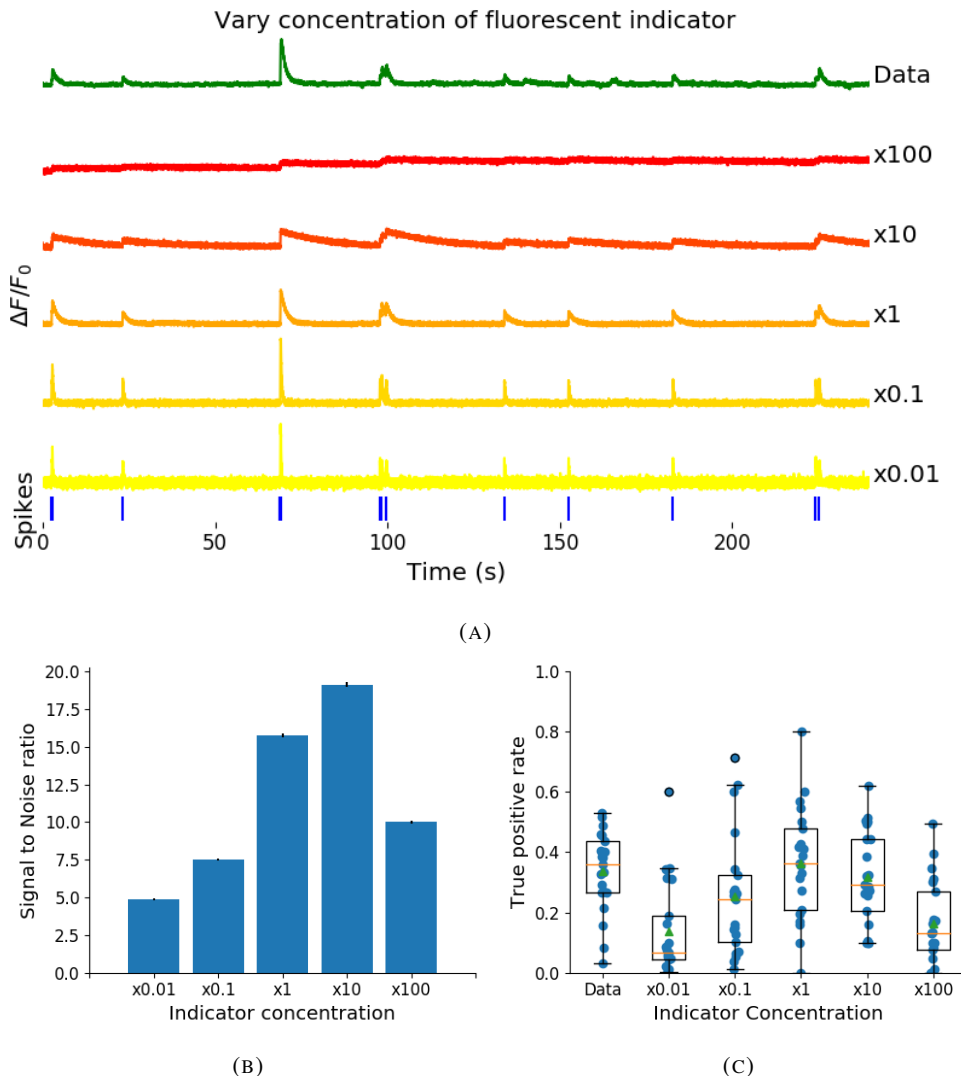


FIGURE 2.5: (a) An example trace for each of the five perturbed values for the concentration of fluorescent calcium indicator. The top two traces are produced by the lower perturbed values, the middle trace is produced by the experimental value, and the lowest two traces are produced when using the higher perturbed values. (b) The signal-to-noise ratio of the modelled fluorescence traces using each of the four perturbed values, and the experimental value. Extreme perturbations of the concentration either above or below the experimental level lowered the SNR. (c) The true-positive rates of the deconvolution algorithm’s predictions when inferring from the observed data, and inferring from modelled traces using the perturbed and experimental values. We found that the algorithms performs equally badly on the two most extreme values, and performs equally well on the experimental value, and the next higher perturbed value.

1003 decrease in indicator concentration caused a reduction in the increase in  $\Delta F / F_0$  in response  
1004 to an action potential, and an increase in the decay time of this increase (figure 2.5a). The  
1005 increase in indicator concentration had the opposite effect, it caused an increase in the change  
1006 in  $\Delta F / F_0$  in response to an action potential, and a decrease in the decay time.

1007 Third, the concentration and types of endogenous calcium buffers also vary from neuron  
1008 to neuron, both within and between cell types (Bartol et al., 2015; Maravall et al., 2000;  
1009 Neher and Augustine, 1992). Since the calcium buffer capacity of neurons is high, around  
1010 50-70 (Lee et al., 2000) in excitatory hippocampal pyramidal cells, around 100-250 (Lee et  
1011 al., 2000) in inhibitory hippocampal pyramidal cells, and 900-200 in Purkinje cells (depend-  
1012 ing on the age of the subject), these endogenous buffers compete with GCaMP for binding  
1013 to calcium, and variations in endogenous buffer concentration may affect GCaMP signal and  
1014 therefore spike inference. To address this we varied the concentration of the endogenous  
1015 buffer in the model neuron over five orders of magnitude from 0.8 to 8000  $\mu\text{M}$ , simulated  
1016 calcium fluorescence traces in response to the same set of spike trains, and performed spike  
1017 inference on the resulting fluorescence time series. Increasing the endogenous buffer con-  
1018 centration had a substantial effect on the GCaMP fluorescence signal, both decreasing its  
1019 amplitude and slowing its kinetics (figure 2.6(a)). This corresponded with a decrease in both  
1020 single-spike signal-to-noise ratio (figure 2.6(b)) and spike inference accuracy (figure 2.6(c)).  
1021 In contrast, decreasing endogenous buffer capacity from the fitted value had little effect on  
1022 either the GCaMP signal or spike inference (figure 2.6).

1023 **2.3.5 Single spike inference accuracy drops for high firing rates, but firing rate  
1024 itself can be estimated from mean fluorescence amplitude**

1025 The fluorescence signal recorded from neurons using calcium indicators is typically much  
1026 slower than changes in membrane potential for two reasons: first, because the calcium and  
1027 the indicator have slow binding and unbinding kinetics, the signal is a low-pass filtered ver-  
1028 sion of the membrane potential. Second, neuronal two-photon imaging experiments are often  
1029 performed in scanning mode, which limits their frame rate to  $\sim 10\text{Hz}$  or slower. This im-  
1030 plies that multiple spike events that occur close in time might be difficult to resolve from a  
1031 calcium indicator time series. Many cells, especially several types of inhibitory interneurons,  
1032 fire tonically at rates higher than 10Hz. We used the model to test whether spike inference  
1033 accuracy depended on the neuron's firing frequency by driving the cell with spike trains sam-  
1034 pled from a Poisson processes of varying frequency. We simulated a variable firing rate using  
1035 an Ornstein-Uhlenbeck process, and simulated the spike trains using a Poisson distribution

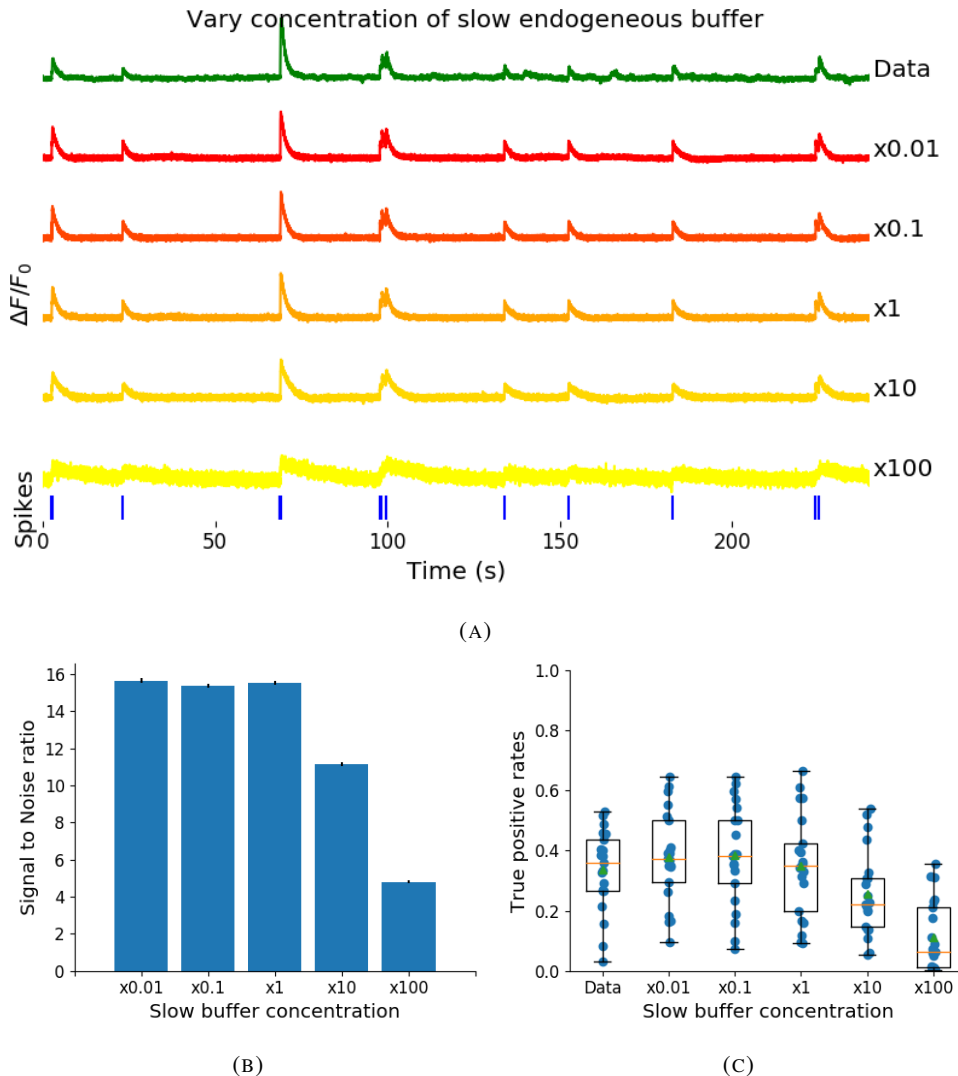
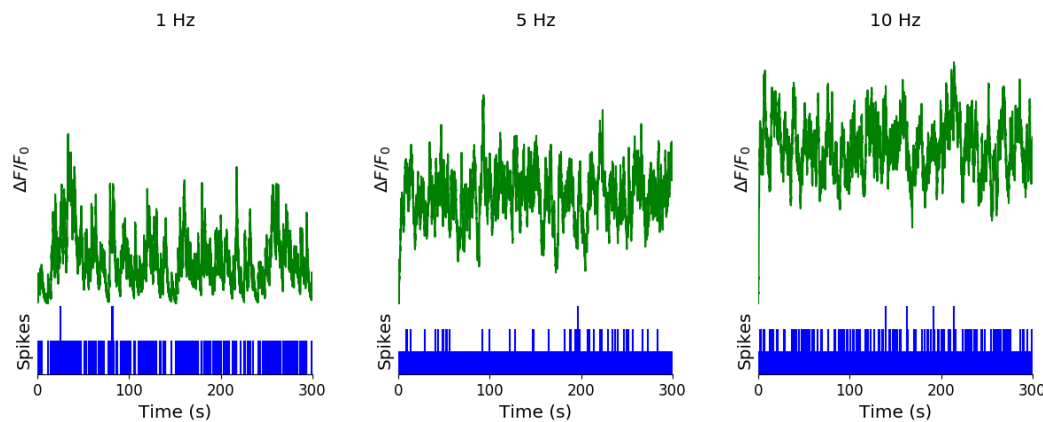


FIGURE 2.6: (a) An example trace for each of the five perturbed values for the concentration of immobile endogenous buffer. (b) The signal-to-noise ratio of the modelled fluorescence traces using each of the four perturbed values, and the experimental value. The lower values for the immobile buffer produce the same SNR as the experimental value. But the higher perturbed values produce fluorescence traces with a lower SNR. (c) The true-positive rates of the deconvolution algorithm’s predictions when inferring from the observed data, and inferring from modelled traces using the perturbed and experimental values.

with its rate taken from this process. Because of the high frequency firing rate of these spike trains, we used the accuracy as the measure of spike inference quality. We simulated 30 spike trains at average firing rate of 1, 5, and 10Hz, and measured the spike inference quality of all these traces. Spike inference accuracy decreased with increasing firing rate, for up to 10Hz Poisson spike trains (figure 2.8(left)). Although the accuracy remained above 90% for each of the three frequencies. We also plotted the average  $\Delta F/F_0$  as a function of stimulation firing rate. We found that it increased monotonically as a function of firing rate (figure 2.8(right)).

We expected lower spike inference quality as the average spiking frequency increased. Since the fluorescence trace, in some sense, is a low pass filtered version of the spike train, a tightly packed groups of spikes will be more difficult to infer than isolated spikes. However, the increasing amplitude of the fluorescence trace with increasing frequency suggests that some spike inference algorithm could be developed based on this amplitude.



**FIGURE 2.7: Simulating fluorescence traces at different firing rates** Example modelled traces created using simulated spike trains with a mean firing rate of 1Hz (left column), 5Hz (middle column), and 10Hz (right column). Note the difference in amplitude with different mean firing rates.

## 2.4 Discussion

We designed a biophysical model for the changes in free calcium and bound calcium concentrations within a cell soma with a fluorescent calcium indicator. We used this model to model the fluorescence trace resulting from a spike train in this cell. We fit the free parameters of the model by matching the power spectrum and amplitude of fluorescence traces with simultaneously measured spike trains. We inferred spikes from real fluorescence traces and modelled fluorescence traces, and measured the quality of the spike inference in both cases.

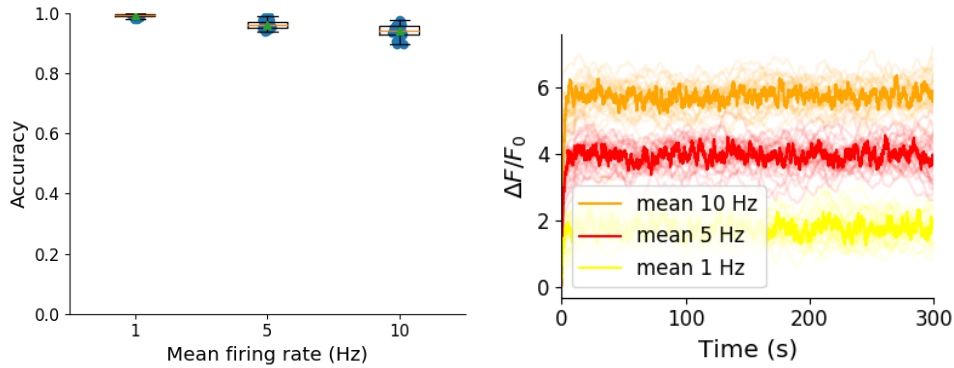


FIGURE 2.8: **Inference quality and  $\Delta F/F_0$  vs Firing rate** (left) The spike inference accuracy when applied to 30 traces created using simulated spike trains with mean firing rates of 1, 5, and 10 Hz. (right) The mean  $\Delta F/F_0$  across those 30 traces for each frequency.

1056 We found that the spike inference quality was similar in both cases. We perturbed the concentration of the calcium buffers in the model, and the binding/unbinding rates of those buffers  
 1057 in the model, and measured the effect on the signal-to-noise ratio (SNR) of the modelled  
 1058 fluorescence traces and the spike inference quality.  
 1059

1060 For the fluorescent calcium indicator, we found that any large perturbation away from  
 1061 the taken from the literature led to a reduction in SNR, and spike inference quality. For the  
 1062 binding/unbinding rates, we kept the ratio of these rates constant, but altered their values in  
 1063 parallel. The lower values caused a reduction in SNR, and a reduction in spike inference  
 1064 quality. For the endogenous buffer concentration, an increase above the experimental value  
 1065 caused a reduction in SNR and spike inference quality.

1066 Although the model produced visually similar time series to the real data, there were a  
 1067 few aspects it did not capture. First, the real data featured some low-frequency components  
 1068 that did not appear related to the spike events. These were not captured by the models we  
 1069 used in this study, but could be added in future by adding a suitable low-frequency term to the  
 1070 resulting time series. Second, the real data seemed to have some non-linearities not captured  
 1071 in the model, for example the response to two nearby spikes was greater than expected from  
 1072 the linear sum of two single spikes. This may be due to the co-operative binding of calmod-  
 1073 ulin to calcium, which gives calmodulin a supra-linear sensitivity to calcium concentration  
 1074 (Faas et al., 2011). The non-linear dynamics of this binding have been included in a recently  
 1075 developed spike inference model (Greenberg et al., 2018). Our model, in contrast, behaved  
 1076 much more linearly but could be extended in future to include such non-linearities. Third,  
 1077 in the real data the fluorescence peak amplitude seemed to vary from spike to spike, even  
 1078 for well-isolated spike events. Recent research has shown that calcium influx due to a single

1079 action potential was quite variable in pyramidal cells, and that this variability had a effect on  
1080 spike inference (Éltes et al., 2019). However in our model we assumed each spike lead to the  
1081 same fixed-amplitude injection of calcium to the cell, leading to much greater regularity in  
1082 fluorescence peak amplitudes. This variability could be added in future versions of the model  
1083 by making the injected calcium peak a random variable. Fourth, we modelled the soma as  
1084 a single compartment, but in reality there is likely a non-uniform spatial profile of calcium  
1085 concentration. This may matter because some endogenous buffers might access calcium right  
1086 as it influxes from the extracellular space, whereas the majority of the fluorescence signal is  
1087 more likely coming from the bulk of the cytoplasm. Future models could attempt to model  
1088 these spatial dependencies to assess whether they affect the overall spike inference procedure.

1089 As well as the optimised parameters, the model has 14 fixed parameters than can be  
1090 changed to simulate different types of calcium indicators. This model could be used to test  
1091 the theoretical performance of proposed new types of calcium indicator. The model could  
1092 also be used by developers of spike inference algorithms to test the effects of changing cal-  
1093 cium indicator parameters on spike inference, or to test the affects of changing spiking char-  
1094 acteristics on spike inference. For example, high firing rate vs low firing rate, or bursting vs  
1095 no bursting. Given the increasing amplitude of the fluorescence trace with increasing mean  
1096 firing rate, it would be possible to build a spike inference algorithm on this principle at least  
1097 in part.

1098 Our model has already been used as a tool by our colleagues, for simulating fluorescence  
1099 traces in response to cells that can fire with a continuous rate between 10 and 20Hz, but do  
1100 not always do so. Our colleagues found that a combination of the amplitude and the variance  
1101 of the simulated fluorescence trace was the best indicator of firing rate. For example, when  
1102 a cell was not firing, the amplitude and variance of the fluorescence trace was relatively low.  
1103 When the cell fired with a low firing rate  $\sim 1\text{Hz}$ , the mean amplitude was still low but  
1104 the variance of the fluorescence trace was high, and for high firing rate  $\sim 10 - 20\text{Hz}$ , the  
1105 fluorescence amplitude was high, and the variance was low. In this way, our model may be  
1106 useful for investigating firing rates underlying real fluorescence traces in response to cells  
1107 which can fire in these rage ranges.

1108 A recent paper by Greenberg et al (2018) described a biophysical model for spike train  
1109 inference called the ‘Sequential binding model’. Their model for spike inference was sim-  
1110 ilar to our model for fluorescence traces in that their model included parameters for two  
1111 types of endogenous buffer. But this model also included dynamics for calcium binding to  
1112 and unbinding from these endogenous buffers. Furthermore, this model included dynamics

1113 for calcium binding to and unbinding from the four binding sites present on a GCaMPs6  
1114 molecule. In the accuracy measurements specified in that paper, this model performed better  
1115 than the MLspike algorithm, which is also partially a biophysically model, and it performed  
1116 better than the constrained non-negative deconvolution algorithm. The sequential binding  
1117 model also has biophysically interpretable parameters, and its fitted parameters for quantities  
1118 such as buffering capacity and calcium influx upon action potential firing fall in line with  
1119 experimental values (Greenberg et al., 2018). Biophysical models like this appear to be the  
1120 way forward for spike inference algorithms, and would make a good complimentary tool to  
1121 our fluorescence model.

1122 **Chapter 3**

1123 **Functional networks expand across  
1124 anatomical boundaries as correlation  
1125 time-scale increases**

1126 *Abstract*

1127 Decades of research has established that correlated spiking plays a crucial role in represent-  
1128 ing sensory information. One drawback associated with the recent improvement in recording  
1129 technology and consequent large datasets is the difficulty in analysing higher order correla-  
1130 tions in large neuronal ensembles. One benefit of these datasets that has not yet been explored  
1131 is the opportunity to compare correlations within anatomical regions to correlations across  
1132 anatomical regions. In this work, we measured correlations between neurons residing in  
1133 nine different brains regions in three awake and behaving mice. Using the these correlation  
1134 measurements, we created weighted undirected graph networks and applied network science  
1135 methods to detect functional communities in our neural ensembles. We compared these func-  
1136 tional communities to their anatomical distribution. We repeated the analysis, using different  
1137 timescales for our correlation measurements, and found that functional communities were  
1138 more likely to be dominated by neurons from a single brain region at shorter timescales  
1139 (< 100ms).

### 1140 3.1 Introduction

1141 Decades of research has established that correlations play a crucial role in representing sen-  
1142 sory information. For example, the onset of visual attention has been shown to have a greater  
1143 affect on the correlations in the macaque V4 region than on the firing rates in that region  
1144 (Cohen and Maunsell, 2009). Recent findings show that spontaneous behaviours explain cor-  
1145 relations in parts of the brain not associated with motor control (Stringer et al., 2019), that  
1146 satiety state appears to have a brain wide representation (Allen et al., 2019), and that subject  
1147 exploratory and non-exploratory states are represented in the amygdala (Gründemann et al.,  
1148 2019). So, behavioural states are likely represented across many regions of the brain, not just  
1149 motor related areas. In order to understand the brain, we must understand the interactions  
1150 between neurons and regions.

1151 Because of limitations in recording technology almost all research has explored corre-  
1152 lations between neurons within a given brain region, or within only two regions at most  
1153 (Wierzynski et al., 2009; Patterson et al., 2014; Girard, Hupé, and Bullier, 2001). Rela-  
1154 tively little is known about correlations between neurons in many different brain regions.  
1155 However, the recent development of ‘Neuropixels’ probes (Jun et al., 2017) has allowed  
1156 extracellular voltage measurements to be collected from multiple brain regions simultane-  
1157 ously routinely, and in much larger numbers than traditional methods. In this project we  
1158 used a publicly-available Neuropixels dataset to analyse correlations between different brain  
1159 regions (Stringer et al., 2019).

1160 A drawback associated with the improvement in recording technology is an increase in  
1161 the difficulty in analysing these data. For example, analysing the  $i$ th order interactions of  
1162  $N$  neurons generally requires estimation of  $N^i$  parameters. A number that becomes astro-  
1163 nomical for large  $N$ . New methods are required for analysing these new large datasets. We  
1164 attempted to address this requirement in this piece of research by applying a cutting-edge  
1165 network science community detection method to neural data.

1166 Another unexplored area of research is the changes in cell interactions at different timescales.  
1167 Studies have shown different timescales for fluctuations in spiking activity (Murray et al.,  
1168 2014), and different time scales for event representation (Baldassano et al., 2017) across dif-  
1169 ferent brain regions. Still most studies focus on quantifying interactions at a given timescale.  
1170 But neurons may interact differently, or may interact with different neurons at different  
1171 timescales. Here we explore correlated communities of neurons at different timescales.

1172 In this work, we measured correlations between binned spike counts from neurons from

1173 nine different regions of the mouse brain. These measurements induced a weighted undi-  
1174 rected graph or network where each neuron is represented by a node, and the strength of  
1175 the connection between these nodes/neurons is the strength of the correlation between their  
1176 spike counts. We then applied newly invented network methods (Humphries et al., 2019)  
1177 to this network to find any community structure, and place the neurons in these correlation  
1178 based communities. Finally, we compared these functional communities to the anatomical  
1179 membership of the neurons.

1180 To investigate the functional communities and their relationship with anatomy at different  
1181 time scales, we repeated these analyses using different length bin widths when binning spike  
1182 times.

1183 To find and analyse functional networks while controlling for the subject’s behaviour, we  
1184 conditioned the binned spike counts on data from a video of the subject’s face, and repeated  
1185 our analysis for spike count correlations (or noise correlations) and signal correlations.

## 1186 3.2 Data

1187 The data that we used in this project were collected by Nick Steinmetz and his lab members  
1188 (Stringer et al., 2019).

### 1189 3.2.1 Brain regions

1190 Neuropixels probes were used to collect extracellular recordings (Jun et al., 2017) from three  
1191 different mice. The mice were awake, headfixed, and engaging in spontaneous behaviour.  
1192 The mice were of different sexes and different ages. One mouse was ‘wild-type’, the others  
1193 were mutants. Details as follows:

- 1194 1. male, wild type, P73.
- 1195 2. female, TetO-GCaMP6s, Camk2a-tTa, P113
- 1196 3. male, Ai32, Pvalb-Cre, P99

1197 Eight probes were used to collect readings from 2296, 2668, and 1462 cells respectively.  
1198 Data were collected from nine brain regions in each mouse:

- 1199 • Caudate Putamen (CP)
- 1200 • Frontal Motor Cortex (Frmocxt)
- 1201 • Hippocampal formation (Hpf)

- 1202     ● Lateral Septum (Ls)
- 1203     ● Midbrain (Mb)
- 1204     ● Superior Colliculus (Sc)
- 1205     ● Somatomotor cortex (Sommotcx)
- 1206     ● Thalamus (Th)
- 1207     ● Primary visual cortex (V1)

1208   Readings were continuous and lasted for about 1 hour (Stringer et al., 2019). Locations of  
 1209   each of the probes can be seen in figure 3.1.

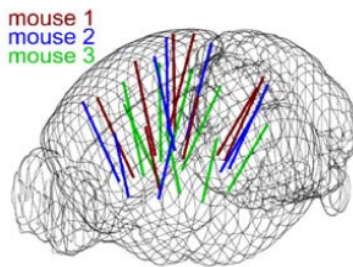


**FIGURE 3.1: Probe Locations:** The locations of the probes in each of the three mouse brains (Stringer et al., 2019).

### 1210   **3.2.2 Video recordings**

1211   Video recordings of the mouse's face were taken during the spontaneous behaviour. We had  
 1212   access to the top 500 principle components and top 500 eigenvectors of the processed videos.  
 1213   The frequency of recording was slightly less than 40Hz. Each frame contained  $327 \times 561$   
 1214   pixels. These principal components were used as behavioural data. We controlled for these  
 1215   components when taking measurements conditioned on behaviour.

## 1216   **3.3 Methods**

### 1217   **3.3.1 Binning data**

1218   We transformed the spike timing data into binned spike count data by dividing the experi-  
 1219   mental period into time bins and counting the spikes fired by each cell within the time period  
 1220   covered by each of those bins. The data were divided into time bins of various widths ranging  
 1221   from 0.01s to 4s.

1222 If the total length of the recording period was not an integer multiple of the time bin  
 1223 width, we cut off the remaining time at the end of the recording period. This period was at  
 1224 most 3.99s. This is far less than the total recording time of around 1 hour. So, this detail  
 1225 would not affect our results.

1226 **3.3.2 Correlation coefficients**

We calculated Pearson's correlation coefficient for pairs of spike counts from pairs of neurons. For jointly distributed random variables  $X$  and  $Y$ , Pearson's correlation coefficient is defined as:

$$\rho_{XY} = \frac{\text{cov}(X, Y)}{\sigma_X \sigma_Y} \quad (3.1)$$

$$= \frac{E[(X - \mu_X)(Y - \mu_Y)]}{\sigma_X \sigma_Y} \quad (3.2)$$

1227 where  $E$  denotes the expected value,  $\mu$  denotes the mean, and  $\sigma$  denotes the standard deviation.  
 1228 The correlation coefficient is a normalised measure of the covariance. It can take values  
 1229 between 1 (completely correlated) and  $-1$  (completely anti-correlated). Two independent  
 1230 variables will have a correlation coefficient of 0. But, having 0 correlation does not imply  
 1231 independence.

If we do not know the means and standard deviations required for equation 3.1, but we have samples from  $X$  and  $Y$ , Pearson's sample correlation coefficient is defined as:

$$r_{XY} = \frac{\sum_{i=1}^n (x_i - \bar{x})(y_i - \bar{y})}{\sqrt{\sum_{i=1}^n (x_i - \bar{x})^2} \sqrt{\sum_{i=1}^n (y_i - \bar{y})^2}} \quad (3.3)$$

1232 where  $\{(x_i, y_i)\}$  for  $i \in \{1, \dots, n\}$  are the paired samples from  $X$  and  $Y$ , and  $\bar{x} = \frac{1}{n} \sum_{i=1}^n x_i$ ,  
 1233 and  $\bar{y} = \frac{1}{n} \sum_{i=1}^n y_i$  are the sample means.

1234 In practice we used the python function `scipy.stats.pearsonr` to calculate the  
 1235 correlation coefficients.

1236 **Total correlations,  $r_{SC}$**

1237 The total correlation ( $r_{SC}$ ) of two cells is the correlation between the spike counts of those  
 1238 cells in response to a given stimulus condition.

1239 **Shuffled total correlations**

1240 We measured the shuffled total correlations between two neurons by randomly permuting one  
 1241 of the neuron's spike counts and measuring the total correlations. These shuffled correlations  
 1242 were useful when measuring the effect of time bin width on correlations, and when decid-  
 1243 ing which correlations should be preserved when creating correlation networks (see section  
 1244 3.3.5).

1245 **Separating Correlations & Anti-correlations**

1246 In order to compare the effect of bin width on measures of negative  $r_{SC}$  (anti-correlation) and  
 1247 positive  $r_{SC}$  separately, we had to separate correlated and anti-correlated pairs. To do this, we  
 1248 simply measured the mean  $r_{SC}$ , taking the mean across all the bin widths. If this quantity was  
 1249 positive or zero we regarded the pair as positively correlated. If this quantity was negative  
 1250 we regarded the pair as anti-correlated.

1251 **3.3.3 Conditioning on behavioural data**

Our behavioural data consisted of the top 500 principal components (PCs) of a processed video recording of the mouse's face (see section 3.2.2). Denoting the spike count of a given cell by  $X$ , and the PCs by  $Z_1, \dots, Z_{500}$ , we wanted to model  $X$  as a function of  $Z_1, \dots, Z_{500}$  in order to estimate

$$E[X|Z_1, \dots, Z_{500}] = \int_{x \in X} x P(X = x|Z_1, \dots, Z_{500}) dx \quad (3.4)$$

$$= \int_{x \in X} x \frac{P(X = x, Z_1, \dots, Z_{500})}{P(Z_1, \dots, Z_{500})} dx \quad (3.5)$$

1252 Given the 500 components, a naïve estimation of  $P(Z_1, \dots, Z_{500})$  or  $P(X, Z_1, \dots, Z_{500})$  by  
 1253 histogramming was impossible. Therefore we modelled  $X$  as a linear combination of the  
 1254 PCs.

1255 **Linear regression**

1256 We modelled the spike count of a given cell,  $X$ , as a linear combination of the PCs of the  
 1257 video of the mouse's face,  $\mathbf{Z} = Z_1, \dots, Z_{500}$ . We tried three different types of regularization

1258 • L1 or 'Lasso'

1259 • L2 or 'Ridge regression'

- 1260 • ‘Elastic net’ regularisation (a linear combination of both  $L1$  and  $L2$  regularisation  
 1261 penalties)

1262 The elastic net regularisation performed the best, so we stuck with that.

1263 **Elastic net regularisation**

Suppose we wish to model  $n$  observations of a random variable  $X$ ,  $\mathbf{x} = (x_1, \dots, x_n)$  using  $n$  instances of  $m$  predictors  $\mathbf{Z} = (Z_1, \dots, Z_m)$ . The naïve elastic net criterion is

$$L(\lambda_1, \lambda_2, \boldsymbol{\beta}) = |\mathbf{x} - \mathbf{Z}\boldsymbol{\beta}|^2 + \lambda_2|\boldsymbol{\beta}|_2 + \lambda_1|\boldsymbol{\beta}|_1 \quad (3.6)$$

where

$$|\boldsymbol{\beta}|_2 = \sum_{j=1}^m \beta_j^2 \quad (3.7)$$

$$|\boldsymbol{\beta}|_1 = \sum_{j=1}^m |\beta_j| \quad (3.8)$$

The naïve elastic net estimator  $\hat{\boldsymbol{\beta}}$  is the minimiser of the system of equations 3.6 (Zou and Hastie, 2005)

$$\hat{\boldsymbol{\beta}} = \arg \min_{\boldsymbol{\beta}} L(\lambda_1, \lambda_2, \boldsymbol{\beta}) \quad (3.9)$$

1264 We implemented the model using the `ElasticNetCV` method of Python’s  
 1265 `sklearn.linear_models` package.

1266 As well as using the PCs, we also tried fitting the models using the raw video data recon-  
 1267 structed from the PCs and eigenvectors. These models performed worse than those using the  
 1268 PCs. We expected this because each representation contains the same amount of information,  
 1269 but the raw video representation spreads this information across many more components.  
 1270 This requires more parameter fitting, but given the same information.

1271 **Conditional covariance**

We calculated the expected value of the conditional covariance using the law of total covariance.

$$\text{cov}(X, Y) = E[\text{cov}(X, Y|Z)] + \text{cov}(E[X|Z], E[Y|Z]) \quad (3.10)$$

1272 where these expected values are calculated with respect to the distribution of  $Z$  as a random  
 1273 variable.

1274 The law of total covariance breaks the covariance into two components. The first com-  
 1275 ponent  $E[\text{cov}(X, Y|Z)]$  is the expected value, under the distribution of  $Z$ , of the conditional  
 1276 covariance  $\text{cov}(X, Y|Z)$ . This covariance could be interpreted as the unnormalised version  
 1277 of what Cohen et al. (2011) call the spike count correlation (Cohen and Kohn, 2011), aka.  
 1278 the noise correlation. In particular, this is the covariance of the spike counts in response to  
 1279 repeated presentation of identical stimuli.

1280 The second component is analogous to what Cohn et al. (2011) call the *signal correlation*  
 1281 (Cohen and Kohn, 2011). In particular,  $\text{cov}(E[X|Z], E[Y|Z])$  is the covariance between  
 1282 spike counts in response to different stimuli.

Using our linear model, we calculated  $E[X|Z_1, \dots, Z_{500}]$  for each cell  $X$ . Then we pro-  
 ceeded to calculate

$$E[\text{cov}(X, Y|Z_1, \dots, Z_{500})] = \text{cov}(X, Y) - \quad (3.11)$$

$$\text{cov}(E[X|Z_1, \dots, Z_{500}], E[Y|Z_1, \dots, Z_{500}]) \quad (3.12)$$

1283 **Measures of conditional correlation**

As a measure of expected correlation, we measured the ‘event conditional correlation’ (Maugis,  
 2014)

$$\rho_{XY|Z} = \frac{E[\text{cov}(X, Y|Z)]}{\sqrt{E[\text{var}(X|Z)]E[\text{var}(Y|Z)]}} \quad (3.13)$$

1284 Although this is not an actual correlation, it is an intuitive analogue to the correlation as a  
 1285 normalised version of the covariance.

For comparison, we also measured the ‘signal correlation’

$$\rho_{\text{signal}} = \frac{\text{cov}(E[X|Z], E[Y|Z])}{\sqrt{\text{var}(E[X|Z])\text{var}(E[Y|Z])}} \quad (3.14)$$

1286 this is an actual correlation.

1287 **3.3.4 Information Theory**

1288 **Entropy  $H(X)$**

The entropy of a random variable  $X$ , with outcomes  $x_1, \dots, x_N$ , and corresponding probabilities  $p_1, \dots, p_N$  is defined as

$$H(X) = - \sum_{n=1}^N p_n \log_2 p_n \quad (3.15)$$

1289 This quantity is also known as the information entropy or the ‘surprise’. It measures the  
 1290 amount of uncertainty in a random variable. For example, a variable with a probability of 1  
 1291 for one outcome, and 0 for all other outcomes will have 0 bits entropy, because it contains no  
 1292 uncertainty. But a variable with a uniform distribution will have maximal entropy as it is the  
 1293 least predictable. This quantity is analogous to the entropy of a physical system (Shannon,  
 1294 1948). Note that any base may be used for the logarithm in equation 3.15, but using base 2  
 1295 means that the quantity will be measured in ‘bits’.

The joint entropy of two jointly distributed random variables  $X$  and  $Y$ , where  $Y$  has outcomes  $y_1, \dots, y_M$ , is defined as

$$H(X, Y) = - \sum_{n=1}^N \sum_{m=1}^M P(X = x_n, Y = y_m) \log_2 P(X = x_n, Y = y_m) \quad (3.16)$$

1296 If  $X$  and  $Y$  are independent then  $H(X, Y) = H(X) + H(Y)$ . Otherwise  $H(X, Y) <$   
 1297  $H(X) + H(Y)$ . When  $X$  and  $Y$  are completely dependent  $H(X, Y) = H(X) = H(Y)$ .

The conditional entropy of  $Y$  conditioned on  $X$  is defined as

$$H(Y|X) = - \sum_{n=1}^N \sum_{m=1}^M P(X = x_n, Y = y_m) \log_2 \frac{P(X = x_n, Y = y_m)}{P(X = x_n)} \quad (3.17)$$

1298 When  $X$  and  $Y$  are independent  $H(Y|X) = H(Y)$ . Intuitively, we learn nothing of  $Y$  by  
 1299 knowing  $X$ , so  $Y$  is equally uncertain whether we know  $X$  or not. If  $Y$  is totally dependent  
 1300 on  $X$ , then the fraction in the logarithm is 1, which gives  $H(Y|X) = 0$ .

1301 These entropy measures are the basis of the mutual information measure.

1302 **Maximum entropy limit**

When spiking data is binned into spike counts there is an upper limit on the entropy of these data. The maximum entropy discrete distribution is the discrete uniform distribution. A

random variable with this distribution will take values from some finite set with equal probabilities. Binned spike count data will take values between 0 and some maximum observed spike count  $n_{\max}$ . A neuron with responses that maximises entropy will take these values with equal probability, i.e. if  $i \in \{0, \dots, n_{\max}\}$  then  $P(X = i) = \frac{1}{n_{\max} + 1}$ . The entropy of this neuron will be

$$\begin{aligned} H(X) &= - \sum_{i=0}^{n_{\max}} P(X = i) \log_2 P(X = i) \\ &= - \sum_{i=0}^{n_{\max}} \frac{1}{n_{\max} + 1} \log_2 \left( \frac{1}{n_{\max} + 1} \right) \\ &= - \log_2 \left( \frac{1}{n_{\max} + 1} \right) \\ &= \log_2 (n_{\max} + 1) \end{aligned}$$

1303 Therefore, the maximum entropy of the binned spike counts of a neuron is  $\log_2 (n_{\max} + 1)$ .  
 1304 Of course, it would be very unusual for a neuron to fire in accordance with the discrete  
 1305 uniform distribution. Most measurements of entropy taken on binned spiking data will be  
 1306 much lower than the maximum. See figure 3.2 to see the maximum entropy as a function of  
 1307 the maximum observed spike count.

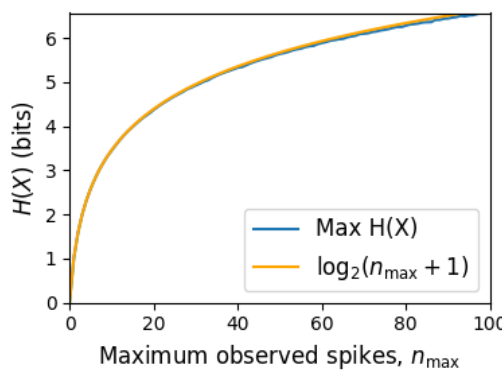


FIGURE 3.2: **Entropy Limit:** The upper limit on entropy of binned spike count data as a function of the maximum observed spike count. The orange line is the analytical maximum. The blue line is the entropy of samples with  $N = 1000$  data points taken from the discrete uniform distribution.

1308 **Mutual Information  $I(X; Y)$**

1309 The mutual information can be defined mathematically in a number of ways, all of which are  
 1310 equivalent. These definitions illustrate the different ways of interpreting the mutual informa-  
 1311 tion.

For two jointly distributed random variables  $X$  and  $Y$ , the mutual information  $I(X;Y)$  is defined as

$$I(X;Y) = H(Y) - H(Y|X) \quad (3.18)$$

$$= H(X) - H(X|Y) \quad (3.19)$$

1312 Equation 3.18 fits with the following intuition: The mutual information between  $X$  and  $Y$  is  
1313 the reduction in uncertainty about  $X$  gained by knowing  $Y$ , or vice versa. We could also say  
1314 the mutual information is the amount of information gained about  $X$  by knowing  $Y$ , or vice  
1315 versa.

Another useful entropy based definition for the mutual information is

$$I(X;Y) = H(X) + H(Y) - H(X,Y) \quad (3.20)$$

1316 This definition is useful because it does not require the calculation of conditional probabili-  
1317 ties.

The mutual information can also be defined in terms of marginal, joint, and conditional distributions. For example,

$$I(X;Y) = - \sum_{n=1}^N \sum_{m=1}^M P(X = x_n, Y = y_m) \log_2 \frac{P(X = x_n, Y = y_m)}{P(X = x_n)P(Y = y_m)} \quad (3.21)$$

Notice that this can be rewritten as a Kullback–Leibler divergence.

$$I(X;Y) = D_{KL}(P(X,Y) || P(X)P(Y)) \quad (3.22)$$

1318 So, we can also think of the mutual information as a measure of the difference between  
1319 the joint distribution of  $X$  and  $Y$ , and the product of their marginal distributions. Since the  
1320 product of the marginal distributions is the joint distribution for independent variables, we  
1321 can think of the mutual information as a measure of the variables’ dependence on one another.

1322 The minimum value that  $I(X;Y)$  can take is 0. This occurs when the random variables  
1323  $X$  and  $Y$  are independent. Then we have  $H(X|Y) = H(X)$ , and  $H(Y|X) = H(Y)$ , which  
1324 according to equation 3.18, gives  $I(X;Y) = 0$ . We also have that  $H(X,Y) = H(X) +$   
1325  $H(Y)$  in this case, which according equation 3.20, gives  $I(X;Y) = 0$ . Finally, we also have  
1326  $P(X,Y) = P(X)P(Y)$ , which leaves us with 1 in the argument for the logarithm in equation  
1327 3.21, which again gives  $I(X;Y) = 0$ .

1328     The mutual information reaches its maximum value when one of the variables  $X$  and  
 1329      $Y$  is completely determined by knowing the value of the other. In that case  $I(X; Y) =$   
 1330      $\min\{H(X), H(Y)\}$ .

1331     **Variation of Information**  $VI(X, Y)$

The variation of information is another information theoretical quantity based on the mutual information. It is defined as

$$VI(X; Y) = H(X) + H(Y) - 2I(X; Y) \quad (3.23)$$

We can rewrite this as the summation of two positive quantities

$$VI(X; Y) = [H(X) - I(X; Y)] + [H(Y) - I(X; Y)] \quad (3.24)$$

1332     In English, the variation of information is the summation of the uncertainty in the random  
 1333     variables  $X$  and  $Y$  excluding the uncertainty shared by those variables.

1334     This measure will become more relevant when we go on to talk about clusterings because  
 1335      $VI(X; Y)$  forms a metric on the space of clusterings.

1336     **Measuring entropies & mutual information**

1337     In practice, we measured the mutual information between spike counts using Python and the  
 1338     python package `pyitlib`. We used the PT-bias correction technique to estimate the bias of  
 1339     our measurements when measuring the mutual information between the spike counts of two  
 1340     cells (Treves and Panzeri, 1995).

1341     When measuring the mutual information between clusterings we used Python, but we  
 1342     used the `mutual_info_score`, `adjusted_mutual_info_score`, and  
 1343     `normalized_mutual_info_score` functions from the `sklearn.metrics` part of  
 1344     the `sklearn` package.

1345     **3.3.5 Network analysis**

1346     **Correlation networks**

1347     In order to analyse functional networks created by the neurons in our ensemble, we mea-  
 1348     sured the total correlation between each pair of neurons. These measurements induced an

1349 undirected weighted graph/network between the neurons. The weight of each connection  
1350 was equal to the total correlation between each pair of neurons.

1351 We followed the same procedure for total correlations 3.3.2, spike count correlations, and  
1352 signal correlations 3.3.3.

1353 **Rectified correlations**

1354 At the time of writing, the community detection method outlined in (Humphries et al., 2019)  
1355 could only be applied to networks with positively weighted connections. But many neuron  
1356 pairs were negatively correlated. To apply the community detection method, we *rectified* the  
1357 network, by setting all the negative weights to zero.

1358 We also looked for structure in the network created by negative correlations by reversing  
1359 the signs of the correlations, and rectifying these correlations before applying our network  
1360 analysis.

1361 Finally, we used the absolute value of the correlations as the weights for the graph/network.  
1362 By doing this, we hoped to identify both correlated and anti-correlated functional communi-  
1363 ties of neurons.

1364 **Sparsifying data networks**

1365 When creating our correlation networks, we wanted to exclude any correlations that could  
1366 be judged to exist ‘by chance’. To do this, we measured the 5th and 95th percentile of  
1367 the shuffled correlations (see section 3.3.2) for the given mouse and time bin width. We  
1368 then set all the data correlations between these two values to 0. This excluded any ‘chance’  
1369 correlations from our network, and created a sparser network. This allowed us to make use  
1370 of the ‘sparse weighted configuration model’ as described in section 3.3.5.

1371 **Communities**

1372 Given some network represented by an adjacency matrix  $\mathbf{A}$ , a community within that net-  
1373 work is defined as a collection of nodes where the number of connections within these nodes  
1374 is higher than the expected number of connections between these nodes. In order to quan-  
1375 tify the ‘expected’ number of connections, we need a model of expected networks. This is  
1376 analogous to a ‘null model’ in traditional hypothesis testing. We test the hypothesis that our  
1377 data network departs from the null network model to a statistically significant degree. For  
1378 undirected unweighted networks, the canonical model of a null network is the configuration

model (Fosdick et al., 2016). Since we are working with weighted sparse networks, we used more suitable null models, described below.

### 1381 **Weighted configuration model**

1382 The *weighted configuration model* is a canonical null network model for weighted networks.  
 1383 Given some data network, the weighted configuration model null network will preserve the  
 1384 degree sequence and weight sequence of each node in the data network. But the edges will  
 1385 be distributed randomly (Fosdick et al., 2016). Any structure in the data network beyond  
 1386 its degree sequence and weight sequence will not be captured in the weighted configuration  
 1387 model. So, this model can be used in testing the hypothesis that this extra structure exists.

### 1388 **Sparse weighted configuration model**

1389 The *sparse weighted configuration model* is another null network model. Similar in nature to  
 1390 the weighted configuration model (see section 3.3.5), but the sparsity of the data network is  
 1391 preserved in the null network. This is achieved by sampling from a probability distribution  
 1392 for the creation or non-creation of each possible connection, then distributing the weight of  
 1393 the data network randomly in this sparse network (Humphries et al., 2019). This is the null  
 1394 network that we used when searching for additional structure in our data networks.

### 1395 **Spectral rejection**

1396 We made use of the spectral rejection algorithm as outlined in (Humphries et al., 2019). The  
 1397 spectral rejection algorithm is a method for finding structure in a network not captured by a  
 1398 supposed null model, if such structure exists.

To describe the method, we denote our data network matrix  $\mathbf{W}$ , we denote the expected network of our null network model as  $\langle \mathbf{P} \rangle$ . Then the departure of our data network from the null network can be described by the matrix

$$\mathbf{B} = \mathbf{W} - \langle \mathbf{P} \rangle \quad (3.25)$$

1399 a common choice for  $\langle \mathbf{P} \rangle$  in community detection is the ‘configuration model’ (Fosdick et  
 1400 al., 2016; Humphries, 2011). The matrix  $\mathbf{B}$  is often called the configuration matrix, in this  
 1401 context we will use the term ‘deviation matrix’ as it captures the deviation of  $\mathbf{W}$  from the  
 1402 null model.

1403 To test for structure in the network represented by  $\mathbf{W}$ , we examine the eigenspectrum of  $\mathbf{B}$   
 1404 and compare it to the eigenspectrum of our null model. Firstly, note that since our data model  
 1405 doesn't allow self loops, and is not directed, the matrix representing the network will be  
 1406 symmetric and positive semi-definite, and will therefore be invertible with real eigenvalues.  
 1407 We selected a null model with the same characteristics.

1408 To find the eigenspectrum of the null model, we generated  $N$  samples from our null  
 1409 model  $P_1, \dots, P_N$ , and we measured their deviation matrices  $B_1, \dots, B_N$ . We then calculated  
 1410 the eigenspectrum of each of those samples. We calculated the upper bound of the null model  
 1411 eigenspectrum by taking the mean of the largest eigenvalues of  $B_1, \dots, B_N$ . We calculated a  
 1412 lower bound on the null model eigenspectrum by taking the mean of the smallest eigenvalues  
 1413 of  $B_1, \dots, B_N$ .

1414 We then calculated the eigenspectrum of  $\mathbf{B}$ , our data network deviation matrix. If any of  
 1415 those eigenvalues lay outside of the upper or lower bounds of the null model eigenspectrum,  
 1416 this is evidence of additional structure not captured by the null model. If we chose the sparse  
 1417 weighted configuration model (see section 3.3.5) as our null network model, then eigenvalues  
 1418 lying below the lower bound indicate  $k$ -partite structure in the network. For example, if one  
 1419 eigenvalue lay below the lower bound, this would indicate some bipartite structure in the data  
 1420 network. If any eigenvalues lay above the upper bound of the null model eigenspectrum, this  
 1421 is evidence of community structure in the data network. For example, one eigenvalue of  $\mathbf{B}$   
 1422 lying above the upper bound of the null model eigenspectrum indicates the presence of two  
 1423 communities in the network (Humphries, 2011).

#### 1424 Node rejection

1425 If there are  $d$  data eigenvalues lying outside of the null network eigenspectrum, the  $d$  eigen-  
 1426 vectors corresponding to these eigenvalues will form a vector space. If we project the nodes  
 1427 of our network into this vector space, by projecting either rows or columns of the data ma-  
 1428 trix, we can see how strongly each node contributes to the vector space. Nodes that contribute  
 1429 strongly to the additional structure will project far away from the origin, nodes that do not  
 1430 contribute to the additional structure will project close to the origin. We want to use this  
 1431 information to discard those nodes that do not contribute.

1432 We can test whether a node projects *far* away from the origin or *close* to the origin  
 1433 using the eigenvalues and eigenvectors of  $B_1, \dots, B_N$ . The  $j$ th eigenvector and eigenvalue  
 1434 of  $B_i$  gives a value for a null network's projection into the  $j$ th dimension of the additional  
 1435 structure vector space. The matrices  $B_1, \dots, B_N$  give  $N$  projections into that dimension.

1436 These projections are a distribution of the null networks' projections. If the data node's  
 1437 projection exceeds that of the null network projections this node is judged to project *far* from  
 1438 the origin, and therefore contribute to the additional structure. Otherwise, the node is judged  
 1439 to project *close* to the origin, and is therefore rejected (Humphries et al., 2019).

#### 1440 Community detection

1441 Another application for this  $d$  dimensional space is community detection. We first project  
 1442 all of the nodes into this  $d$ -dimensional space, then perform the clustering in this space. The  
 1443 clustering and community detection procedure is described in (Humphries, 2011).

1444 In practice, the procedure is carried out  $n$  times (we chose  $n = 100$  times), this returns  $n$   
 1445 clusterings. We resolve these  $n$  clusterings to one final clustering using *consensus clustering*.  
 1446 We used the consensus clustering method that uses an explicit null model for the consensus  
 1447 matrix, as outlined in (Humphries et al., 2019).

#### 1448 3.3.6 Clustering Comparison

A clustering  $\mathcal{C}$  is a partition of a set  $D$  into sets  $C_1, C_2, \dots, C_K$ , called clusters, that satisfy the following for all  $k, l \in \{1, \dots, K\}$ :

$$C_k \cap C_l = \emptyset \quad (3.26)$$

$$\bigcup_{k=1}^K C_k = D \quad (3.27)$$

1449 If we consider two clusterings,  $\mathcal{C}$  with clusters  $C_1, C_2, \dots, C_K$  and  $\mathcal{C}'$  with clusters  
 1450  $C'_1, C'_2, \dots, C'_K$ . There are a number of measurements we can use to compare  $\mathcal{C}$  and  $\mathcal{C}'$ . In  
 1451 the following, the number of elements in  $D$  is denoted by  $n$ , and the number of elements in  
 1452 cluster  $C_k$  is  $n_k$ .

#### 1453 Adjusted Rand Index

1454 The *adjusted Rand Index* is a normalised similarity measure for clusterings based on pair  
 1455 counting.

1456 If we consider the clusterings  $\mathcal{C}$  and  $\mathcal{C}'$ , and denote

1457 • the number of pairs in the same cluster in  $\mathcal{C}$  and  $\mathcal{C}'$  by  $N_{11}$

1458 • the number of pairs in different clusters in  $\mathcal{C}$  and  $\mathcal{C}'$  by  $N_{00}$

- 1459 • the number of pairs in the same cluster in  $\mathcal{C}$  and different clusters in  $\mathcal{C}'$  by  $N_{10}$

- 1460 • the number of pairs in different clusters in  $\mathcal{C}$  and the same cluster in  $\mathcal{C}'$  by  $N_{01}$

then the *Rand Index* is defined as

$$RI = \frac{N_{11} + N_{00}}{N_{11} + N_{00} + N_{10} + N_{01}} = \frac{N_{11} + N_{00}}{\binom{n}{2}} \quad (3.28)$$

1461 The Rand Index is 1 when the clusterings are identical, and 0 when the clusterings are com-  
1462 pletely different.

The *adjusted Rand Index* intends on correcting the Rand Index for chance matching pairs.

This is defined as

$$ARI = \frac{2(N_{00}N_{11} - N_{01}N_{10})}{(N_{00} + N_{01})(N_{01} + N_{11}) + (N_{00} + N_{10})(N_{10} + N_{11})} \quad (3.29)$$

1463 The adjusted Rand Index is 1 when the clusterings are identical, and 0 when the Rand Index  
1464 is equal to its expected value.

#### 1465 Clustering as random variables

If we take any random element of  $D$ , the probability that this element is in cluster  $C_k$  of clustering  $\mathcal{C}$  is

$$P(K = k) = \frac{n_k}{n} \quad (3.30)$$

1466 this defines a probability distribution, which makes the clustering a random variable. Any  
1467 clustering can be considered as a random variable this way.

This means that we can measure any of the information theoretic quantities defined in section 3.3.4 with respect to clusterings. For example, the entropy of a clustering is

$$H(\mathcal{C}) = - \sum_{k=1}^K \frac{n_k}{n} \log \frac{n_k}{n} \quad (3.31)$$

If we have two clusterings, the joint probability distribution of these clusterings is defined as

$$P(K = k, K' = k') = \frac{|C_k \cap C'_{k'}|}{n} \quad (3.32)$$

1468 The joint distribution allows us to define the mutual information between two clusterings,  
1469  $I(\mathcal{C}; \mathcal{C}')$  (Meilă, 2007).

1470 **Information based similarity measures**

The mutual information between two clusterings is a similarity measure, with  $I(\mathcal{C}; \mathcal{C}') = 0$  if  $\mathcal{C}$  and  $\mathcal{C}'$  are completely different, and  $I(\mathcal{C}; \mathcal{C}') = H(\mathcal{C}) = H(\mathcal{C}')$  if  $\mathcal{C}$  and  $\mathcal{C}'$  are identical. This can be normalised in a number of different ways to make more similarity measures (Vinh, Epps, and Bailey, 2010)

$$NMI_{joint} = \frac{I(\mathcal{C}; \mathcal{C}')}{H(\mathcal{C}, \mathcal{C}')} \quad (3.33)$$

$$NMI_{max} = \frac{I(\mathcal{C}; \mathcal{C}')}{\max\{H(\mathcal{C}), H(\mathcal{C}')\}} \quad (3.34)$$

$$NMI_{sum} = \frac{2I(\mathcal{C}; \mathcal{C}')}{H(\mathcal{C}) + H(\mathcal{C}')} \quad (3.35)$$

$$NMI_{sqrt} = \frac{I(\mathcal{C}; \mathcal{C}')}{\sqrt{H(\mathcal{C})H(\mathcal{C}')}} \quad (3.36)$$

$$NMI_{min} = \frac{I(\mathcal{C}; \mathcal{C}')}{\min\{H(\mathcal{C}), H(\mathcal{C}')\}} \quad (3.37)$$

We can control for chance similarities between the two clusterings by measuring the *adjusted mutual information* between the clusterings. This is defined as

$$AMI_{sum} = \frac{I(\mathcal{C}; \mathcal{C}') - E\{I(\mathcal{C}; \mathcal{C}')\}}{\frac{1}{2}[H(\mathcal{C}) + H(\mathcal{C}')] - E\{I(\mathcal{C}; \mathcal{C}')\}} \quad (3.38)$$

1471 The first term in the denominator, taking the average of the marginal entropies, can be re-  
 1472 placed by taking the maximum, minimum, or the geometric mean (Vinh, Epps, and Bailey,  
 1473 2010).

1474 **Information based metrics**

The variation of information between two clusterings  $VI(\mathcal{C}; \mathcal{C}')$  (see section 3.3.4) is a metric on the space of clusterings (Meilă, 2007). That is,

$$VI(\mathcal{C}; \mathcal{C}') \geq 0 \quad (3.39)$$

$$VI(\mathcal{C}; \mathcal{C}') = 0 \iff \mathcal{C} = \mathcal{C}' \quad (3.40)$$

$$VI(\mathcal{C}; \mathcal{C}') = VI(\mathcal{C}'; \mathcal{C}) \quad (3.41)$$

$$VI(\mathcal{C}; \mathcal{C}'') \leq VI(\mathcal{C}; \mathcal{C}') + VI(\mathcal{C}'; \mathcal{C}'') \quad (3.42)$$

Another metric is the *information distance* (Vinh, Epps, and Bailey, 2010)

$$D_{max} = \max\{H(\mathcal{C}), H(\mathcal{C}')\} - I(\mathcal{C}; \mathcal{C}') \quad (3.43)$$

Both of these can be normalised

$$NVI(\mathcal{C}; \mathcal{C}') = 1 - \frac{I(\mathcal{C}; \mathcal{C}')}{H(\mathcal{C}, \mathcal{C}')} \quad (3.44)$$

$$d_{max} = 1 - \frac{I(\mathcal{C}; \mathcal{C}')}{\max\{H(\mathcal{C}), H(\mathcal{C}')\}} \quad (3.45)$$

#### 1475 Comparing detected communities and anatomical divisions

1476 In order to quantify the difference or similarity between the communities detected in our cor-  
 1477 relation network and the anatomical classification of the cells in that network, we considered  
 1478 the communities and the anatomical regions as clusters in two different clusterings,  $\mathcal{C}_{comm}$   
 1479 and  $\mathcal{C}_{anat}$ , respectively. We then measured the similarity between the clusterings using the  
 1480 mutual information, the adjusted mutual information, and the normalised mutual informa-  
 1481 tion. We measured the difference between, or the distance between, the clusterings using the  
 1482 variation of information, the normalised variation of information, and the normalised infor-  
 1483 mation distance. We also measured the difference between the clusterings using the adjusted  
 1484 Rand Index, just to use a non-information based measure.

1485 We took all of these measures for communities detected using different time bin widths.  
 1486 This gave us an idea of the effect of time bin width on correlation networks in neural ensem-  
 1487 bles relative to anatomical regions within those ensembles.

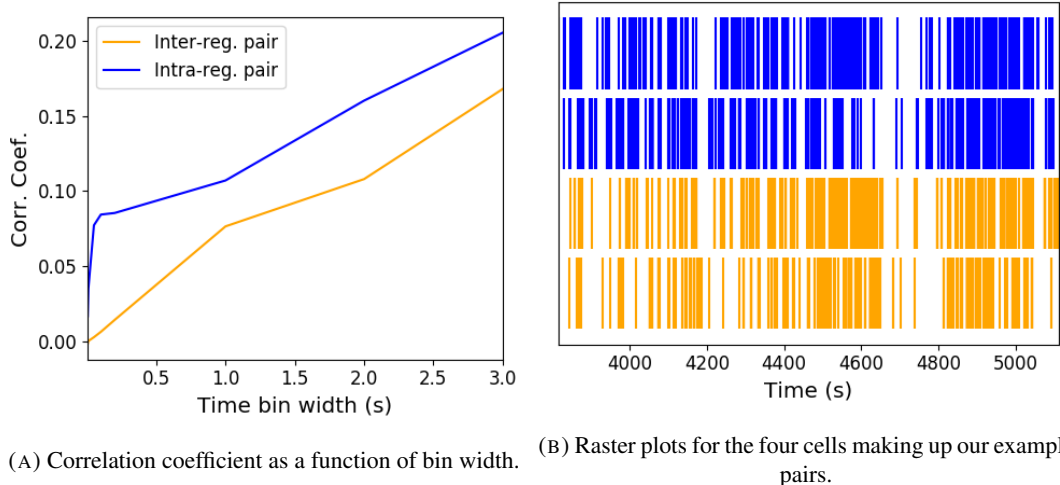
## 1488 3.4 Results

1489 Note that in the following text, we refer to the correlation coefficient between two sequences  
 1490 of spike counts from two different cells as the *total correlation*. We refer to the correlation  
 1491 between spike counts in response to a certain stimulus as the *spike count correlation* aka  
 1492 *noise correlation*, and we refer to the correlation between mean or expected responses to  
 1493 different stimuli as the *signal correlation* (Cohen and Kohn, 2011).

1494 The nine different brain regions from which we had data were the caudate putamen (CP),  
 1495 frontal motor cortex (FrMoCtx), hippocampus (HPF), lateral septum (LS), midbrain (MB),  
 1496 primary visual cortex (V1), superior colliculus (SC), somatomotor cortex (SomMoCtx), and  
 1497 thalamus (TH).

1498 **3.4.1 Average correlation size increases with increasing time bin width**

1499 First we inspected the affect of time bin width on total correlations. We know that using short  
 1500 time bins results in artificially small correlation measurements (Cohen and Kohn, 2011), so  
 1501 we expected to see an increase in correlation amplitude with increasing time bin width. That  
 1502 is exactly what we observed. Taking 50 cells at random, we calculated the total correla-  
 1503 tion between every possible pair of these cells, using different time bin widths ranging from  
 1504 0.005s to 3s. We found that the longer the time bin width, the greater the correlations (see  
 1505 figure 3.4a).



(A) Correlation coefficient as a function of bin width. (B) Raster plots for the four cells making up our example pairs.

FIGURE 3.3: (A) An example of the correlation coefficients between two different pairs of cells, one where both cells are in the same brain region (intra-regional pair), and one where both cells are in different brain regions (inter-regional pair). The correlation coefficients have been measured using different time bin widths, ranging from 5ms to 3s. Note the increasing amplitude of the correlations with increasing bin width. (B) A raster plot showing the spike times of each pair of cells.

1506 We also separated the positively correlated pairs from the negatively correlated pairs  
 1507 using the mean correlation of each pair across all bin widths (see section 3.3.2). We found  
 1508 that the positively correlated pairs become more positively correlated with increasing time bin  
 1509 width, and the negatively correlated pairs become more negatively correlated with increasing  
 1510 time bin width (see figures 3.4b and 3.4c).

1511 In figure 3.3a we plot correlations from two example pairs, one pair from within a region,  
 1512 and one pair between regions. It can be seen that the correlation coefficient increases with  
 1513 bin width. The correlations can be observed by eye in the raster plot for these cells in figure  
 1514 3.3b.

1515 When taking the mean across all pairs, the positively correlated pairs dominate in terms  
 1516 of both number of pairs, and amplitude of correlations. Therefore the mean across all pairs

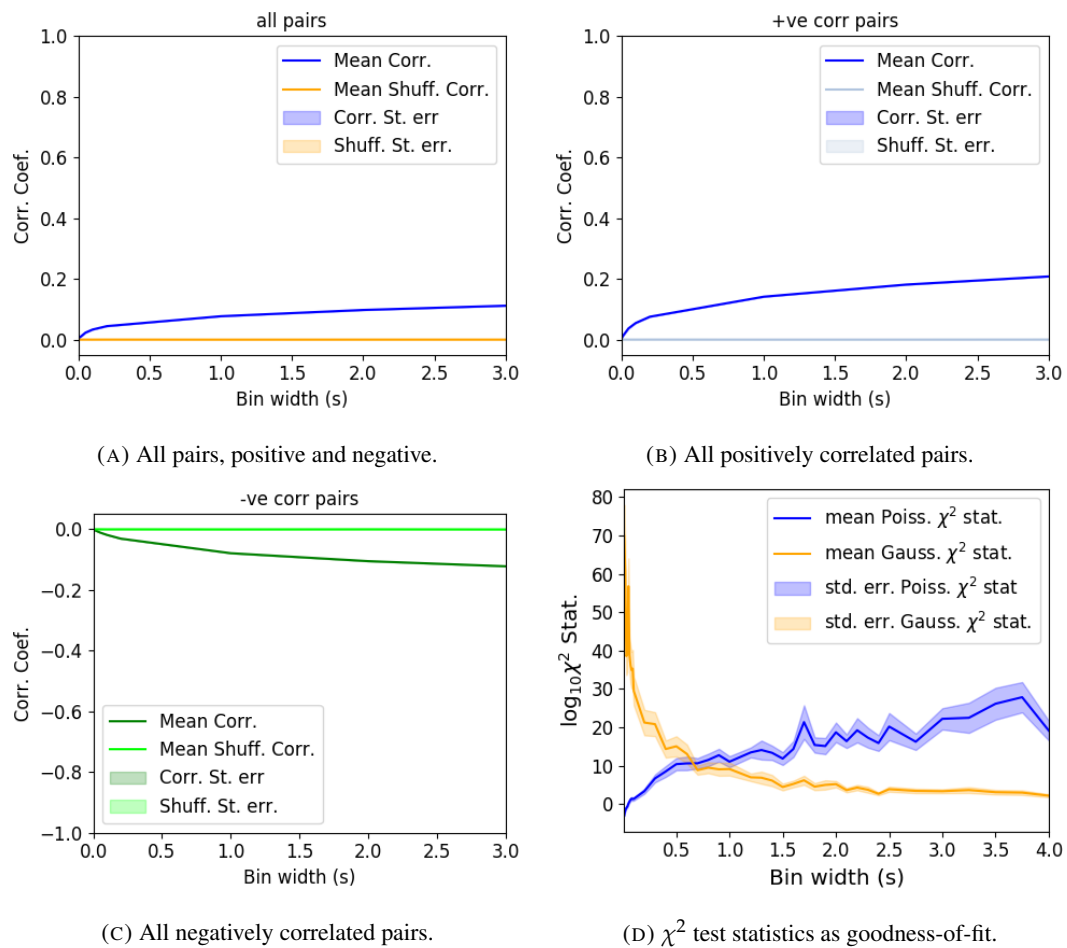


FIGURE 3.4: Mean correlation coefficients measured from pairs of 50 randomly chosen neurons. (A) All possible pairs, (B) positively correlated pairs, and (C) negatively correlated pairs. (D) Mean and standard error of  $\chi^2$  test statistics for Poisson and Gaussian distributions fitted to neuron spike counts.

1517 is positive.

1518 These results were observed in each of the three mouse subjects from which we had data.

1519 **3.4.2 Goodness-of-fit for Poisson and Gaussian distributions across increasing  
1520 time bin widths**

1521 We wanted to investigate if the width of the time bin used to bin spike times into spike counts  
1522 had an effect on the distribution of spike counts. We used the  $\chi^2$  statistic as a goodness-of-fit  
1523 measure for Poisson and Gaussian (normal) distributions to the spike count of 100 randomly  
1524 chosen neurons for a number of bin widths ranging from 0.01s to 4s. For the  $\chi^2$  statistic, the  
1525 higher the value, the worse the fit.

1526 We expected a Poisson distribution to be a better fit for shorter time bin widths because  
1527 spike counts must be non-negative, therefore any distribution of spike counts with mass dis-  
1528 tributed at or close to 0 will be skewed. The distribution of spike counts is more likely to be  
1529 distributed close to 0 when the time bin widths used to bin spike times into spike counts are  
1530 small relative to the amount of time it takes for a neuron to fire an action potential ( $\sim 1\text{ms}$  in  
1531 the case of non-burst firing neurons).

1532 We expected a Gaussian distribution to be a better fit for longer time bin widths, because  
1533 a Poisson distribution with a large rate is well approximated by a Gaussian distribution with  
1534 mean and variance equal to the Poisson rate. Therefore, a Gaussian distribution would ap-  
1535 proximate the mean of a collection of large spike counts, and have more flexibility than a  
1536 Poisson distribution to fit the variance.

1537 We found that that a Poisson distribution is the best fit for shorter time bins less than 0.7s  
1538 in length. Then a Gaussian distribution is a better fit for time bins greater than 0.7s in length  
1539 (see figure 3.4d).

1540 **3.4.3 Differences between and inter- and intra- regional correlations decrease  
1541 with increasing bin width**

1542 We investigated the differences in distribution between inter-regional correlations, i.e. corre-  
1543 lations between neurons in different brain regions, and intra-regional correlations, i.e. corre-  
1544 lations between neurons in the same brain region.

1545 Firstly, we investigated these quantities for all possible pairs of  $\sim 500$  neurons taken  
1546 from across all the 9 brain regions from which we had data. We distributed these neurons as  
1547 evenly as possible across all of the regions, so that cells from one region would not dominate  
1548 our data. We observed that the mean intra-regional correlations were always higher than the

mean inter-regional correlations for every value of time bin width used. We also observed that as the time bin width increased these mean correlations increased and the difference between the mean inter-regional and intra-regional correlations grew (see figure 3.5 (Left)).

Stringer et al. (2019) had a similar finding using the same data. They used only one value for the time bin width, 1.2s. Using this time bin width to bin spike times and measure total correlations, they found that the mean ‘within-region’ correlations were always greater than the ‘out-of-region’ correlations (Stringer et al., 2019). The figure from their paper showing this result can be seen in figure 3.5 (Right).

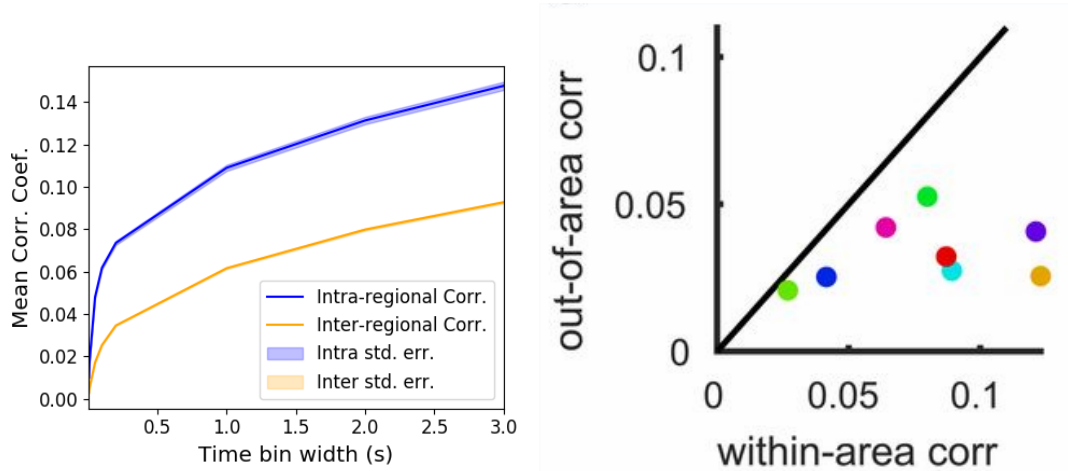
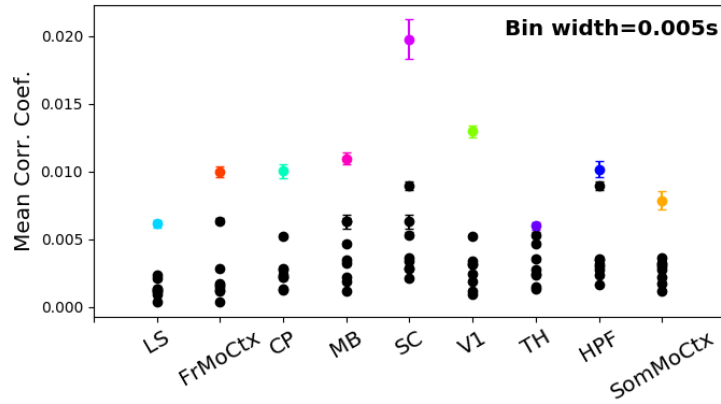


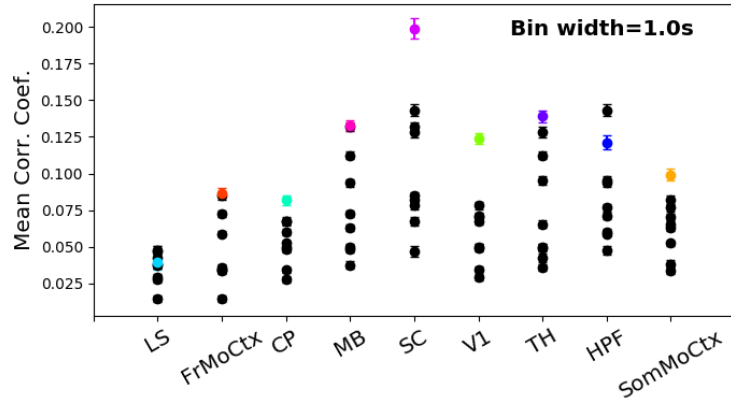
FIGURE 3.5: (Left)The mean intra-region and inter-region correlations using all possible pairs of  $\sim 500$  neurons, spread across 9 different brain regions. (Right) Courtesy of Stringer et al. (2019), mean inter-regional (out-of-area) correlation coefficients vs mean intra-regional (within-area) correlation coefficients for a bin width of 1.2s. Note that the intra-regional coefficients are higher in each case.

Examples of the correlations of one intra-regional pair and one inter-regional pair can be seen in figure 3.3.

Secondly, we separated those pairs into intra-regional and inter-regional groups. We noted that the mean intra-regional correlations (coloured dots in figures 3.6a and 3.6b) for a given region tended to be higher than the mean inter-regional correlations (black dots in figures 3.6a and 3.6b) involving cells from that region. However, in contrast with our previous result, we noted that the difference between the mean intra-regional correlations and most highly correlated inter-regional correlations reduced as we increased the time bin width (see figures 3.6a and 3.6b). This shows that the mean correlations shown in figure 3.5 are not distributed evenly across all region pair combinations.



(A) Mean inter-regional and intra-regional correlations using a time bin width of 5ms.



(B) Mean inter-regional and intra-regional correlations using a time bin width of 1s.

FIGURE 3.6: The mean intra-regional correlations (coloured dots) and mean inter-regional correlations (black dots) for a given region, indicated on the x-axis, for different time bin widths. Each black dot represents the mean inter-regional correlations between the region indicated on the x-axis and one other region. (A) shows these measurements when we used a time bin width of 5ms. (B) shows these measurements when we used a time bin width of 1s. Note that the difference between the mean inter-regional correlations and mean intra-regional correlations is smaller for 1s bins.

Finally, to see these regional mean correlations in a bit more detail, to examine the individual pair combinations in particular, we displayed these data in a matrix of mean correlations (see figure 3.7), showing the mean intra-regional correlations on the main diagonal, and the mean inter-regional correlations off diagonal. Comparing a version of this figure created using a short time bin width of 5ms (figure 3.7a) and a version using a longer time bin width of 1s (figure 3.7b) we observed that the mean intra-regional correlations are always relatively high in comparison to the mean inter-regional correlations, but the mean correlations in some inter-regional pairs are relatively much higher when using the longer time bin width.

This could indicate information being processed quickly at a local or within-region level, and the local representations of this information spreading between regions at longer timescales.

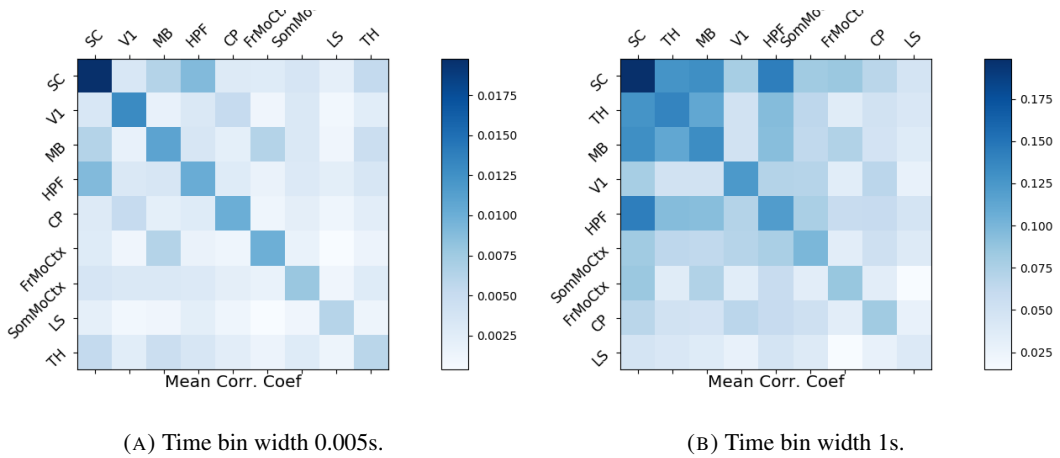


FIGURE 3.7: Mean inter-regional (main diagonal) and intra-regional (off diagonal) correlation coefficients. (A) Shows these measurements when spike times were binned using 5ms time bins. (B) Shows the same, using 1s time bins. Note that the matrices are ordered according to the main diagonal values, therefore the ordering is different in each subfigure.

These results were consistent across the three mouse subjects. But, the relative magnitudes of the mean intra-regional and inter-regional correlations were not consistent. For example, the region with the highest mean intra-regional correlations when using 1s bin widths for subject one is the superior colliculus (SC), but for subject two it is the midbrain (MB).

#### 3.4.4 Connected and divided structure in correlation based networks reduces in dimension with increasing bin width

We used the correlation measurements to create weighted undirected graphs/networks where each node represents a neuron, and the weight of each edge is the pairwise correlation between those neurons represented by the nodes at either end of that edge. We aimed to find

1586 communities of neurons within these networks, and compare the structure of these commu-  
1587 nities to the anatomical division of those neurons. The first step of this process involved  
1588 applying the ‘spectral rejection’ technique developed by Humphries et al (2019) (Humphries  
1589 et al., 2019). This technique compares our data network to a chosen null network model, and  
1590 finds any additional structure in the data network beyond that which is captured in the null  
1591 network model (if there is any such structure).

1592 By comparing the eigenspectrum of the data network to the eigenspectrum of many sam-  
1593 ples from the null network model, this technique allows us to estimate the dimensionality of  
1594 the additional structure in the data network, and gives us a basis for that vector space. It also  
1595 divides the additional structure into connected structure, and  $k$ -partite (or divided) structure.  
1596 For example, if our algorithm found two dimensions of additional connected structure, and  
1597 one dimension of additional divided structure. We might expect to find three communities,  
1598 that is groups more strongly connected within group than without, and we might expect to  
1599 find bi-partite structure, that is two sets that are more strongly connected between groups  
1600 than within groups.

1601 The technique also finds which nodes contribute to this additional structure, and divides  
1602 our data network into signal and noise networks. The details of spectral rejection and node  
1603 rejection can be found in sections 3.3.5 and 3.3.5 respectively, and a full overview can be  
1604 found in (Humphries et al., 2019).

1605 We chose the sparse weighted configuration model (see section 3.3.5) as our null network  
1606 model. This model matches the sparsity and the total weight of the original network but  
1607 distributes the weight at random across the sparse network.

1608 We applied the spectral rejection method to our networks based on total correlations using  
1609 different values for the time bin width. We observed that for smaller time bin widths, our data  
1610 networks had both  $k$ -partite structure, and community structure. As the width of the time bin  
1611 increased, we found that the  $k$ -partite structure disappeared from our data networks, and the  
1612 dimension of the community structure reduced in two of the three mice from which we had  
1613 data (see figure 3.8).

### 1614 **3.4.5 Detecting communities in correlation based networks**

1615 We applied the community detection procedure described in section 3.3.5 to our signal net-  
1616 works for our various time bin widths. We detected a greater number of smaller communities  
1617 at shorter time bin widths, and a smaller number of larger communities for longer time bin  
1618 widths (see figure 3.9). This was expected after the results found in section 3.4.4. We found

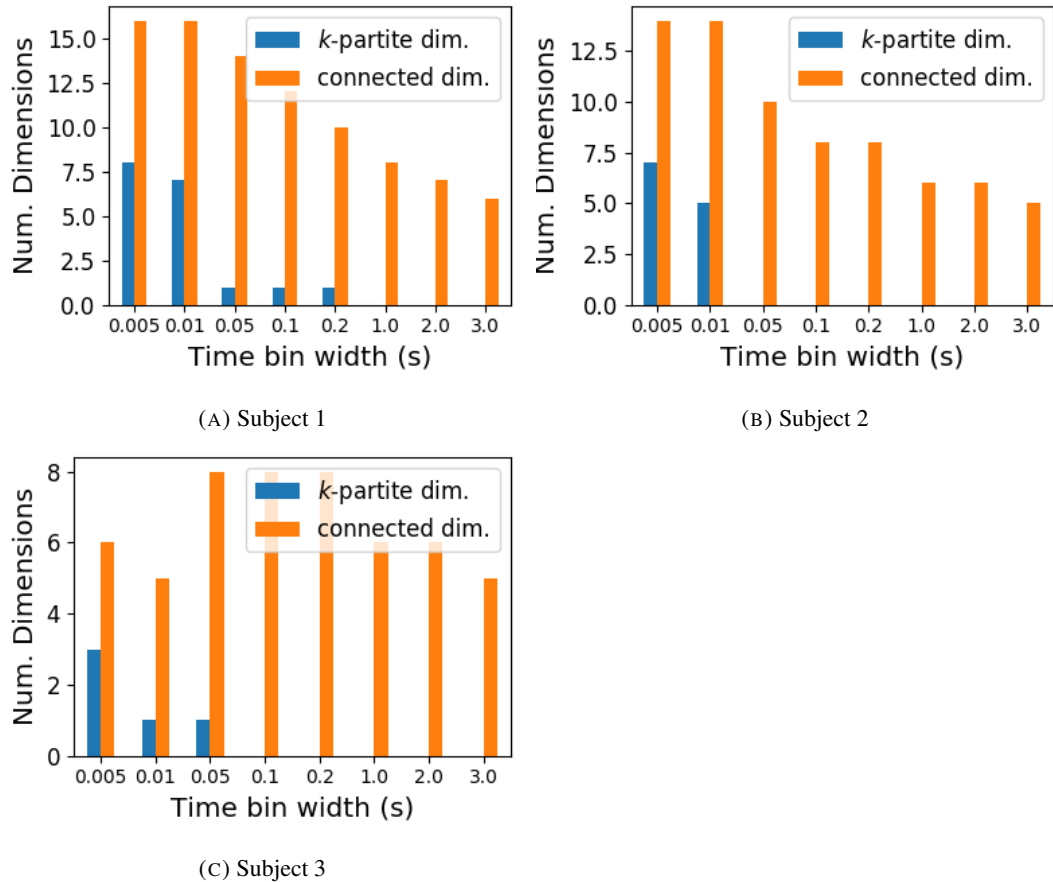


FIGURE 3.8: The number of dimensions in the *k*-partite and connected structure in the correlation based networks beyond the structure captured by a sparse weighted configuration null network model (see section 3.3.5), shown for different time bin widths. Note that the *k*-partite structure disappears for time bin width greater than 200ms for all three subjects. The dimension of the connected structure reduces with increasing bin width for 2 of the 3 subjects (top row).

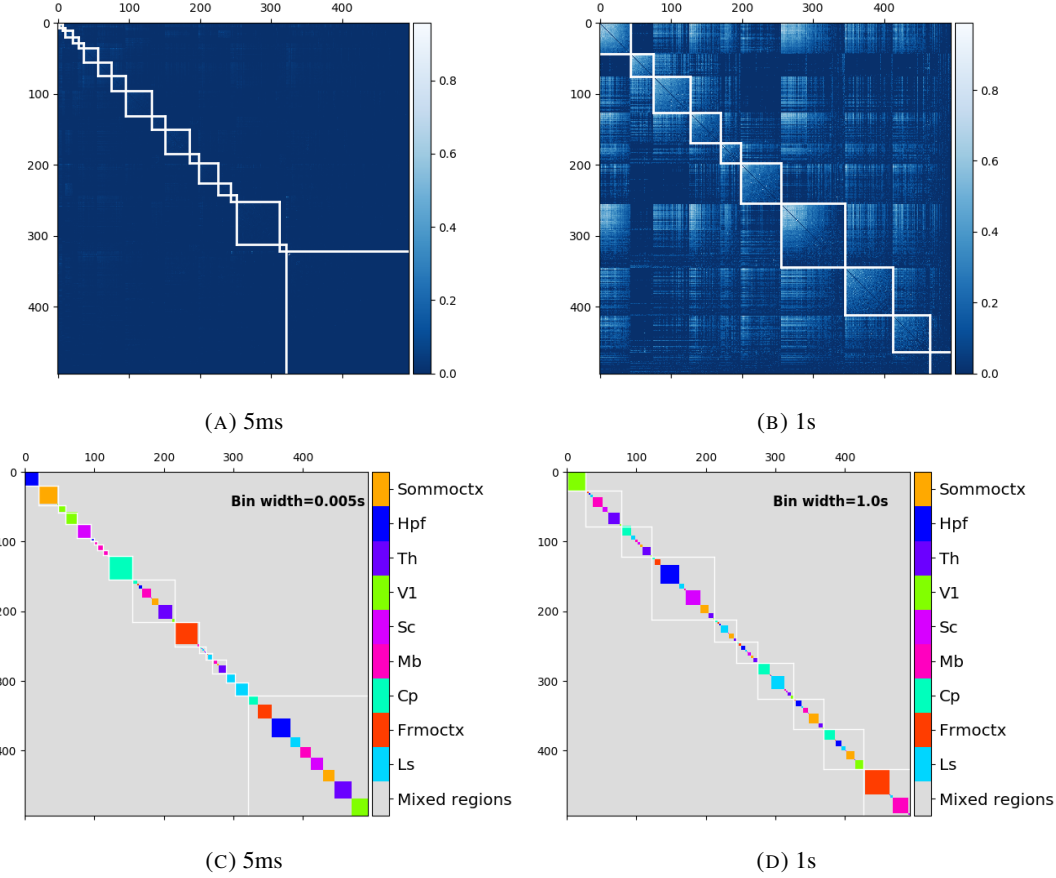


FIGURE 3.9: (A-B) Correlation matrices with detected communities indicated by white lines. Each off main diagonal entry in the matrix represents a pair of neurons. Those entries within a white square indicate that both of those neurons are in the same community as detected by our community detection procedure. Matrices shown are for 5ms and 1s time bin widths respectively. Main diagonal entries were set to 0. (C-D) Matrices showing the anatomical distribution of pairs along with their community membership. Entries where both cells are in the same region are given a colour indicated by the colour bar. Entries where cells are in different regions are given the grey colour also indicated by the colour bar.

1619 more dimensions of additional structure at shorter time bin widths, therefore we found more  
1620 communities at shorter time bin widths.

1621 We also noticed that at short time bin widths the communities detected tended to be  
1622 dominated by cells from one region. Whereas communities existing in networks created  
1623 using wider time bin widths tended to contain cells from many different brain regions. More  
1624 on this in the next section.

### 1625 **3.4.6 Functional communities resemble anatomical division at short timescales**

1626 In order to quantify the similarity of the communities detected to the anatomical division of  
1627 the cells. We treated both the anatomical division and the communities as clusterings of these  
1628 cells. We then used measures for quantifying the difference or similarity between clusterings  
1629 to quantify the difference or similarity between the detected communities and the anatomical  
1630 division. Details of these measures can be found in section 3.3.6 or in (Vinh, Epps, and  
1631 Bailey, 2010).

1632 We used two different types of measures for clustering comparison; information based  
1633 measures (see section 3.3.6) and pair counting based measures (see section 3.3.6). We include  
1634 one example of each in figure 3.10.

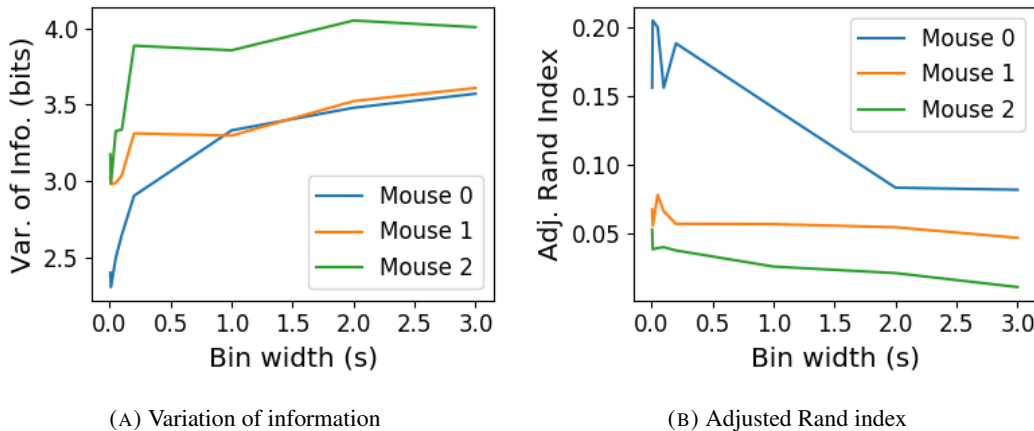
1635 The variation of information is the information based measure included in figure 3.10a.  
1636 This measure forms a metric on the space of clusterings. The larger the value for the variation  
1637 of information, the more different the clusterings.

1638 The adjusted Rand index is the pair counting based measure included in figure 3.10b. In  
1639 contrast with the variation of information, the adjusted Rand index is a normalised similarity  
1640 measure. The adjusted Rand index takes value 1 when the clusterings are identical, and takes  
1641 value 0 when the clusterings are no more similar than chance.

1642 Both measures indicated that the detected communities and the anatomical division of  
1643 the cells were more similar when we used shorter time bins widths (see figure 3.10). This  
1644 indicates that correlated behaviour in neuronal ensembles is more restricted to individual  
1645 brain regions at short timescales (< 250ms), and the correlated activity spreads out across  
1646 brain regions over longer time scales.

### 1647 **3.4.7 Conditional correlations & signal correlations**

1648 In light of the excellent research of Stringer et al (2019) showing that spontaneous behaviours  
1649 can drive activity in neuronal ensembles across the visual cortex and midbrain (Stringer et  
1650 al., 2019), we decided to control for the mouse's behaviour when performing our analyses.



(A) Variation of information

(B) Adjusted Rand index

FIGURE 3.10: (A) The variation of information is a measure of distance between clusterings. The distance between the anatomical ‘clustering’ and community detection ‘clustering’ increases with increasing time bin width. (B) The adjusted Rand index is a normalised similarity measure between clusterings. The anatomical and community detection clusterings become less similar as the time bin width increases.

1651 It is possible that our community detection process may be detecting communities across  
 1652 multiple brain regions at longer time scales due to aggregating neuronal activity driven by  
 1653 several spontaneous behaviours occurring during the time interval covered by a given time  
 1654 bin. A time bin of 1s, for example, could contain a spike count where those spikes were driven  
 1655 by different spontaneous behaviours. We aimed to investigate this possibility by applying our  
 1656 community detection analysis to conditional correlation measures.

1657 We used the top 500 principal components of a video of the mouse’s face as a measure of  
 1658 the mouse’s behaviour (see section 3.2.2). We modelled the spike counts as a linear combi-  
 1659 nation of the principal components using linear regression with ElasticNet regularisation (see  
 1660 section 3.3.3). Using this model, we quantified the expected spike count given the mouse’s  
 1661 behaviour  $E[X|Z_1, \dots, Z_{500}]$ .

1662 We used these expected values to measure  $\text{cov}(E[X|Z], E[Y|Z])$ , and we used that value,  
 1663 the covariance  $\text{cov}(X, Y)$ , and the *law of total covariance* (see section 3.3.3) to measure  
 1664  $E[\text{cov}(X, Y|Z)]$ . Here  $X$  and  $Y$  represent spike counts from individual cells, and  $Z$  is short-  
 1665 hand for the 500 principal components mentioned above. The two components of the co-  
 1666 variance,  $\text{cov}(E[X|Z], E[Y|Z])$  and  $E[\text{cov}(X, Y|Z)]$ , represent a ‘signal covariance’ and ex-  
 1667 pected value of a ‘spike count covariance’ respectively, analogous to the signal correlation  
 1668 and spike count correlation (Cohen and Kohn, 2011).

1669 We examined the means of these components for different values of the time bin width  
 1670 (see figure 3.11). We observed a consistent increase in  $E[\text{cov}(X, Y|Z)]$  as the time bin width  
 1671 increased. But we saw different trends for  $\text{cov}(E[X|Z], E[Y|Z])$  for each mouse.

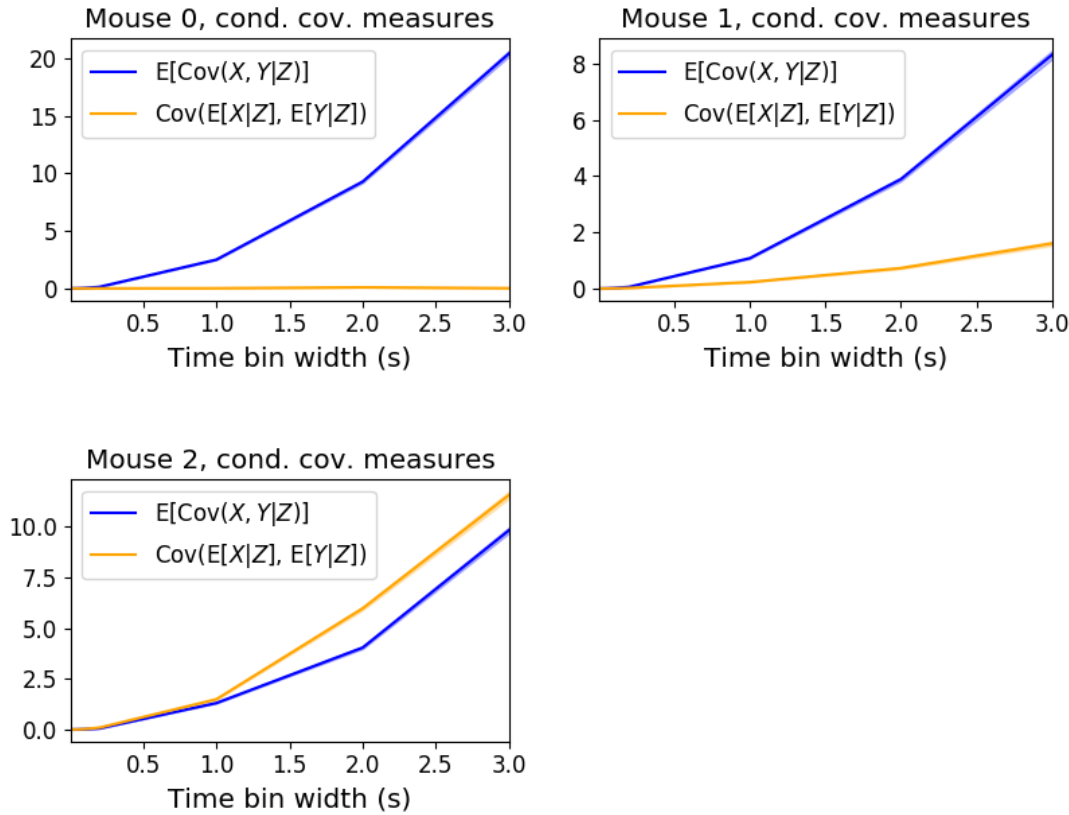


FIGURE 3.11: Comparing the components of the total covariance across different values for the time bin width. We observed a consistent increase in  $E[\text{cov}(X, Y|Z)]$  as the time bin width increased. But we saw different trends for  $\text{cov}(E[X|Z], E[Y|Z])$  for each mouse.

1672 Using  $\text{cov}(E[X|Z], E[Y|Z])$  we measured the signal correlation,  $\rho_{\text{signal}}$ , and using  $E[\text{cov}(X, Y|Z)]$   
 1673 we measured the event conditional correlation,  $\rho_{X,Y|Z}$  (see section 3.3.3 for more details).  
 1674 We saw a consistent increase in  $\rho_{X,Y|Z}$  as the time bin width increased, this corresponds to  
 1675 the result for  $E[\text{cov}(X, Y|Z)]$ . We observed different trends for  $\rho_{\text{signal}}$  for each mouse, this  
 1676 corresponds to the result for  $\text{cov}(E[X|Z], E[Y|Z])$ .

1677 We applied our network noise rejection and community detection process to networks  
 1678 based on the spike count correlations  $\rho_{X,Y|Z}$  and the signal correlations  $\rho_{\text{signal}}$ . We noted that  
 1679 the community detection on  $\rho_{X,Y|Z}$  behaved similarly to the community detection on the total  
 1680 correlation. We can see this in figures 3.13a and 3.13b. At very short time bin widths, we  
 1681 detect more communities, and those communities often contain cells from one brain region  
 1682 only. At longer time bin widths, we detect fewer communities, and those communities tend  
 1683 to contain cells from multiple brain regions. When we examine the distance between (or  
 1684 similarity between) the anatomical division of the cells, and the detected communities we  
 1685 notice that the two clusterings are more similar at shorter time bin widths (see figure 3.14).

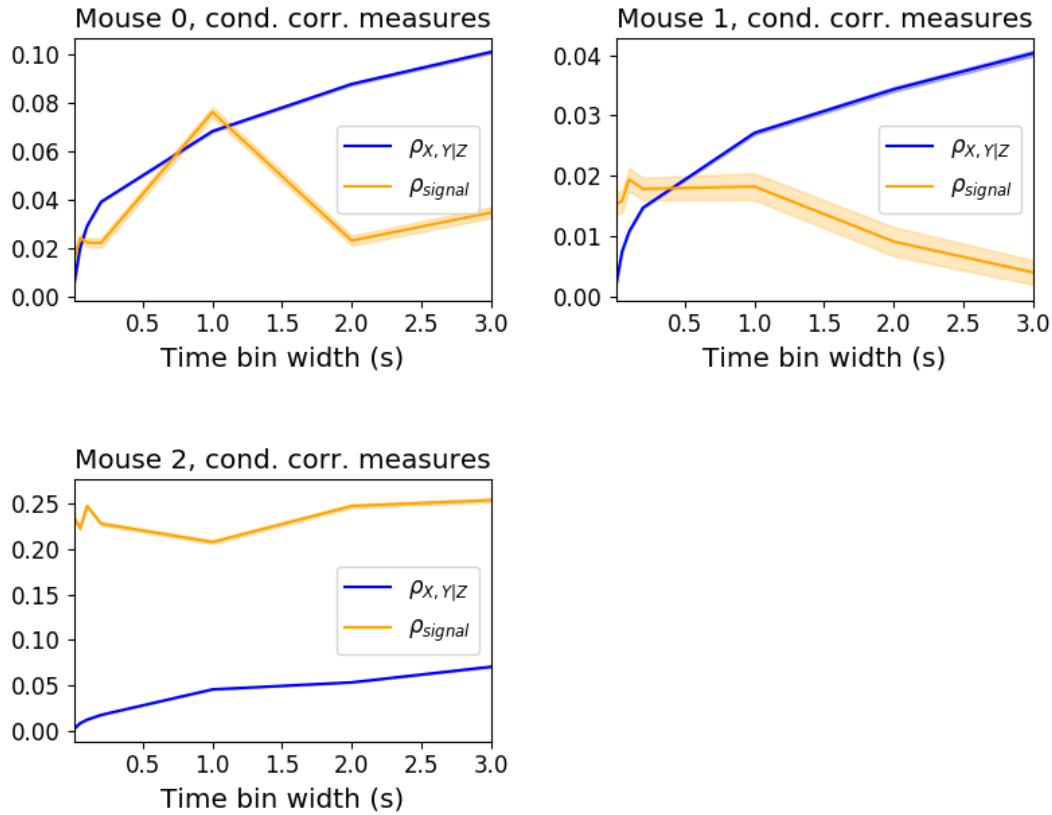


FIGURE 3.12: Comparing the components of the total covariance across different values for the time bin width. We saw a consistent increase in  $\rho_{X,Y|Z}$  as the time bin width increased in all three subjects. But we saw different trends in  $\rho_{signal}$  for each of the subjects.

When we applied the network noise rejection and community detection process to the networks based on the signal correlations  $\rho_{signal}$  we found the number of communities we detected reduced with increasing time bin width. But the number of communities detected was less than that for the total correlations or the spike count correlations. The communities detected always tended to contain cells from multiple regions at both short and long timescales (see figures 3.13c and 3.13d). The communities detected bore very little relation to the anatomical division of the cells. The adjusted Rand index between the community clustering and the anatomical ‘clustering’ is close to zero for every time bin width (see figure 3.15b). This indicates that the similarity between the clusterings is close to chance. We did observe a slight downward trend in the variation of information with increasing bin width (see figure 3.15a), but this is more likely due to a decrease in the number of communities detected rather than any relationship with anatomy.

We also observed that the network noise rejection process rejected some of the cells when applied to the network based on the signal correlations. This means that those cells

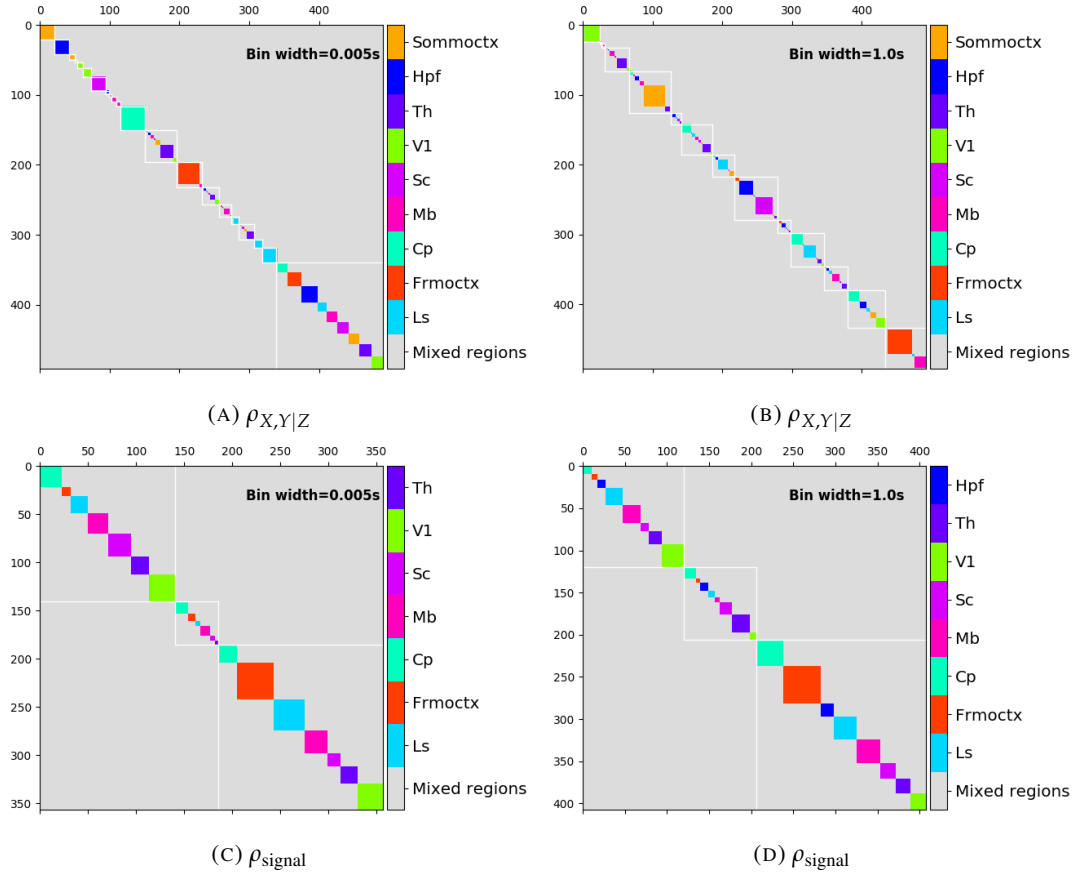


FIGURE 3.13: Matrices showing the regional membership of pairs by colour, and the communities in which those pairs lie. (A-B) Detected communities and regional membership matrix for network based on rectified spike count correlation  $\rho_{X,Y|Z}$ , using time bin widths of 0.005s and 1s respectively. (C-D) Detected communities and regional membership matrix for network based on rectified signal correlation  $\rho_{\text{signal}}$ , using time bin widths of 0.005s and 1s respectively.

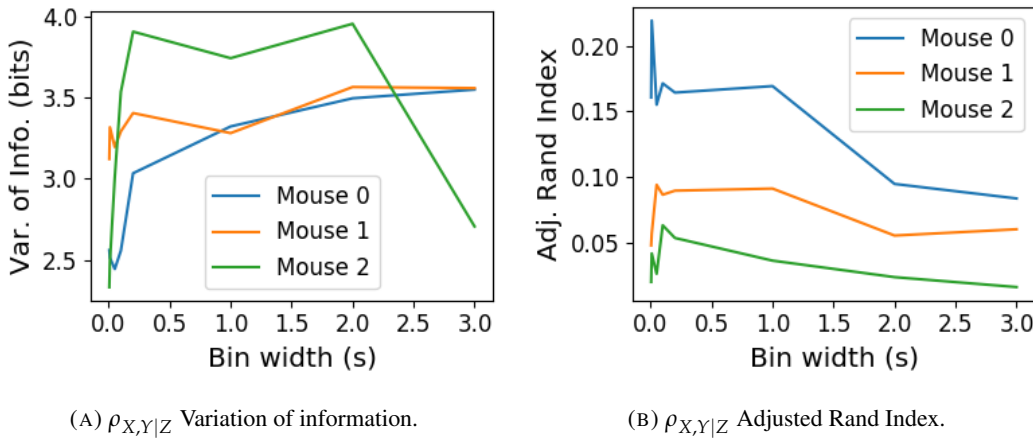
(A)  $\rho_{X,Y|Z}$  Variation of information.(B)  $\rho_{X,Y|Z}$  Adjusted Rand Index.

FIGURE 3.14: Distance and similarity measures between the anatomical division of the neurons, and the communities detected in the network based on the spike count correlations  $\rho_{X,Y|Z}$ . (A) The variation of information is a ‘distance’ measure between clusterings. The distance between the anatomical ‘clustering’ and the community clustering increases as the time bin width increases. (B) The adjusted Rand index is a similarity measure between clusterings. The detected communities become less similar to the anatomical division of the cells as the time bin width increases.

1700 did not contribute to the additional structure of the network beyond that captured by the  
 1701 sparse weighted configuration model. This is why the matrices in figures 3.13c and 3.13d are  
 1702 smaller than their analogues in figures 3.13a and 3.13b.

### 1703 3.4.8 Absolute correlations and negative rectified correlations

1704 At the moment, the network noise rejection protocol can only be applied to weighted undi-  
 1705 rected graphs with non-negative weights. This meant that we had to rectify our correlated  
 1706 networks before applying the network noise rejection and community detection process. We  
 1707 wanted to investigate what would happen if instead of rectifying the correlations, we used the  
 1708 absolute value, or reversed the signs of the correlations and then rectified.

1709 When we used the absolute value of the correlations, we found very similar results to  
 1710 those shown above for the rectified total correlations and the rectified spike count corre-  
 1711 lations. We detected more communities using shorter bin widths, and these communities  
 1712 were more similar to the brain’s anatomy than those communities detected using a longer bin  
 1713 width (see figure 3.16). The only exception being that we detected more communities. This  
 1714 could indicate that we detected both positively and negatively correlated communities, but  
 1715 we haven’t done any further investigation so we cannot say for sure.

1716 When we used the sign reversed rectified correlated networks, we tended to find fewer  
 1717 communities. Each community contained cells from many different anatomical regions, at

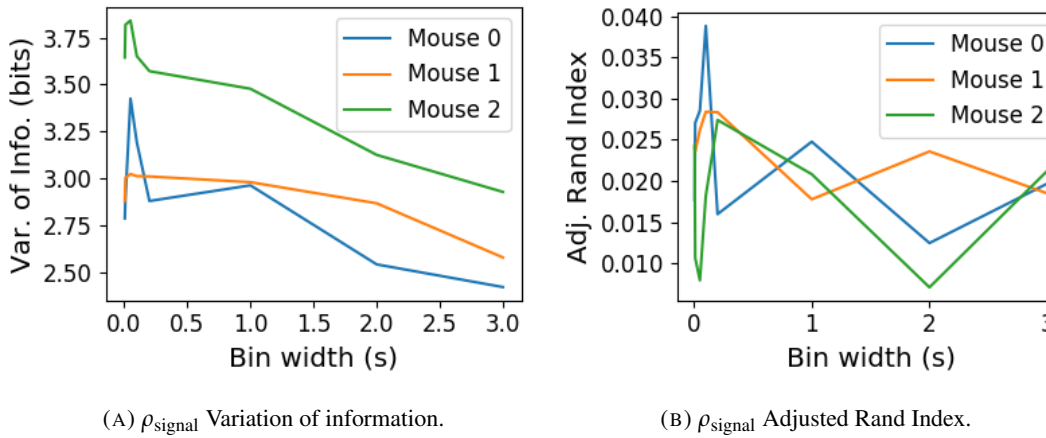
(A)  $\rho_{\text{signal}}$  Variation of information.(B)  $\rho_{\text{signal}}$  Adjusted Rand Index.

FIGURE 3.15: Distance and similarity measures between the anatomical division of the neurons, and the communities detected in the network based on the signal correlations  $\rho_{\text{signal}}$ . (A) The variation of information is a ‘distance’ measure between clusterings. The distance between the anatomical ‘clustering’ and the community clustering increases as the time bin width increases. (B) The adjusted Rand index is a similarity measure between clusterings. The detected communities become less similar to the anatomical division of the cells as the time bin width increases.

1718 both long and short bin widths (see figures 3.17a, 3.17b, 3.17c, 3.17d). The communities  
 1719 bore little relation to the anatomical distribution of the cells, this can be seen in figure 3.17f,  
 1720 the values close to zero indicate that the similarity between the two clusterings are around  
 1721 chance level. This indicates that there was not much structure in the negatively correlated  
 1722 networks beyond that captured by the sparse weighted configuration model.

## 1723 3.5 Discussion

1724 It is well established that the brain uses correlated behaviour in neuronal ensembles to repre-  
 1725 sent the information taken in through sensation (Cohen and Maunsell, 2009; Litwin-Kumar,  
 1726 Chacron, and Doiron, 2012; deCharms and Merzenich, 1996). However, most studies that  
 1727 examine the nature of these correlations in-vivo, study an ensemble of cells from only one  
 1728 or two brain regions (Cohen and Kohn, 2011; Wierzynski et al., 2009; Patterson et al., 2014;  
 1729 Girard, Hupé, and Bullier, 2001). Furthermore, recent results have shown that behaviour can  
 1730 drive correlated activity in multiple brain regions, including those not normally associated  
 1731 with motor control (Stringer et al., 2019; Gründemann et al., 2019; Allen et al., 2019). In this  
 1732 study, we utilised one of the newly recorded large datasets containing electrophysiological  
 1733 recordings from multiple brain regions simultaneously. We investigated correlated behaviour  
 1734 in these different brain regions and we investigated correlated behaviour between neurons in  
 1735 different regions, during spontaneous behaviour.

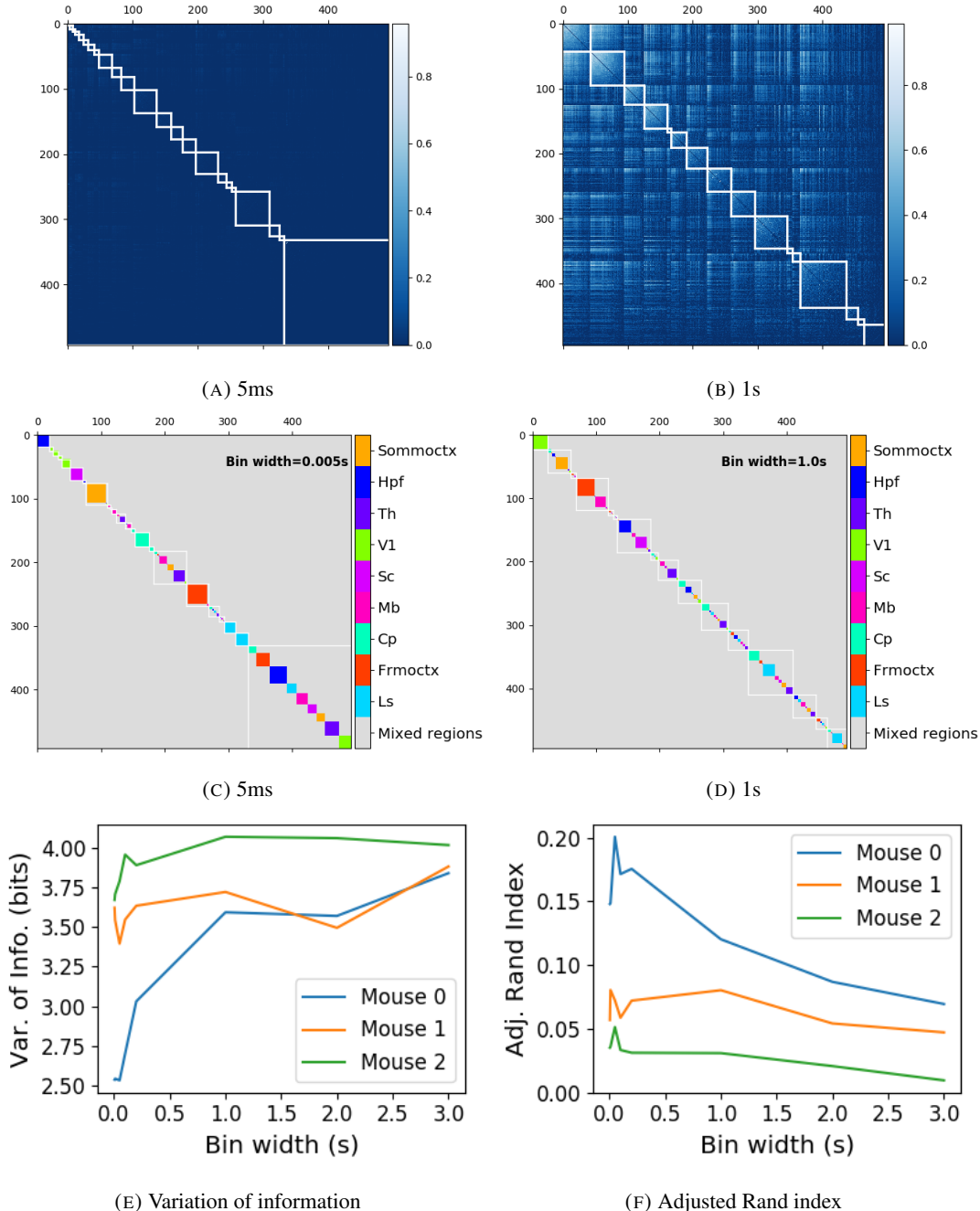


FIGURE 3.16: (A-B) Absolute correlation matrices with detected communities indicated by white lines. These communities are based on the absolute value of the total correlation between each pair of cells. Those entries within a white square indicate that both of those neurons are in the same community. Matrices shown are for 5ms and 1s time bin widths respectively. Main diagonal entries were set to 0. (C-D) Matrices showing the anatomical distribution of pairs along with their community membership. Regional membership is indicated by the colour bar. (E) Variation of information between the anatomical division of the cells, and the detected communities. (F) Adjusted Rand index between the anatomical division, and the detected communities.

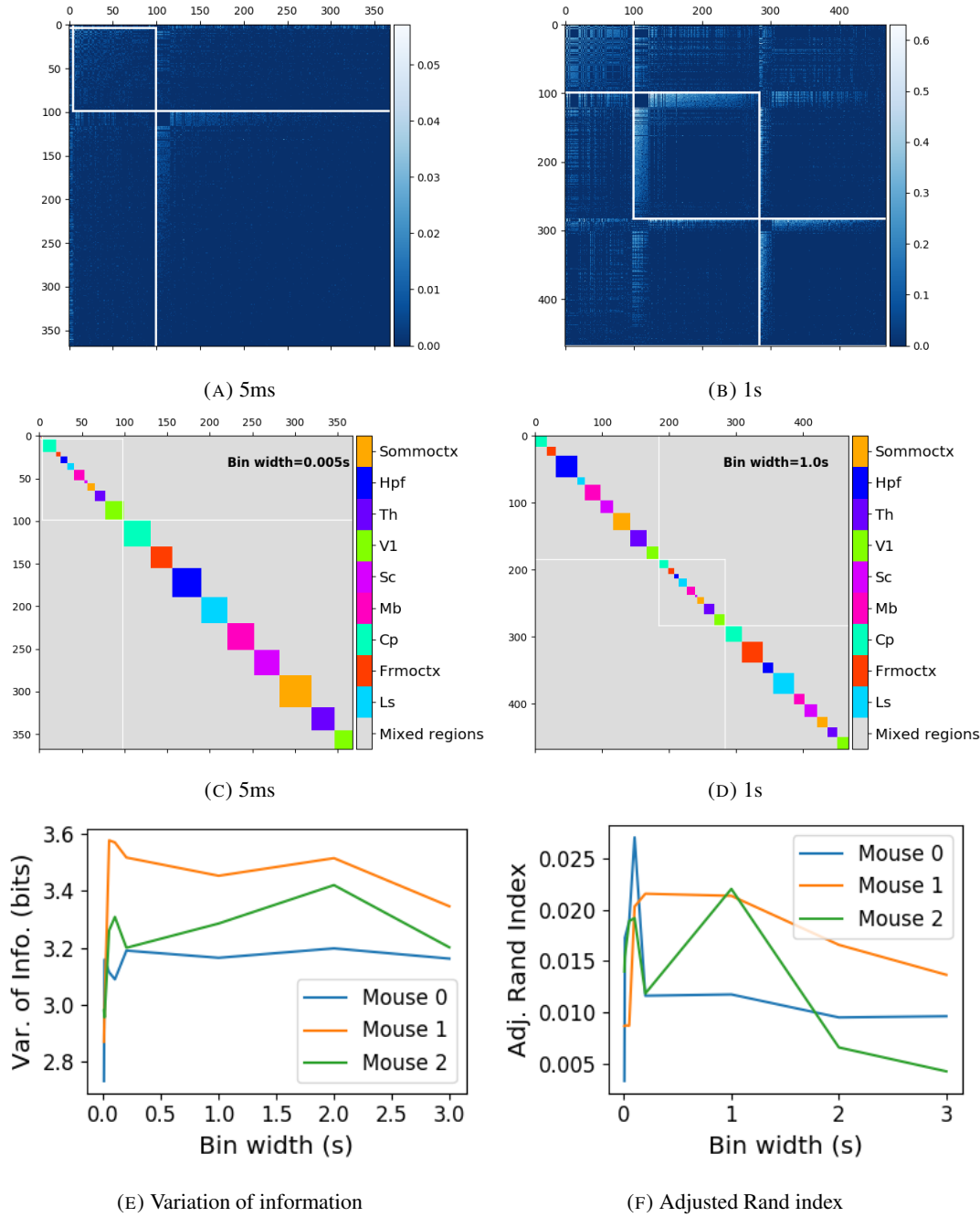


FIGURE 3.17: (A-B) Sign reversed rectified correlation matrices with detected communities indicated by white lines. Those entries within a white square indicate that both of those neurons are in the same community. Matrices shown are for 5ms and 1s time bin widths respectively. Main diagonal entries were set to 0. (C-D) Matrices showing the anatomical distribution of pairs along with their community membership. Regional membership is indicated by the colour bar. (E) Variation of information between the anatomical division of the cells, and the detected communities. (F) Adjusted Rand index between the anatomical division, and the detected communities.

1736 A number of studies have found that the timescale of correlated behaviour induced by a  
1737 stimulus can be modulated by the stimulus structure and behavioural context. For example,  
1738 the spike train correlations between cells in weakly electric fish are modulated by the spa-  
1739 tial extent of the stimulus (Litwin-Kumar, Chacron, and Doiron, 2012), and neurons in the  
1740 marmoset primary auditory cortex modulate their spike timing (and therefore correlation) in  
1741 response to stimulus features without modulating their firing rate (deCharms and Merzenich,  
1742 1996). Furthermore, the width of the time bins over which spike counts are measured has  
1743 been shown to have an effect on the magnitude of those correlations (Cohen and Kohn, 2011).  
1744 Despite this, very little research has been done comparing correlation measures from the same  
1745 dataset at different timescales. We investigated this by varying the time bin width used to bin  
1746 spike times into spike counts from as short as 5ms up to 3s.

1747 In order to further investigate the effect of these correlations at different timescales, we  
1748 regarded our neuronal ensemble as a weighted undirected graph, where each neuron is rep-  
1749 resented by a node, and the weight on each edge is the correlation between the neurons  
1750 connected by that edge. We then applied a novel clustering method from network science  
1751 (Humphries et al., 2019) to identify communities in these networks. Communities in a net-  
1752 work graph refer to sets of nodes that are more strongly connected to each other than the  
1753 nodes outside of their set. Another way to put this is to say that the nodes in a community  
1754 are more strongly connected than *expected*. What connection strength might be expected is  
1755 defined by a null network model. We chose a null network model that matched the sparsity  
1756 and total strength of our correlation based data networks. So, if two cells were in the same  
1757 community, those cells were more correlated than would be expected given the correlation  
1758 strength of their ensemble.

1759 These networks, and the community detection process, were completely agnostic of the  
1760 anatomical division of the cells in our ensemble. When we compared the detected commu-  
1761 nities with the anatomical division of the cells using distance and similarity measures for  
1762 clusterings, we found that the detected communities were more similar to the anatomical  
1763 division at shorter timescales. That is, when we used a wider time bin to count spikes, and  
1764 computed pairwise correlations with these spike counts, the correlated communities tended to  
1765 exist within anatomical regions at shorter timescales, and tended to span anatomical regions  
1766 at longer timescales. This could reflect localised functional correlations at short time scales  
1767 rippling outwards across brain regions at longer timescales. The brain may be processing  
1768 some information quickly locally, and carrying out further, perhaps more detailed, represen-  
1769 tation over a longer timescale across many regions using the representations that were just

1770 built locally.

1771 These changes in communities across timescales could also be driven by the anatomy  
1772 of the individual cells. For example, it may simply take longer to transmit action potentials  
1773 over longer distances, hence correlated activity over longer timescales will exist between  
1774 anatomical regions, rather than within. However, the switch to almost exclusively multi-  
1775 regional functional networks at 1s bin widths, rather than a mixture of multi-region, and  
1776 single-region suggests that the inter-regional correlations either overpower, or inhibit the  
1777 local correlations. So there may be more at play than just timescales.

1778 We acknowledged that the region spanning correlated communities that we detected at  
1779 longer time scales could exist due to collating activity driven by distinct spontaneous activi-  
1780 ties. In order to account for this, we modelled the spike counts as a linear function of the  
1781 top 500 principal components of a video of the mouse's face filmed simultaneously with the  
1782 electrophysiological readings. We applied our network noise rejection and community de-  
1783 tection process to the weighted undirected networks formed by the spike count correlations  
1784 (or noise correlations) and the signal correlations that we calculated using our model. For the  
1785 spike count correlation networks, we found much the same results as for the total correlations  
1786 as described above. For the signal correlations, the communities detected in these networks  
1787 bore little relation to the anatomical division of the cells. Recent findings have shown that  
1788 behavioural data accounts for correlations in many brain regions that would otherwise be  
1789 dismissed as noise (Stringer et al., 2019), our finding to shows that these correlations are still  
1790 governed by the timescale division between local communication and across-region commu-  
1791 nication.

1792 There is a lot of room for further investigation based on this research. For a start, the  
1793 data that we used here were collected from nine different regions in the mouse brain, but  
1794 none of these regions were part of the somatosensory cortex. Given that a mouse experiences  
1795 so much of its environment through its sense of smell, some data from this region would be  
1796 interesting to investigate. On the same theme, the mice in the experiment from which the  
1797 data were collected were headfixed and placed on a rotating ball, but were otherwise behav-  
1798 ing spontaneously. Had these mice been exposed to a visual, aural, or olfactory stimulus,  
1799 we could have examined the responses of the cells in the brain regions corresponding to vi-  
1800 sion, hearing, and olfaction, and compared these responses to the responses from the other  
1801 brain regions. Furthermore, we could have investigated the interaction between the sets of  
1802 responses.

1803 Another space for further investigation is the community detection. The algorithm that we

1804 used here never detects overlapping communities. But functional communities could indeed  
1805 have overlaps. Clustering methods that detect overlapping clusters do exist (Baadel, Thabtah,  
1806 and Lu, 2016). Applying one of those algorithms could yield some interesting results. Also,  
1807 the community detection algorithm that we used here cannot process graphs with negative  
1808 weights, this forced us to separate positive and negative correlations before applying our  
1809 network noise rejection and community detections process, or use the absolute value of our  
1810 correlations. A community detection algorithm that can work on weighted undirected graphs  
1811 with negative weights could yield some interesting results here.

1812 **Chapter 4**

1813 **A simple two parameter distribution  
1814 for modelling neuronal activity and  
1815 capturing neuronal association**

1816 *Abstract*

1817 Recent developments in electrophysiological technology have lead to an increase in the size  
1818 of electrophysiology datasets. Consequently, there is a requirement for new analysis tech-  
1819 niques that can make use of these new datasets, while remaining easy to use in practice. In  
1820 this work, we fit some one or two parameter probability distributions to spiking data collected  
1821 from a mouse exposed to visual stimuli. We show that the Conway-Maxwell-binomial dis-  
1822 tribution is a suitable model for the number of active neurons in a neuronal ensemble at any  
1823 given moment. This distribution fits these data better than binomial or beta-binomial distribu-  
1824 tions. It also captures the correlated activity in the primary visual cortex induced by stimulus  
1825 onset more effectively than simply measuring the correlations, at short timescales (< 10ms).  
1826 We also replicate the finding of Churchland et al (2010) relating to stimulus onset quenching  
1827 neural variability in cortical areas, and we show a correspondence between this quenching  
1828 and changes in one of the parameters of the fitted Conway-Maxwell-binomial distributions.

1829 **4.1 Introduction**

1830 Recent advances in electrophysiological technology, such as ‘Neuropixels’ probes (Jun et al.,  
1831 2017) have allowed extracellular voltage measurements to be collected from larger numbers  
1832 of cells than traditional methods, in multiple brain regions simultaneously, and routinely.  
1833 These larger datasets require innovative methods to extract information from the data in a  
1834 reasonable amount of time, ‘reasonable’ being subjective in this case.

1835 Theoretically, all the information at any given moment in an electrophysiological dataset  
1836 with  $n$  neurons could be captured by calculating the probability distribution for every possi-  
1837 ble spiking pattern. This would require defining a random variable with  $2^n$  possible values, a  
1838 task that quickly becomes impossible as  $n$  increases. Attempts at approximating this random  
1839 variable often involve measuring pairwise or higher order correlations (Schneidman et al.,  
1840 2006; Flach, 2013; Ganmor, Segev, and Schneidman, 2011). But pairwise correlations may  
1841 not be enough to characterise instantaneous neural activity (Tkačik et al., 2014). Further-  
1842 more, these kinds of models tend to ignore the temporal structure of neuronal data, in favour  
1843 of smaller model size, and scalability.

1844 Higher order correlations would be helpful here, but defining these correlations can be  
1845 tricky, never-mind quantifying them. If we use the interaction parameters arising from the  
1846 exponential family model as measures of higher order correlations, measuring these correla-  
1847 tions becomes computationally impractical quite quickly also (the number of ‘three neuron  
1848 correlations’ to measure scales with  $\binom{n}{3}$ ). In this paper, we dispense with measuring correla-  
1849 tions directly, and attempt to characterise correlated behaviour by measuring ‘association’; a  
1850 more general concept that includes correlation.

1851 In this work, we examined the ability of simple distributions to model the number of  
1852 active (spiking) neurons in a neuronal ensemble at any given timepoint. We compared a  
1853 little-known distribution named the Conway-Maxwell-binomial distribution to the binomial  
1854 distribution and the beta-binomial distribution. The binomial distribution is a probability dis-  
1855 tribution over the number of successes in a sequence of independent and identical Bernoulli  
1856 trials. The beta-binomial distribution is similar, but allows for a bit more flexibility while still  
1857 being a model for heterogeneity. Similar to the binomial and beta-binomial, the Conway-  
1858 Maxwell-binomial distribution is a probability distribution over the number of successes in a  
1859 series of Bernoulli trials, but allows over- and under-dispersion relative to the binomial dis-  
1860 tribution. This distribution should therefore be a good candidate for our purposes. We found  
1861 that Conway-Maxwell-binomial distribution was usually the best candidate of the three that

1862 we examined.

1863 We also observed some interesting changes in the number of active neurons in the primary  
1864 visual cortex and hippocampus at stimulus onset and some changes in this activity in the  
1865 thalamus which were sustained for the full duration of the stimulus presentation. This let us  
1866 know that there were some responses to model.

1867 We found that fitting a Conway-Maxwell-binomial distribution was a better method of  
1868 capturing association between neurons than measuring the spike count correlation for the  
1869 short time bins that we used (< 10ms).

1870 Finally, we also wanted to investigate parallels between the parameters of the Conway-  
1871 Maxwell-binomial distribution and quantities that have been established as relevant to sen-  
1872 sory processing. So, we replicated the findings made by Churchland et al. (2010) relating  
1873 to a reduction in neural variability at stimulus onset in the macaque cortical regions, but for  
1874 data taken from the mouse primary visual cortex. We compared these findings to the values  
1875 of the fitted Conway-Maxwell-binomial distribution parameters.

## 1876 4.2 Data

1877 We used data collected by Nick Steinmetz and his lab ‘CortexLab at UCL’ (Steinmetz, Caran-  
1878 dini, and Harris, 2019). The data can be found online <sup>1</sup> and are free to use for research  
1879 purposes.

1880 Two ‘Phase3’ Neuropixels (Jun et al., 2017) electrode arrays were inserted into the brain  
1881 of an awake, head-fixed mouse for about an hour and a half. These electrode arrays recorded  
1882 384 channels of neural data each at 30kHz and less than  $7\mu\text{V}$  RMS noise levels. The sites  
1883 are densely spaced in a ‘continuous tetrode’-like arrangement, and a whole array records  
1884 from a 3.8mm span of the brain. One array recorded from visual cortex, hippocampus, and  
1885 thalamus, the other array recorded from motor cortex and striatum. The data were spike-  
1886 sorted automatically by Kilosort and manually by Nick Steinmetz using Phy. In total 831  
1887 well-isolated individual neurons were identified.

### 1888 4.2.1 Experimental protocol

1889 The mouse was shown a visual stimulus on three monitors placed around the mouse at right  
1890 angles to each other, covering about  $\pm 135$  degrees azimuth and  $\pm 35$  degrees elevation.

---

<sup>1</sup><http://data.cortexlab.net/dualPhase3/>

1891 The stimulus consisted of sine-wave modulated full-field drifting gratings of 16 drift di-  
1892 rections ( $0^\circ, 22.5^\circ, \dots, 337.5^\circ$ ) with 2Hz temporal frequency and 0.08 cycles/degree spatial  
1893 frequency displayed for 2 seconds plus a blank condition. Each of these 17 conditions were  
1894 presented 10 times in a random order across 170 different trials. There were therefore 160  
1895 trials with a drifting-grating visual stimulus present, and 10 trials with a blank stimulus.

1896 **4.3 Methods**

1897 **4.3.1 Binning data**

1898 We converted the spike times for each cell into spike counts by putting the spike times into  
1899 time bins of a given ‘width’ (in milliseconds). We used time bins of 1ms, 5ms, and 10ms.  
1900 We used different time bin widths to assess the impact of choosing a bin width.

1901 **4.3.2 Number of *active* neurons**

1902 To count the number of active neurons in each neuronal ensemble, we split the time interval  
1903 for each trial into bins of a given width. We counted the number of spikes fired by each cell  
1904 in each bin. If a cell fired *at least* one spike in a given bin, we regarded that cell as active in  
1905 that bin. We recorded the number of active cells in every bin, and for the purposes of further  
1906 analysis, we recorded each cell’s individual spike counts.

1907 It should be noted that when we used a bin width of 1ms, the maximum number of  
1908 spikes in any bin was 1. For the wider time bins, some bins had spike counts greater than  
1909 1. Consequently when using a bin width of 1ms, the number of active neurons and the total  
1910 spike count of a given bin were identical. But for wider bin widths, the total spike count was  
1911 greater than the number of active neurons.

1912 So for the 1ms bin width, the activity of a neuron and the number of spikes fired by that  
1913 neuron in any bin can be modelled as a Bernoulli variable. But for wider time bins, only the  
1914 activity can be modelled in this way.

1915 **4.3.3 Moving windows for measurements**

1916 When taking measurements (e.g. moving average over the number of active neurons) or  
1917 fitting distributions (eg. the beta binomial distribution) we slid a window containing a certain  
1918 number of bins across the data, and made our measurements at each window position. For  
1919 example, when analysing 1ms bin data, we used a window containing 100 bins, and we slid

Bin width (ms)	Window size (bins)	Window size (ms)	Windows per trial
1ms	100	100ms	296
5ms	40	200ms	286
10ms	40	400ms	266

TABLE 4.1: Details of the different bin width and analysis window sizes used when binning spike times, and analysing those data.

1920 the window across the time interval for each trial moving 10 bins at a time. So that for  
 1921 3060ms of data, we made 296 measurements.

1922 For the 5ms bin width data, we used windows containing 40 bins, and slid the window 2  
 1923 bins at a time when taking measurements.

1924 For the 10ms bin width data, we used windows containing 40 bins, and slid the window  
 1925 1 bin at a time when taking measurements (see table 4.1 for concise details).

1926 By continuing to use windows containing 40 bins, we retained statistical power but sac-  
 1927 rificed the number of measurements taken.

1928 There was an interval between each trial with a grey image in place of the moving of  
 1929 the moving bar stimulus. This interval varied in time. But we included some of this interval  
 1930 when recording the data for each trial. We started recording the number of active neurons,  
 1931 and the number of spikes from each neuron from 530ms before each trial until 1030ms after  
 1932 each trial. This way, we could see the change in our measurements at the onset of a stimulus  
 1933 and the end of stimulus presentation.

1934 As mentioned in section 4.3.2, we recorded the number of active neurons in each bin, and  
 1935 the spike count for each neuron in each bin. The actual measurements we took using these  
 1936 data in each window were as follows:

1937 **Moving average** The average number of active cells in each window.

1938 **Moving variance** The variance of the number of active cells in each window.

1939 **Average correlation** We measured the correlation between the spike counts of each pair of  
 1940 cells in the ensemble, and took the average of these measurements.

1941 **Binomial  $p$**  We fitted a binomial distribution to the data in each window and recorded the  
 1942 fitted probability of success,  $p$  in each case.

1943 **Beta-binomial  $\alpha, \beta$**  We fitted a beta-binomial distribution to the data in each window, and  
 1944 recorded the values of the fitted shape parameters,  $\alpha$  and  $\beta$ , of each distribution.

1945 **Conway-Maxwell-binomial distribution  $p, \nu$**  We fitted a Conway-Maxwell-binomial dis-  
 1946 tribution to the data in each window, and recorded the fitted values of  $p$  and  $\nu$  for each  
 1947 distribution.

1948 **Log-likelihoods** We also recorded the log-likelihood of each of the fitted distributions for  
 1949 each window.

1950 **4.3.4 Fano factor**

The *Fano factor* of a random variable is defined as the ratio of the variable's variance to its mean.

$$F = \frac{\sigma^2}{\mu} \quad (4.1)$$

1951 We measured the Fano factor of the spike count of a given cell by measuring the mean and  
 1952 variance of the spike count across trials, and taking the ratio of those two quantities. When  
 1953 calculated in this way the Fano factor can be used as a measure of neural variability that  
 1954 controls for changes in the firing rate. This is similar to the calculation used in (Churchland  
 1955 et al., 2010).

1956 **4.3.5 Probability Distributions suitable for modelling ensemble activity**

1957 We present here three different probability distributions that could be suitable to model the  
 1958 number of active neurons in an ensemble. Each distribution has the set  $\{0, \dots, n\}$  as its sup-  
 1959 port, where  $n$  is the number of neurons in the ensemble. These are simple distributions with  
 1960 either two or three parameters each. However, we regard  $n$  as known when using these dis-  
 1961 tributions for modelling, so in effect each distribution has either one or two free parameters.

1962 **Association**

1963 *Association* between random variables is similar to the correlation between random variables  
 1964 but is more general in concept. The correlation is a measure of association; and association  
 1965 doesn't have a mathematical definition like correlation does. Essentially, the association  
 1966 between two random variables is their tendency to take the same or similar values. Positively  
 1967 associated variables tend to take the same value, and negatively associated variables tend to  
 1968 take different values. In this research, we work with probability distributions of the number of  
 1969 successes in a set of Bernoulli trials. These Bernoulli variables may or may not be associated.

1970 A probability distribution over the number of successes in  $n$  Bernoulli trials, where the  
 1971 Bernoulli variables may be associated, could constitute a good model for the number of active  
 1972 neurons in an ensemble of  $n$  neurons.

1973 **Binomial distribution**

The binomial distribution is a two parameter discrete probability distribution that can be thought of as a probability distribution the number of successes from  $n$  independent Bernoulli trials, each with the same probability of success. The parameters of the binomial distribution are  $n$  the number of trials, and  $0 \leq p \leq 1$ , the probability of success for each of these trials. A random variable with the binomial distribution can take values from  $\{0, \dots, n\}$ . The probability mass function of the distribution is

$$P(k; n, p) = \binom{n}{k} p^k (1-p)^{n-k} \quad (4.2)$$

1974 As a model for the activity of a neuronal ensemble, the main problem with the binomial  
 1975 distribution is that it treats each neuron, represented as a Bernoulli trial, as independent. It is  
 1976 well known that neurons are not independent, and that correlated behaviour between neurons  
 1977 is vital for representing sensory information (Cohen and Maunsell, 2009). The binomial dis-  
 1978 tribution falls short in this regard, but it is useful as performance benchmark when assessing  
 1979 the performance of other models.

1980 **Beta-binomial distribution**

1981 The beta distribution is the conjugate distribution of the binomial distribution. The beta-  
 1982 binomial distribution is the combination of the beta distribution and the binomial distribution,  
 1983 in that the probability of success for the binomial distribution is sampled from the beta dis-  
 1984 tribution. This allows the beta-binomial distribution to capture some over dispersion relative  
 1985 to the binomial distribution.

The beta-binomial distribution is a three parameter distribution,  $n$  the number of Bernoulli trials, and  $\alpha \in \mathbb{R}_{>0}$  and  $\beta \in \mathbb{R}_{>0}$  the shape parameters of the beta distribution. The probability mass function for the beta-binomial distribution is

$$P(k; n, \alpha, \beta) = \binom{n}{k} \frac{B(k + \alpha, n - k + \beta)}{B(\alpha, \beta)} \quad (4.3)$$

1986 where  $B(\alpha, \beta)$  is the beta function.

This probability distribution can be reparametrised in a number of ways. One of which defines new parameters  $\pi$  and  $\rho$  by

$$\pi = \frac{\alpha}{\alpha + \beta} \quad (4.4)$$

$$\rho = \frac{1}{\alpha + \beta + 1} \quad (4.5)$$

1987 This reparametrisation is useful because  $\pi$  acts as a location parameter analogous to the  $p$   
 1988 parameter of a binomial distribution. A value of  $\rho > 0$  indicates over-dispersion relative to a  
 1989 binomial distribution.

1990 As a model for the activity of a neuronal ensemble, the beta-binomial distribution is  
 1991 more suitable than a binomial distribution because the over-dispersion of the beta-binomial  
 1992 distribution can be used to model positive association between the neurons. An extreme  
 1993 example of this over-dispersion/positive association can be seen in figure 4.1b. In this figure,  
 1994 the neurons are positively associated and so tend to take the same value, consequently the  
 1995 probability mass of the beta-binomial distribution builds up close to  $k = 0$  and  $k = n$ . It is  
 1996 worth noting that the location parameter for each distribution has the same value,  $p = \pi =$   
 1997 0.5.

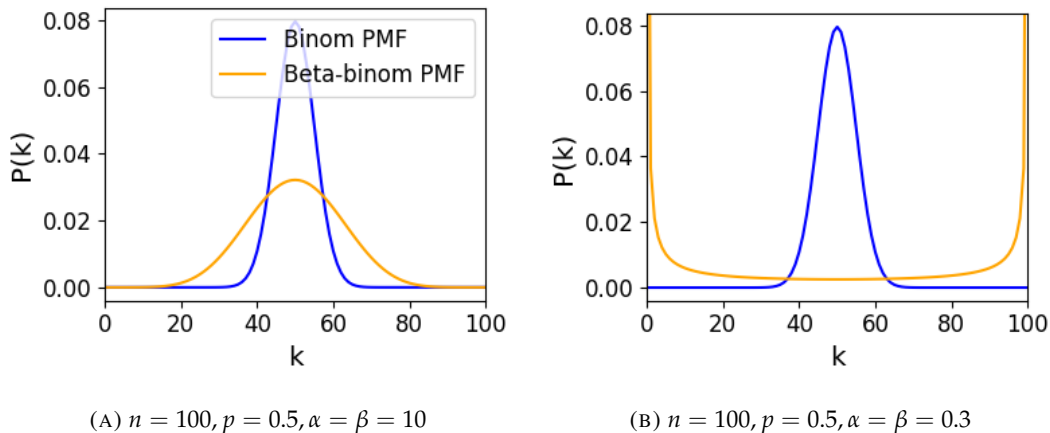


FIGURE 4.1: Figures showing the over-dispersion possible for a beta-binomial distribution relative to a binomial distribution. Parameters are shown in the captions.

### 1998 Conway-Maxwell-binomial distribution

1999 The Conway-Maxwell-binomial distribution (COMb distribution) is a three parameter generalisation of the binomial distribution that allows for over dispersion and under dispersion  
 2000

relative to the binomial distribution. The parameters of the distribution are  $n$  the number of Bernoulli trials, and two shape parameters  $0 \leq p \leq 1$ , and  $\nu \in \mathbb{R}$ .

The probability mass function of the COMb distribution is

$$P(k; n, p, \nu) = \frac{1}{S(n, p, \nu)} \binom{n}{k}^{\nu} p^k (1-p)^{n-k} \quad (4.6)$$

where

$$S(n, p, \nu) = \sum_{j=0}^n \binom{n}{j}^{\nu} p^j (1-p)^{n-j} \quad (4.7)$$

The only difference between this PMF and the PMF for the standard binomial is the introduction of  $\nu$  and the consequent introduction of the normalising function  $S(n, p, \nu)$ .

Indeed, if  $\nu = 1$  the COMb distribution is identical to the binomial distribution with the same values for  $n$  and  $p$ . We can see in figure 4.2d that the KL-divergence  $D_{KL}(P_{COMb}(n, p, \nu) || P_{Bin}(n, p)) = 0$  along the line where  $\nu = 1$ . The analytical expression for the divergence is

$$D_{KL}(P_{COMb}(k; n, p, \nu) || P_{Bin}(k; n, p)) = (\nu - 1) E_{P_{COMb}(k; n, p, \nu)} \left[ \log \binom{n}{k} \right] \quad (4.8)$$

$$- \log S(n, p, \nu) \quad (4.9)$$

At  $\nu = 1$ , we have  $S(n, p, 1)$  which is just the sum over the binomial PMF, so  $S(n, p, 1) = 1$  and therefore  $D_{KL}(P_{COMb}(n, p, \nu) || P_{Bin}(n, p)) = 0$ .

If  $\nu < 1$  the COMb distribution will exhibit over-dispersion relative to the binomial distribution. If  $p = 0.5$  and  $\nu = 0$  the COMb distribution is the discrete uniform distribution, and if  $\nu < 0$  the mass of the COMb distribution will tend to build up near  $k = 0$  and  $k = n$ . This over-dispersion represents positive association in the Bernoulli variables. An example of this over-dispersion can be seen in figure 4.2b.

If  $\nu > 1$  the COMb distribution will exhibit under-dispersion relative to the binomial distribution. The larger the value of  $\nu$  the more probability mass will build up at  $n/2$  for even  $n$ , or at  $\lfloor n/2 \rfloor$  and  $\lceil n/2 \rceil$  for odd  $n$ . This under-dispersion represents negative association in the Bernoulli variables. An example of this under-dispersion can be seen in figure 4.2a.

It should be noted that the  $p$  parameter of the COMb distribution does not correspond to the mean of the distribution, as is the case for the binomial  $p$  parameter, and beta-binomial  $\pi$  parameter. That is, the COMb  $p$  parameter is not a location parameter. An illustration of this can be seen in figure 4.2c. This is because an interaction between the  $p$  and  $\nu$  parameters skews the mean. There is no analytical expression for the mean of the COMb distribution.

$\nu$	Relative dispersion	Association between neurons/variables
< 1	over	positive
1	none	none
> 1	under	negative

TABLE 4.2: Relative dispersion of the COMb distribution, and association between Bernoulli variables as represented by the value of the  $\nu$  parameter.

2021 Since the COMb distribution has the potential to capture positive and negative associa-  
 2022 tions between the neurons/Bernoulli variables, it should be an excellent candidate for mod-  
 2023 elling the number of active neurons in a neuronal ensemble.

2024 We wrote a dedicated Python package to enable easy creation and fitting of COMb dis-  
 2025 tribution objects. The format of the package imitates the format of other distribution objects  
 2026 from the `scipy.stats` Python package. The COMb package can be found here:  
 2027 [https://github.com/thomasjdelaney/Conway\\_Maxwell\\_Binomial\\_Distribution](https://github.com/thomasjdelaney/Conway_Maxwell_Binomial_Distribution)

### 2028 4.3.6 Fitting

2029 We fitted binomial, beta-binomial, and Conway-Maxwell-binomial (COMb) distributions to  
 2030 the neural activity in each of the overlapping windows covering each trial. To fit the distribu-  
 2031 tions we minimised the appropriate negative log likelihood function using the data from the  
 2032 window.

There is an analytical solution for maximum likelihood estimate of the binomial distribution's  $p$  parameter.

$$\hat{p} = \frac{1}{n} \sum_{i=1}^N k_i \quad (4.10)$$

2033 We minimised the negative log likelihood function of the beta-binomial distribution nu-  
 2034 merically. We calculated the negative log likelihood for a sample directly, by taking the sum  
 2035 of the log of the probability mass function for each value in the sample. We minimised the  
 2036 negation of that function using the `minimise` function of the `scipy.optimize` Python  
 2037 package.

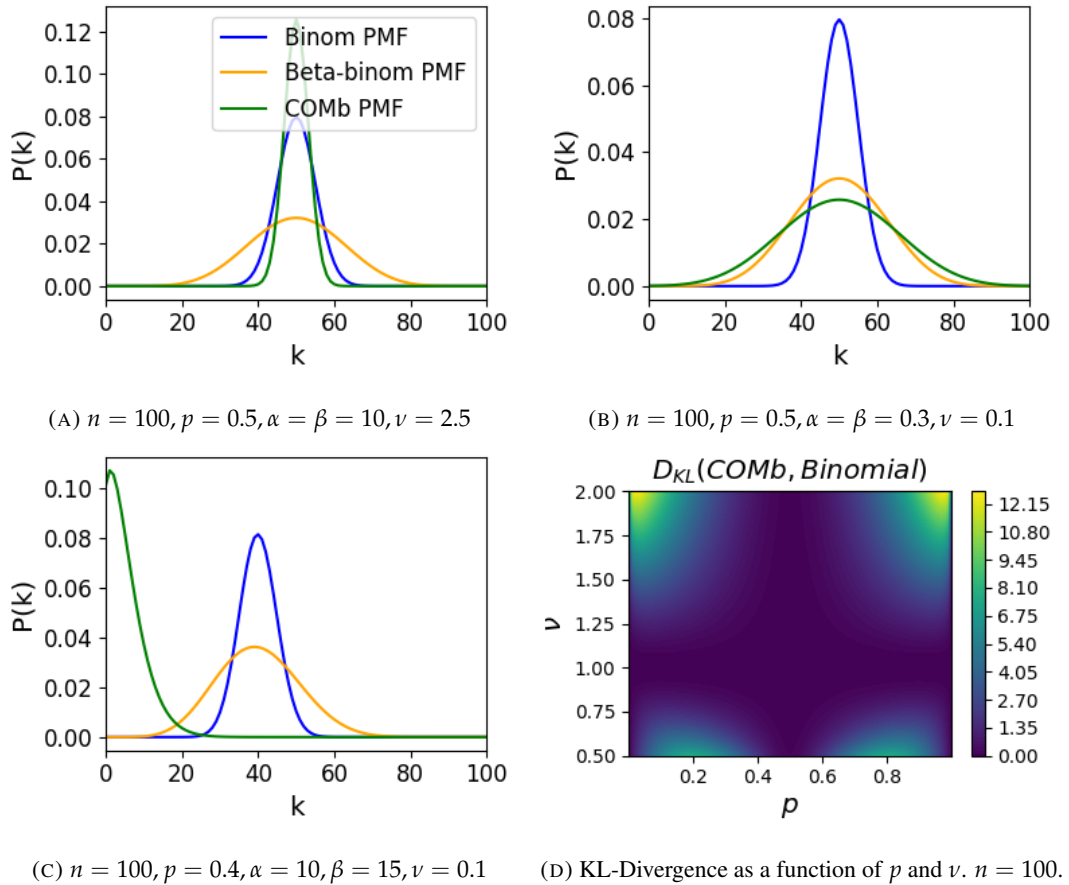


FIGURE 4.2: Figures showing (A) the under-dispersion and (B) over-dispersion permitted by the COMb distribution relative to a binomial distribution. (C) illustrates that the  $p$  parameter of the COMb distribution does not correspond to the mean of the distribution, as it does for the binomial and beta-binomial distributions. (D) shows a heatmap for the value of the Kullback-Liebler divergence between the COMb distribution and the standard binomial distribution with same value for  $n$ , as a function of  $p$  and  $\nu$ . Parameters are shown in the captions.

The log likelihood function of the COMb distribution given some sample  $\{k_1, \dots, k_N\}$  is

$$\ell(p, \nu | k_1, \dots, k_N) = N [n \log(1 - p) - \log S(n, p, \nu)] \quad (4.11)$$

$$+ \log \frac{p}{1 - p} \sum_{i=1}^N k_i \quad (4.12)$$

$$+ \nu \sum_{i=1}^N \log \binom{n}{k_i} \quad (4.13)$$

2038 We minimised the negation of this function using numerical methods. More specifically, we  
2039 used the `minimise` function of the `scipy.optimize` Python package.

2040 **4.3.7 Goodness-of-fit**

2041 After fitting, we measured the goodness-of-fit of each model/distribution with their log like-  
2042 lihood. We calculated this directly using the `logpmf` functions of the distribution objects in  
2043 Python.

2044 **4.4 Results**

2045 We defined a neuron as *active* in a time bin if it fires at least one spike during the time interval  
2046 covered by that bin. We measured the number of active neurons in the primary visual cortex  
2047 of a mouse in 1ms bins across 160 trials of a moving bar visual stimulus. We then slid a  
2048 100ms window across these 1ms bins taking measurements, and fitting distributions along  
2049 the way. We did the same for neurons in the thalamus, hippocampus, striatum, and motor  
2050 cortex. We repeated the analysis for 5ms time bins with 40 bin windows, and 10ms time bins  
2051 with 40 bin windows.

2052 **4.4.1 Increases in mean number of active neurons and variance in number of  
2053 active neurons at stimulus onset in some regions**

2054 We measured the average number of active neurons, and the variance of the number of active  
2055 neurons in a 100ms sliding window starting 500ms before stimulus onset until 1000ms after  
2056 stimulus onset. We found differences in the response across regions. There were no observed  
2057 changes in response to the stimulus in the motor cortex or the striatum. The changes in the  
2058 other regions are detailed below.

2059 **Primary visual cortex**

2060 We found a transient increase in both the average and variance of the number of active neu-  
2061 rons at stimulus onset, followed by a fall to pre-stimulus levels, followed by another transient  
2062 increase (see figure 4.3). The oscillation in both of these measurements appear to reflect the  
2063 frequency of the stimulus (see Data section 4.2.1), and it is known that stimulus structure can  
2064 influence response structure(Litwin-Kumar, Chacron, and Doiron, 2012). We see a similar  
2065 but lower amplitude oscillation at the end of the stimulus presentation.

2066 **Hippocampus**

2067 In the hippocampus we observed a transient increase in the average number of active neurons  
2068 and in the variance of the number of active neurons at stimulus onset (see figure 4.4). The  
2069 increase lasted about 125ms, and the subsequent fall to baseline took the a similar amount of  
2070 time.

2071 **Thalamus**

2072 In the thalamus we observed a transient increase in the both the average and variance of  
2073 the number of active neurons on stimulus onset, followed by a fall to pre-stimulus levels,  
2074 followed by a sustained increase until the stimulus presentation ends.

2075 As one you might expect for a visual stimulus, the change in the average number of active  
2076 neurons was greatest in the primary visual cortex. In this region, this quantity doubled on  
2077 stimulus onset. In contrast, in the hippocampus and the thalamus, the average number of  
2078 active neurons only increased by a fraction of the unstimulated baseline value. The duration  
2079 of the response in V1 and the hippocampus at stimulus onset was 300 – 400ms, but the  
2080 response in the thalamus appeared to last for the duration of stimulus presentation. The V1  
2081 also showed a change in the average number of active neurons at stimulus end. The change  
2082 was similar to that observed at stimulus onset, but smaller in magnitude (see figures 4.3, 4.4,  
2083 and 4.5)

2084 **4.4.2 Conway-Maxwell-binomial distribution is usually a better fit than bino-  
2085 mial or beta-binomial**

2086 Since the Conway-Maxwell-binomial distribution has not been fitted to neuronal data before,  
2087 it is not clear that it would be a better fit than the binomial or beta-binomial distributions.  
2088 In order to find out which parametric distribution was the best fit for the largest proportion

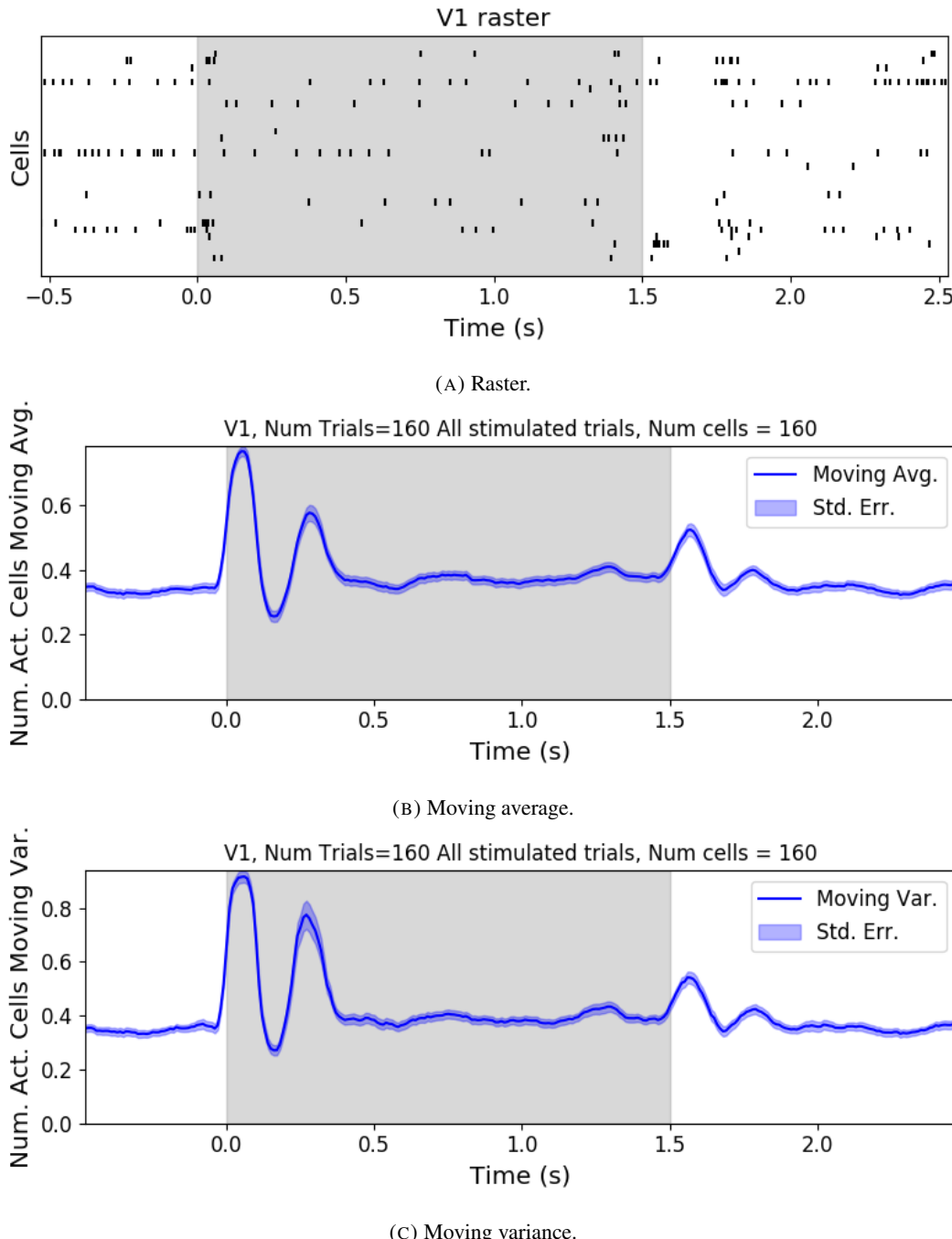


FIGURE 4.3: (A) Raster plot showing the spikes fired by 33 randomly chosen neurons in the primary visual cortex. (B-C) (B) average and (C) variance of the number of active neurons, measured using a sliding window 100ms wide, split into 100 bins. The midpoint of the time interval for each window is used as the timepoint (x-axis point) for the measurements using that window. The grey shaded area indicates the presence of a visual stimulus. The opaque line is an average across the 160 trials that included a visual stimulus of any kind. We can see a transient increase in the average number of active neurons and the variance of this number, followed by a fluctuation and another increase.

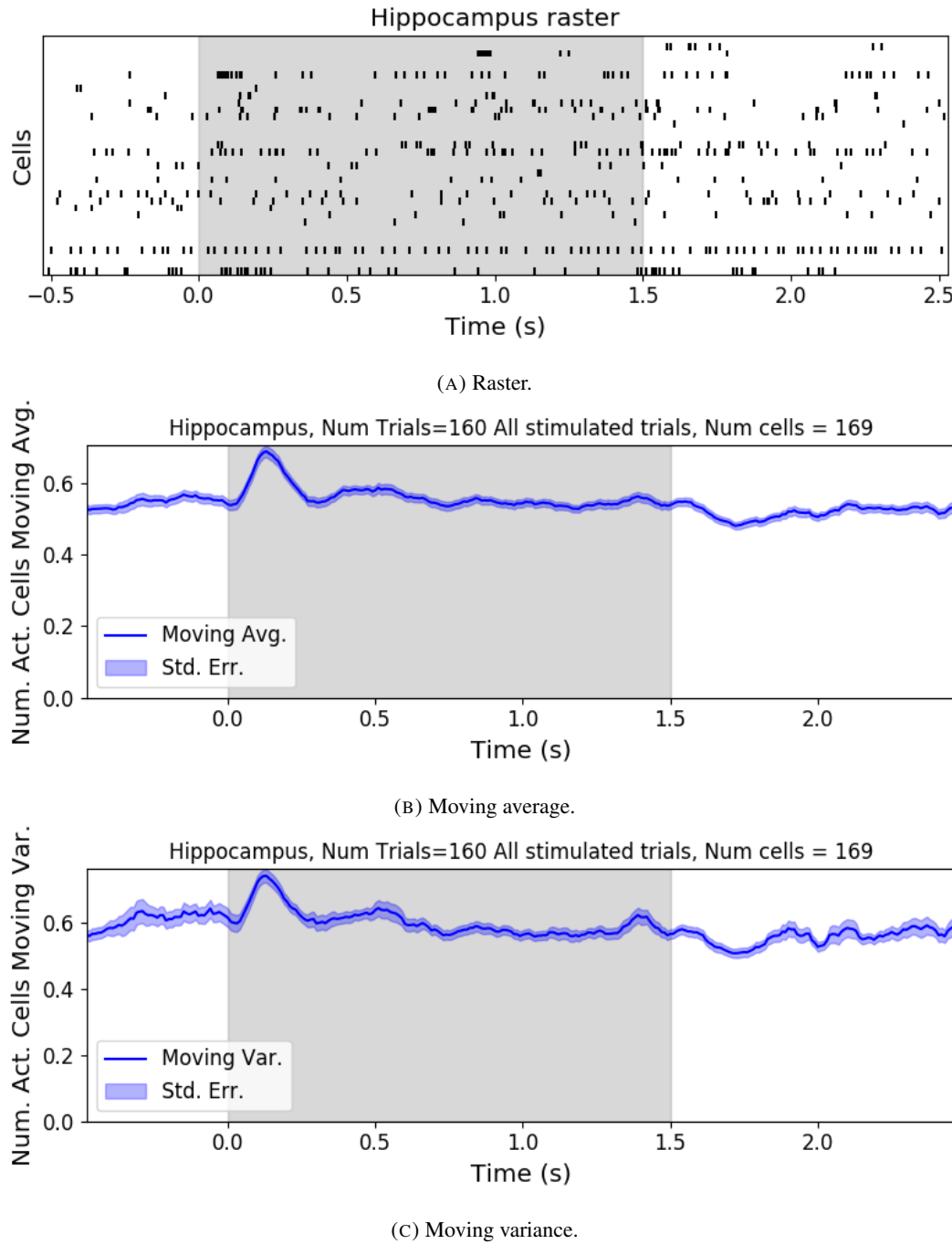


FIGURE 4.4: (A) Raster plot showing the spikes fired by 33 randomly chosen neurons in the hippocampus. (B-C) (B) average and (C) variance of the number of active neurons, measured using a sliding window 100ms wide, split into 100 bins. The midpoint of the time interval for each window is used as the timepoint (x-axis point) for the measurements using that window. The grey shaded area indicates the presence of a visual stimulus. The opaque line is an average across the 160 trials that included a visual stimulus of any kind. We can see a transient increase in the average number of active neurons and the variance of this number at stimulus onset.

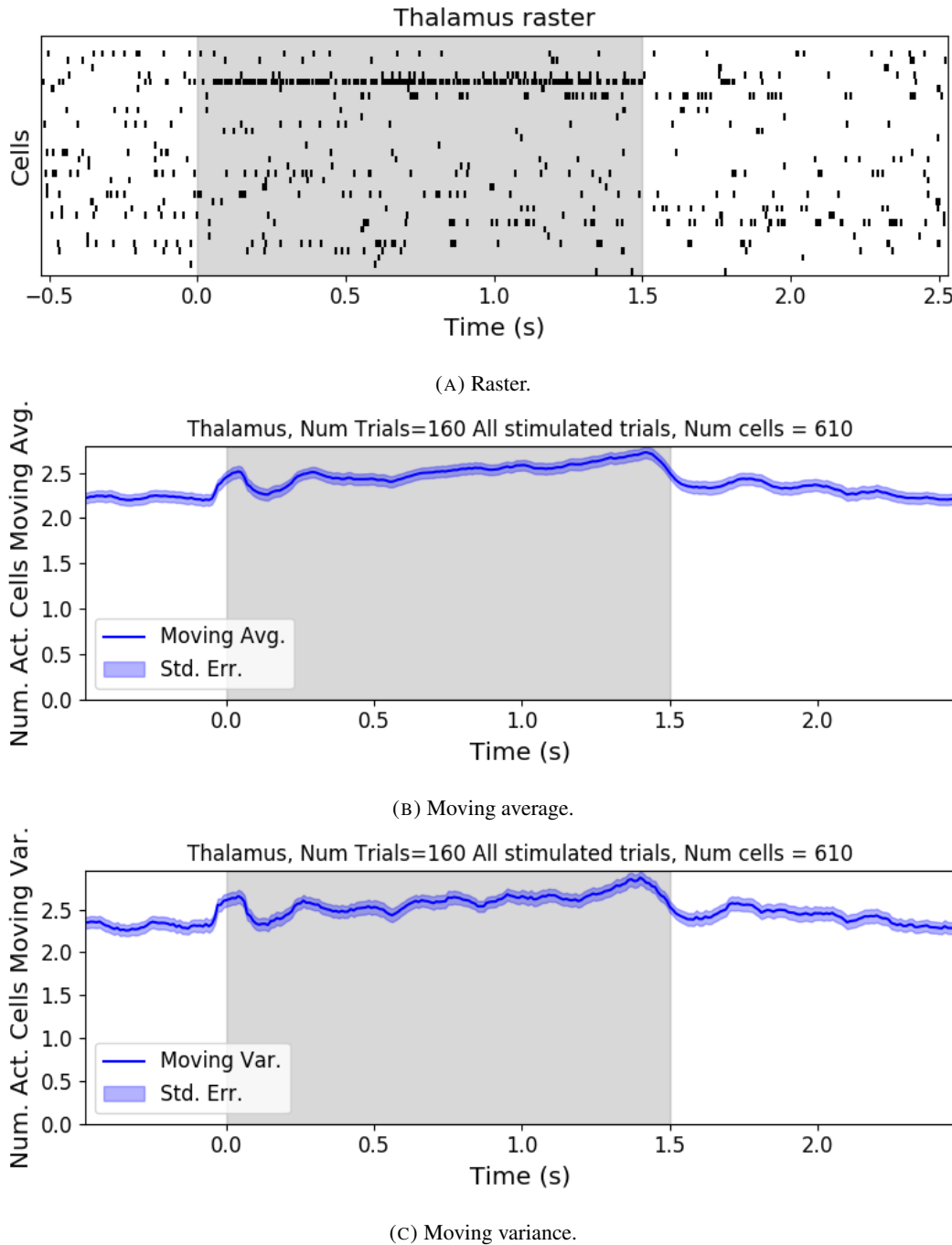
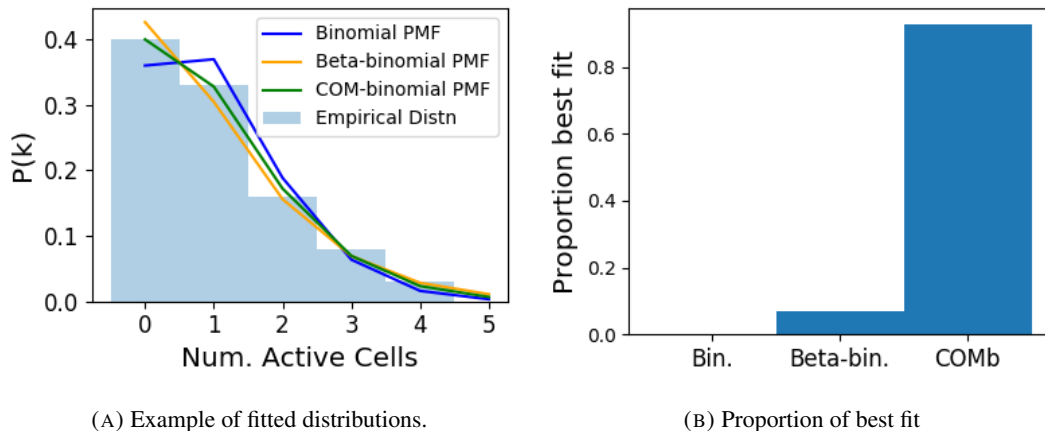


FIGURE 4.5: (A) Raster plot showing the spikes fired by 33 randomly chosen neurons in the thalamus. (B-C) (B) average and (C) variance of the number of active neurons, measured using a sliding window 100ms wide, split into 100 bins. The midpoint of the time interval for each window is used as the timepoint (x-axis point) for the measurements using that window. The grey shaded area indicates the presence of a visual stimulus. The opaque line is an average across the 160 trials that included a visual stimulus of any kind. We can see an immediate increase at stimulus onset, a subsequent fall, and another sustained increase until the stimulus presentation ends.

of our data, we fit a binomial, a beta-binomial, and a Conway-Maxwell-binomial (COMb) distribution to each window for each bin width, and each region. Then we assessed the goodness-of-fit of each distribution by calculating the log-likelihood of each fitted distribution using the associated sample. We measured the proportion of samples for which each distribution was the best fit, for each bin width value and each region.

We found that the COMb distribution was the best fit for most of the samples regardless of bin width or region. The bin width had an effect on the number of samples for which the COMb distribution was the best fit. The results are summarised in table 4.3. For a bin width of 1ms, the COMb distribution was the best fit for over 90% of samples, the beta-binomial distribution was the best fit for less than 10% of samples, and the binomial distribution was the best fit for less than 1% of samples, across regions. For 5ms bins, the COMb distribution was the best fit for 70 – 80% of samples, the beta-binomial distribution was the best fit for 20 – 30% of the samples, and again the binomial distribution was the best fit for less than 1% of samples, across regions. Finally, for 10ms bins, the COMb distribution was the best fit for 53 – 80% of samples, the beta-binomial distribution was the best fit for 20 – 47% of the samples, and the binomial distribution was the best fit for less than 0.1% of samples, across regions.



(A) Example of fitted distributions.

(B) Proportion of best fit

FIGURE 4.6: (A) An example of the binomial, beta-binomial, and Conway-Maxwell-binomial distributions fitted to a sample of neural activity. The Conway-Maxwell-binomial distribution is the best fit in this case. The histogram shows the empirical distribution of the sample. The probability mass function of each distribution is indicated by a different coloured line. (B) Across all samples in all trials, the proportion of samples for which each fitted distribution was the best fit. The Conway-Maxwell-binomial distribution was the best fit for 93% of the samples taken from V1 using a bin width of 1ms.

Bin Width (ms)	Binomial	Beta-binomial	COMb
1ms	< 1%	< 10%	> 90%
5ms	< 0.1%	20 – 30%	70 – 80%
10ms	< 0.1%	20 – 47%	53 – 80%

TABLE 4.3: Proportion of samples for which each distribution was the best fit, grouped by bin width. The COMb distribution is the best fit most of the time.

2106 **4.4.3 Conway-Maxwell-binomial distribution captures changes in association  
2107 at stimulus onset**

2108 We fit a Conway-Maxwell-binomial (COMb) distribution to the number of active neurons in  
2109 the 1ms time bins in a 100ms sliding window. We also measured the correlation coefficient  
2110 between the spike counts of all possible pairs of neurons, and took the average of these  
2111 coefficients. We did this for all the trials with a visual stimulus. We observed a reduction in  
2112 the COMb distribution's  $\nu$  parameter at stimulus onset from around 1 to between 0 and 1 (see  
2113 figure 4.7a). A value of  $\nu$  less than 1 indicates positive association between the neurons (see  
2114 section 4.3.5). We might expect to see this positive association reflected in the correlation  
2115 coefficients, but this is not the case. We see no change in the time series of average correlation  
2116 measures at stimulus onset.

2117 This may be due to the very short time bin we used in this case. We know that using small  
2118 time bins can artificially reduce correlation measurements (Cohen and Kohn, 2011). In this  
2119 case, fitting the COMb distribution may be a useful way to measure association in a neuronal  
2120 ensemble over very short timescales (< 10ms).

2121 **4.4.4 Replicating stimulus related quenching of neural variability**

2122 Churchland et al. (2010) inspected the effect of a stimulus on neural variability. One of the  
2123 measures of neural variability that they employed was the Fano factor of the spike counts of  
2124 individual cells (see section 4.3.4). They found a reduction in neural variability as measured  
2125 by the Fano factor in various cortical areas in a macaque at the onset of various visual stimuli,  
2126 or a juice reward (Churchland et al., 2010).

2127 We measured the Fano factor of the spike count of each cell in each brain region, during  
2128 each trial. We measured the mean and standard error of these Fano factors from 500ms  
2129 before stimulus onset until 1000ms after stimulus end. For the primary visual cortex, we  
2130 found a transient reduction in the Fano factor immediately after stimulus onset. We used  
2131 a Mann-Whitney U test to check that the Fano factors measured in a window starting at

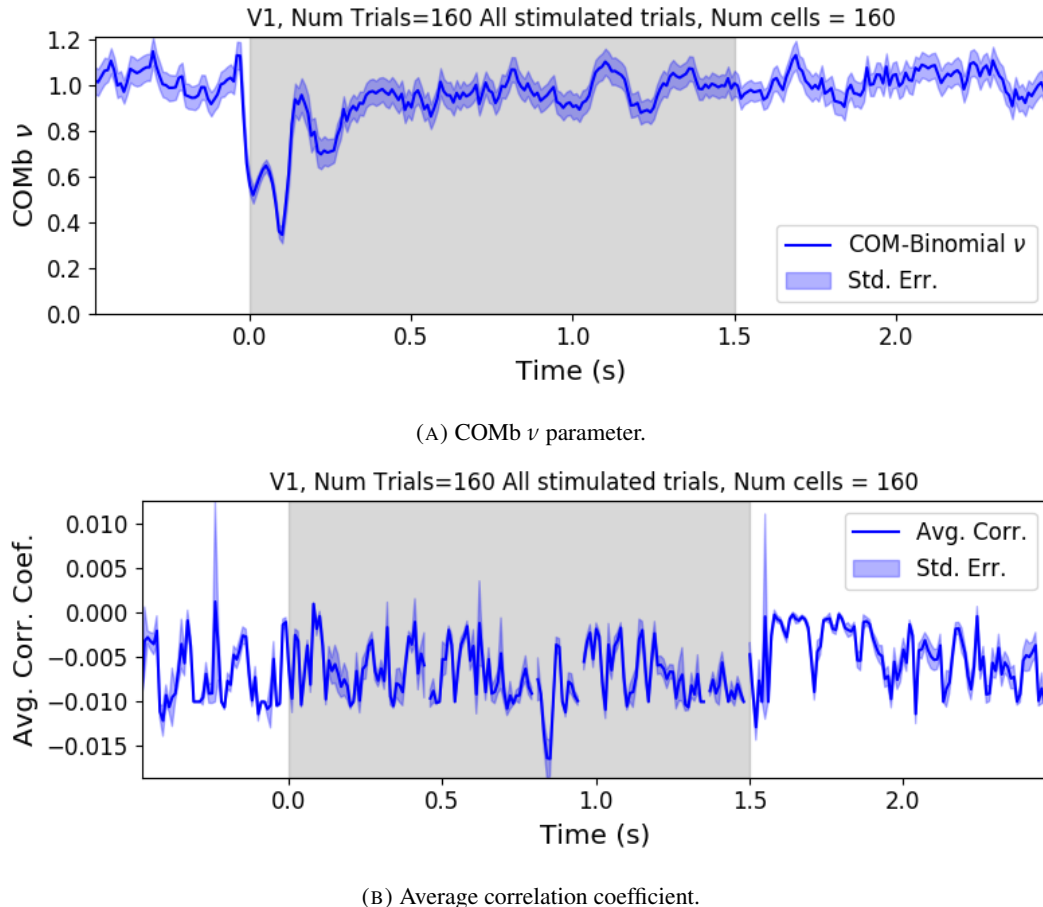


FIGURE 4.7: (A) We fit a Conway-Maxwell-binomial distribution to the number of active neurons in 1ms time bins of a 100ms sliding window. We did this for all trials with a visual stimulus and took the average across those trials. We see a transient drop in value for the distribution's  $\nu$  parameter at stimulus onset. This shows an increase in association between the neurons. (B) We measured the correlation coefficient between the spike counts of all possible pairs of neurons in the same sliding window. We took the average of those coefficients. We also did this for every visually stimulated trial, and took the average across trials. The increase in association is not reflected with an increase in average correlation.

stimulus onset and ending 100ms later were significantly lower than the factors measured in a window ending at stimulus onset ( $p < 0.001$ , see figure 4.8a). We did not get this statistically significant result in any other region.

Our findings agree with those of Churchland et al. for the primary visual cortex. However Churchland also found a reduction in the Fano factor in the dorsal premotor cortex (PMd) at stimulus onset. Our measurements from the mouse motor cortex show no change at stimulus onset (see figure 4.8b). This could indicate some difference in the functionality of the motor cortex in a macaque and the motor cortex of a mouse.

Similar to these findings in the Fano factor, we found a reduction in the  $\nu$  parameter of the COMB distribution on stimulus onset in V1 (figure 4.7a) and in no other region from

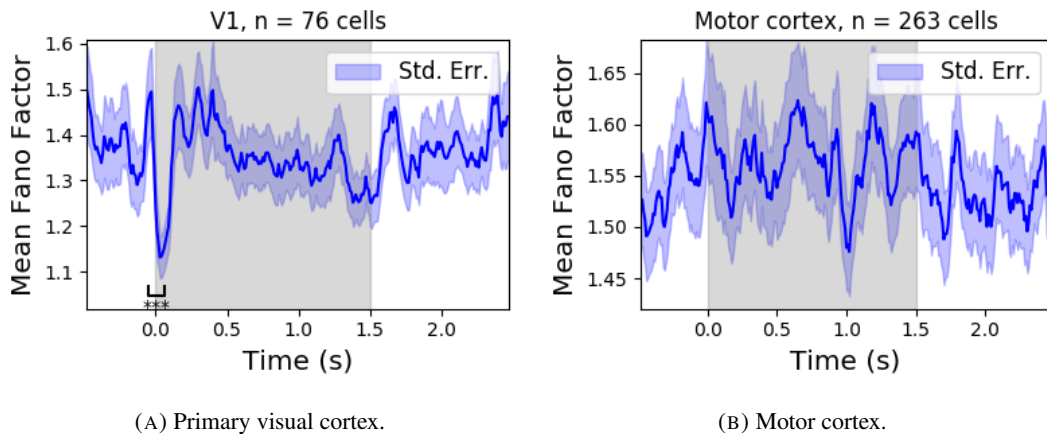


FIGURE 4.8: (A) The mean Fano factor of the spike counts of the cells in the primary visual cortex. Means were taken across cells first, then across trials. There was a significant decrease in the Fano factors immediately after stimulus onset. (B) The mean Fano factor of the spike counts of the cells in the motor cortex. No significant change in measurements at any point.

which we had data. Specifically, the  $\nu$  parameter reduced from around 1, to between 1 and 0. This represents a change from no association between the neurons, to a positive association. It is possible that this positive association may be responsible for the reduction in the Fano factor.

## 4.5 Discussion

Our aim in this research was to develop a new statistical method for analysing the activity of a neuronal ensemble at very short timescales. We wanted our method to use information taken from the whole ensemble, but we also wanted the method to be quick and easy to implement. It is likely that analysis methods with these characteristics will become valuable as electrophysiological datasets include readings from more cells over longer time periods. In this case, we used the number of active, or spiking, neurons in a very short time bin ( $< 10\text{ms}$ ) as a measure of ensemble activity.

First of all, we showed that there were changes in response that we could model at these very short time scales in some of the brain regions from which we had recordings. We observed changes in the average number of active neurons, and the variance of the number of active neurons in three different brain regions in response to visual stimuli. Since we know that correlated behaviour is associated with sensory perception (deCharms and Merzenich, 1996), we might hope to measure the pairwise correlations within the neuronal population in order to further investigate these responses. But, using such short time bins can produce

artificially small spike count correlation measurements (Cohen and Maunsell, 2009). Overcoming this limitation was one of our objectives for our new method. In order to do this, we abandoned the idea of measuring the correlations directly and embraced the concept of *association*. In order to quantify the association between neurons, we used the Conway-Maxwell-binomial distribution to model the number of active (spiking) neurons in an ensemble as a sum of possibly associated Bernoulli random variables.

We showed that the Conway-Maxwell-binomial distribution performed better than the more common options of the binomial and beta-binomial distributions. Furthermore, we showed that the positively associated behaviour between neurons in the primary visual cortex could be captured by fitting a Conway-Maxwell-binomial distribution, but was not captured by the more standard approach of measuring the spike count correlation. The associated behaviour could not be measured using spike count correlations, because of the very short bins required to capture short timescale behaviour.

We replicated a famous result from Churchland et al (2010) relating to the quenching of neural variability in cortical areas at stimulus onset, and in doing so, we established a correspondence between the association quantifying parameter of the Conway-Maxwell-binomial (COMb) distribution and the neural variability as measured by the Fano factor. We found a reduction in the  $\nu$  parameter of the COMB distribution at stimulus onset, indicating a change from no association to positive association between neurons in V1. We found a corresponding reduction in the Fano factor of the individual cells in V1. The positive association between neurons induced by the stimulus would constrain the neurons to fire at the same time. The stimulus also induced a larger number of neurons to spike. These two actions combined could cause an increase in the firing rate of individual cells that is greater in magnitude than the increase in firing rate variability. If this is indeed the case, then the association as captured by the COMB distribution could be regarded as one of the ‘natural parameters’ of the ensemble response for short timescales. That is, a quantity that directly measures some aspect of the behaviour of the ensemble. In this case, it the correlated behaviour of the individual neurons is captured.

This work could be just a first step in creating analysis methods based on the Conway-Maxwell-binomial distribution, or similar statistical models. One way to extend the method would be to pair it up with the ‘Population Tracking model’ (O’Donnell et al., 2017). This model attempts to characterise the interaction between an ensemble and each member of the ensemble by quantifying the probability of spiking for a given a cell, given the number of active cells in the whole population. Combining this model with the COMB distribution

2195 would give us a model that could accurately fit the number of active neurons at any moment,  
2196 and that gives a probability of firing for each cell, and therefore probabilities for full spiking  
2197 patterns, without adding a huge number of parameters to fit.

2198 A more complex way to extend the model would be to fit a Conway-Maxwell-binomial  
2199 distribution to data recorded from multiple brain regions simultaneously, with a different fit  
2200 for each region, then to analyse the temporal relationship between the fitted parameters of  
2201 each region. If we analysed the time series of the COMB distribution parameters from the  
2202 different regions, looking at cross-correlations between regions, this may give some results  
2203 relating to the timescales in which information is processed in different brain regions.

2204 **Chapter 5**

2205 **Studies with practical limitations &**  
2206 **negative results**

2207 *Abstract*

2208 Here I will present some details on research topics that I started, but that unfortunately did not  
2209 lead anywhere useful. There are two pieces of research, based on two papers. Each paper is  
2210 related to the overall theme of my PhD of analysing and modelling behaviours of populations  
2211 of neurons. The first part is based on a model of parallel spike trains including higher order  
2212 interactions by Shimazaki et al (2012). The second part is based on a multiscale model for  
2213 making inferences on hierarchical data.

2214 **5.1 Dynamic state space model of pairwise and higher order neu-**  
2215 **ronal correlations**

2216 In their paper Shimazaki et al (2012) aimed to model spike trains from populations of neurons  
2217 in parallel, with pairwise and higher order dynamic interactions between the trains. They  
2218 modelled the spike trains as multi-variate binary processes using a log-linear model, and they  
2219 extracted spike interaction parameters using a Bayesian filter/EM-algorithm. They developed  
2220 a goodness-of-fit measure for the model to test if including these higher order correlations  
2221 is necessary for an accurate model. Their measure was based on the Bayes factor but they  
2222 also assessed the suitability of higher order models using the AIC and BIC. So the increase  
2223 in the number of parameters associated with fitting higher order interactions was taken into  
2224 account. They tested the performance of the model on synthetic data with known higher  
2225 order correlations. They used the model to look for higher order correlations in data from  
2226 awake behaving animals. They use the model to demonstrate dynamic appearance of higher  
2227 order correlations in the monkey motor cortex (Shimazaki et al., 2012).

2228 We used the available Python repository to implement the model, and we successfully  
2229 worked through the tutorial provided. But we found that the model did not scale well to  
2230 larger populations. We attempted to fit the model to a population of 10 neurons and found we  
2231 didn't manage to finish the process. Since, our goal was to find a model to scale to hundreds  
2232 or thousands of neurons, we decided that this model was no longer worth pursuing.

2233 **5.2 A multiscale model for hierarchical data applied to**  
2234 **neuronal data**

2235 In their paper Kolaczyk et al (2001) developed a framework for a modelling hierarchically  
2236 aggregated data, and making inferences based on a model arising from this framework. They  
2237 assumed that a hierarchical aggregation existed on the data in question, where each element at  
2238 each level of the hierarchy had some associated measurements, an associated mean process,  
2239 which was the expected value of these measurements. They also assumed that the measure-  
2240 ments of each parent were equal to the sum of the measurements from all of its children.  
2241 They showed that these assumptions gave rise to a relationship between parent and child  
2242 measurements across all levels of the hierarchy, where the product of the likelihood of the  
2243 parameters of the lowest level of the hierarchy can be expressed as products of conditional  
2244 likelihoods of the elements of higher levels of the hierarchy (Kolaczyk and Huang, 2010).

2245 They gave examples of these expressions for measurements sampled from Gaussian dis-  
2246 tributions, and Poisson distributions, and showed the definitions of the hierarchical param-  
2247 eters which reparametrise the distribution of these data taking the hierarchy into account.  
2248 They go on to suggest prior distributions for this multiscale model, and integrate these priors  
2249 to give posterior distributions for the measurements from each element at each level in the hi-  
2250 erarchy, and expressions for the MAP estimated parameters of each the associated processes  
2251 (Kolaczyk and Huang, 2010).

2252 We implemented their model in Python by creating some synthetic data from Poisson  
2253 distributions, and defining a hierarchy by agglomerating these data. We calculated the MAP  
2254 estimates using our knowledge of the hierarchy, and using the expressions given in the paper.  
2255 We found that the MAP estimates were far less accurate than would be achieved by simply  
2256 ignoring the hierarchy during estimation, and using a maximum likelihood approach. After  
2257 that, we decided to move on.



2258 **Chapter 6**

2259 **Discussion**

2260 In this project, we attempted to address some of the challenges in data collection from  
 2261 large neuronal ensembles (specifically with calcium imaging) and some of the problems in  
 2262 analysing the data collected from large neuronal ensembles.

2263 Firstly, we investigated the relationship between cell biochemistry, action potentials and  
 2264 the fluorescence traces produced by fluorescent calcium indicators. We did this by building  
 2265 a biophysical model that takes in a spike train and returns the fluorescence trace that that  
 2266 spike would induce. The model included mechanics for the binding of calcium to fluorescent  
 2267 and endogenous mobile and immobile buffers, and the consequent changes in concentration  
 2268 of free and bounded calcium. The model consisted of 17 parameters, 13 of which were  
 2269 set according to data from the literature, and 4 of which were free parameters. We trained  
 2270 the model using simultaneously collected spiking and calcium imaging data (Berens et al.,  
 2271 2018). We fitted the model by matching the  $\Delta F/F_0$  in response to an action potential, and  
 2272 by matching the power spectrum of the actual fluorescence trace. This meant that our model  
 2273 would include the correct amount of noise as well as return the correct change in amplitude  
 2274 in response to an action potential.

2275 Since our model produced fluorescence traces, we could apply spike inference algorithms  
 2276 to the modelled fluorescence traces that our model produced after training, and compare the  
 2277 performance of the algorithms on the modelled traces to their performance on the real traces.  
 2278 We used three spike inference algorithms, two of which were based on modelling the cal-  
 2279 cium trace as an autoregression (Friedrich and Paninski, 2016; Pnevmatikakis et al., 2016),  
 2280 and another inference algorithm that was a little more biologically inspired, but amounted to  
 2281 a very similar algorithm (Deneux et al., 2016). We compared the performance of the algo-  
 2282 rithms by using them to infer spikes from 20 real and modelled fluorescence traces induced  
 2283 by 20 corresponding real spike trains. We then used several binary classification measures  
 2284 (true positive rate, accuracy etc.) to asses the quality of the spike inference for the real and

2285 modelled fluorescence traces. We found that the spike inference algorithms performed sim-  
2286 ilarly on real and modelled traces, showing that our model is capturing at least some of the  
2287 characteristics of the real fluorescence traces.

2288 In order to investigate the effect of indicator characteristics on the modelled fluorescence  
2289 trace and spike inference quality, we perturbed the indicator's affinity and dissociation rate in  
2290 parallel, keeping the ratio of the two the same for all perturbations. We measured the SNR  
2291 of the trace, and the true positive rate of the spike inference algorithms at each perturbed  
2292 value pair. We found that perturbing the values lower caused in decrease in SNR and spike  
2293 inference quality. This shows that our model could be used to test theoretical fluorescent cal-  
2294 cium indicators without having to actually manufacture them. Experimental neuroscientists  
2295 could also use our model to judge which indicator characteristics are most influential in their  
2296 experimental context.

2297 We then investigated the effect of perturbing buffer concentration, and indicator concen-  
2298 tration, on the signal-to-noise ratio of the modelled fluorescence trace and spike inference  
2299 quality. This was a worthwhile experiment because endogenous buffer concentrations vary  
2300 from cell to cell (Bartol et al., 2015; Maravall et al., 2000; Neher and Augustine, 1992), as  
2301 does indicator expression (Chen et al., 2013). We found that extreme perturbations away  
2302 from the indicator concentration taken from the literature lowered the SNR of the trace, and  
2303 the spike inference quality. We also found that increases in the concentration of endogenous  
2304 buffer above the value taken from the literature caused a decrease in the SNR and spike infer-  
2305 ence quality. This reiterates that the indicator and endogenous buffers compete to bind with  
2306 free calcium molecules, and this has an effect on fluorescence and consequently on spike  
2307 inference.

2308 We then created some synthetic spike trains with controlled mean firing rates sampled  
2309 the rates from an Ornstein-Uhlenbeck process. We found that the higher the firing rate, the  
2310 lower the accuracy of the spike inference algorithms. But the mean firing could perhaps be  
2311 inferred from the amplitude of the fluorescence traces. The higher firing rate, the higher the  
2312 amplitude. Calibrating the model to facilitate and accurate measurement would require some  
2313 kind of ground truth, but relative comparisons could be made without any other knowledge  
2314 of the underlying spiking process.

2315 One obvious limitation to our model is the lack of binding mechanics for both the indi-  
2316 cator and endogenous buffers. Greenberg et al included these mechanics in their successful  
2317 spike inference model. We felt that the timescale of these binding mechanics was so small  
2318 in comparison to the fluorescence dynamics that omitting them would make no difference.

2319 But it is possible that their inclusion would improve our model.

2320 After investigating the difficulties with inferring spiking data from calcium imaging data,  
2321 we moved from data collection to analysis and we decided to implement a new network anal-  
2322 ysis method on data from a neuronal ensemble. Using an electrophysiological dataset with  
2323 spike sorted data from 9 different brain regions in 3 mice (Steinmetz, Carandini, and Harris,  
2324 2019), we binned the spike times for each cell into spike counts for each cell and measured  
2325 the correlation coefficients between these spike counts for a selection of cells evenly dis-  
2326 tributed across the 9 regions. We repeated these measurements for time bin widths ranging  
2327 from 5ms to 3s. We rectified these measurements and, for a given time bin width, used them  
2328 as weights for a weighted undirected graph where each node represents a neuron, and the  
2329 weight of each edge is the correlation between the neurons represented by the nodes on that  
2330 edge. We applied a novel spectral analysis and community detection method (Humphries  
2331 et al., 2019) to this network. This clustered the nodes in our ensemble into communities  
2332 whose behaviour was more correlated than expected. Our measure of 'expected correlation  
2333 strength' were based on a random network that matched our data network's sparsity and total  
2334 weight. We compared the detected communities to the anatomical division of our cells using  
2335 clustering comparison measures. We then conditioned the binned spike counts on the be-  
2336 haviour of the mouse using the principal components of a video of the mouses face recorded  
2337 simultaneously with the electrophysiology. We broke the total covariance down into 'spike  
2338 count covariance' and 'signal covariance' components conditioning on the behavioral data  
2339 and using the law of total covariance. We then repeated our analysis for spike count corre-  
2340 lations, and signal correlation. Finally, since our community detection method was only valid  
2341 on graphs with non-negative weights, we used different methods for creating a non-negative  
2342 graph from our total correlations, and we repeated our analysis on those graphs.

2343 Our first finding was that the time bin width used to bin spike times into spike counts had  
2344 a effect on the mean magnitude of the correlations measured. The wider the bin, the higher  
2345 the correlations. Not only that, we separated the pairs into positively and negative correlated  
2346 pairs, and we found that positively correlated pairs have greater correlation coefficients when  
2347 using a wider bin, and negatively correlated pairs have more negative correlation coefficients  
2348 when using a wider bin. We also found that the width of the bin used had an effect on the  
2349 distribution of the spike counts. For smaller bin widths, the distribution of spike counts was  
2350 better represented by a skewed distribution like the Poisson distribution. For wider bins, the  
2351 spike counts were better represented by a Gaussian distribution.

2352 Next we investigated the differences between correlations within regions and between

2353 regions. When we divided the pairs according to those two groups, we found that the mean  
2354 within-region correlations were higher at every bin width, and the difference between the two  
2355 means grew with increasing bin width. When we split the pairs of cells according to their  
2356 regions, we found that the mean within-region correlations in any given region were usually  
2357 greater than the mean between-region correlations for any region pair involving that region.  
2358 The difference between the mean within-region correlation and the highest between-region  
2359 correlations involving that region grew smaller with increasing bin width. To investigate this  
2360 further, we plotted these mean correlations in matrices. Although the mean within-region  
2361 correlations were usually the highest value in their row or column, as the bin width increased,  
2362 the mean between-region correlations grew in magnitude relative to the within-region figure.

2363 Next we chose a null network model, and we used the ‘Network Noise Rejection’ pro-  
2364 cess (Humphries et al., 2019) to check for additional structure in our correlation based data  
2365 network that was not captured by the null model. We found additional structure for any bin  
2366 width that we used. We also found that the dimensionality of the additional structure reduced  
2367 as we increased the bin width. This could mean that the processes or representations that take  
2368 place over longer timescales within the brain also take place in a lower dimensional space.

2369 We applied a community detection method (Humphries, 2011) to the signal correlation  
2370 networks arising from the network noise rejection. We found that the number of communi-  
2371 ties detected decreased with increasing bin width. We also noticed that at shorter bin widths,  
2372 the detected communities were more likely to consist of cells from one brain region only.  
2373 We investigated this further by using clustering comparison methods to compare the detected  
2374 communities with the anatomical division of the cells. We found that for short timescales  
2375 < 50ms correlated communities tended to exist within anatomical regions, and for longer  
2376 timescales > 100ms, the correlated communities tended to exist across anatomical regions.  
2377 This is broadly in agreement with a similar finding for EEG data from humans performing se-  
2378 mantic or memory tasks (Stein and Sarnthein, 2000). Von Stein et al. (2000) found that visual  
2379 processing taking place locally in the visual system was captured in the gamma frequency  
2380 range (25 – 70Hz), while semantic processing was captured in the beta range (12 – 18Hz),  
2381 and tasks involving mental imagery and working memory retention were captured in the theta  
2382 and alpha ranges (4 – 8Hz, and 8 – 12Hz respectively).

2383 We then conditioned our correlation measures on the the mouse’s behaviour. This al-  
2384 lowed us to create spike count correlation (or noise correlation) networks, and signal corre-  
2385 lation networks (Cohen and Kohn, 2011). We applied our analysis to these networks. For the

spike count correlation networks we found very similar results to the total correlation networks. More communities at smaller bin widths, and communities resembled the anatomical division at smaller bin widths. Given that recent findings show that behaviour can account for correlated spiking in many areas of the brain (Stringer et al., 2019), these results for the spike count correlation show that this correlated behaviour is still processed locally at short timescales, while processes and representations that take more time make use of correlated activity across multiple regions.

For the signal correlations, we still found additional structure in these networks. But we always detected a smaller number of communities. These communities also had no relation to the anatomical division of the cells. This result shows that there are groups of cells across multiple brain regions that are activated similarly by certain behaviours.

All of the networks so far were based on rectified correlation measures, because the network noise rejection and community detection processing is (currently) only valid for networks with non-negative weights. For the final part of our analysis, we tried different ways of transforming our total correlations into non-negative quantities before applying our analysis. First of all we took the absolute value of our correlation measures. Our results were very similar to those for the rectified correlations with the exception that we detected more communities consistently. It is possible that using this method detects both positively and negatively correlated communities.

We also tried reversing the sign of all the correlations, then rectifying the network. We hope that this would allow us to detect the negatively correlated communities. We did detect communities in these networks, but never more than three, and these communities bore no relationship with the anatomical distribution of the cells.

Having spent much time investigating correlated behaviour using coefficients of spike counts, we decided to try another method for capturing correlated behaviour in neuronal ensembles. We used electrophysiological data taken from 5 brain regions of an awake mouse exposed to visual stimuli (Steinmetz et al., 2019). We modelled the number of active neurons in a given brain region as the number of successes in a collection of dependent Bernoulli random variables using the Conway-Maxwell-binomial distribution. To avoid violating the Bernoulli assumption, we binned the spike times using 1ms bins. The Conway-Maxwell-binomial distribution is a two parameter extension of the standard binomial distribution. The extra parameter allows the distribution to capture possible positive or negative association between the Bernoulli trials (Kadane, 2016). This means that we are assuming that all the neurons are dependent in the same way. This is not an accurate assumption, but it allows us

2420 model the data in a simple way.

2421 First of all we established that there were changes in the number of active neurons in  
2422 response to the visual stimuli. This was the case in the hippocampus, thalamus, and primary  
2423 visual cortex. Each region had its own signature response. We measured the mean and  
2424 variance of the number of active neurons in a sliding window starting before stimulus onset,  
2425 and finishing after the end of stimulus presentation.

2426 As well as the Conway-Maxwell-binomial distribution, we also fitted binomial, and beta-  
2427 binomial distributions to the number of active neurons in a sliding window. We found that the  
2428 Conway-Maxwell-binomial distribution was the best fit for over 90% of the samples. This  
2429 means that the COMb distribution is capturing some dependency between the neurons, be-  
2430 cause the binomial distribution assumes independence. Also the COMb distribution captures  
2431 this dependence more accurately than the beta-binomial distribution, which does have some  
2432 capacity for over dispersion.

2433 Next we showed that the Conway-Maxwell-binomial distribution captured the change  
2434 in association at stimulus onset better than the correlation coefficient. The extremely small  
2435 bin width artificially shrunk the correlation coefficient to the point where this measurement  
2436 didn't detect any correlated activity. But the association parameter of the COMb distribution  
2437 detected some positive association between the neurons at stimulus onset. So, for particularly  
2438 short time bins, where neurons can be treated as Bernoulli random variables, the Conway-  
2439 Maxwell-binomial distribution is a good way to capture correlated behaviour. There are  
2440 other measurements for capturing association to which this distribution should be compared.  
2441 Cross-correlograms could be used for some measure of synchrony, for example.

2442 Finally, we replicated a famous finding of Churchland et al. (2010) relating to the quench-  
2443 ing of neural variability at stimulus onset, thereby finding a parallel between this reduction  
2444 in the Fano factor and a reduction in the association parameter of the COMb distribution.

2445 We showed that computational neuroscientists can make progress by being inventive with  
2446 their statistical models. A similar distribution to investigate would be the Conway-Maxwell-  
2447 Poisson distribution. This is similar to the standard Poisson distribution, but with an addi-  
2448 tional parameter that allows for over- or under- dispersion relative to a Poisson distribution.  
2449 This might be ideal for modelling firing rates of individual neurons. Some interaction be-  
2450 tween the fitted parameters could capture the association between neurons.

2451 There is one technology that has the potential to take over from both electrophysiology  
2452 and calcium imaging. The technique of voltage imaging has become more useful in recent  
2453 years. The aim for neuroscience would be to develop a voltage imaging dye or protein that

2454 images the membrane potential of a neuron with enough spatial and temporal resolution to  
2455 detect action potentials. Genetically encoded voltage indicators have been developed, and  
2456 enable targeting of specific neuronal ensembles. But their spatial resolution is not yet high  
2457 enough to single out individual cells (Bando et al., 2019). These indicators have the potential  
2458 to take over from calcium imaging, and if imaging deep within the brain becomes possible,  
2459 electrophysiology could also be replaced. This is specualtaion, but the potential is there.



2460 

# Bibliography

- 2461 Allen, William E. et al. (2019). “Thirst regulates motivated behavior through modulation of  
 2462 brainwide neural population dynamics”. In: *Science* 364.6437. ISSN: 0036-8075. DOI:  
 2463 [10.1126/science.aav3932](https://doi.org/10.1126/science.aav3932). eprint: <https://science.sciencemag.org/content/364/6437/eaav3932.full.pdf>. URL: <https://science.sciencemag.org/content/364/6437/eaav3932>.
- 2464 Baadel, S., F. Thabtah, and J. Lu (2016). “Overlapping clustering: A review”. In: *2016 SAI Computing Conference (SAI)*, pp. 233–237. DOI: [10.1109/SAI.2016.7555988](https://doi.org/10.1109/SAI.2016.7555988).
- 2465 Baldassano, Christopher et al. (2017). “Discovering Event Structure in Continuous Narrative Perception and Memory”. In: *Neuron* 95.3, 709 –721.e5. ISSN: 0896-6273. DOI: <https://doi.org/10.1016/j.neuron.2017.06.041>. URL: <http://www.sciencedirect.com/science/article/pii/S0896627317305937>.
- 2466 Bando, Yuki et al. (2019). “Genetic voltage indicators”. In: *BMC Biology* 17.1, p. 71. ISSN:  
 2467 1741-7007. DOI: [10.1186/s12915-019-0682-0](https://doi.org/10.1186/s12915-019-0682-0). URL: <https://doi.org/10.1186/s12915-019-0682-0>.
- 2468 Bartol, Thomas M. et al. (2015). “Computational reconstitution of spine calcium transients from individual proteins”. In: *Frontiers in Synaptic Neuroscience* 7, p. 17. ISSN: 1663-  
 2469 3563. DOI: [10.3389/fnsyn.2015.00017](https://doi.org/10.3389/fnsyn.2015.00017). URL: <https://www.frontiersin.org/article/10.3389/fnsyn.2015.00017>.
- 2470 Berens, Philipp et al. (May 2018). “Community-based benchmarking improves spike rate inference from two-photon calcium imaging data”. In: *PLOS Computational Biology* 14.5, pp. 1–13. DOI: [10.1371/journal.pcbi.1006157](https://doi.org/10.1371/journal.pcbi.1006157). URL: <https://doi.org/10.1371/journal.pcbi.1006157>.
- 2471 Bezanson, Jeff et al. (Sept. 2012). “Julia: A Fast Dynamic Language for Technical Computing”. In: *MIT*.
- 2472 Buccino, Alessio P. et al. (2019). “SpikeInterface, a unified framework for spike sorting”. In: *bioRxiv*. DOI: [10.1101/796599](https://doi.org/10.1101/796599). eprint: <https://www.biorxiv.org/content/early/2019/10/07/796599.full.pdf>. URL: <https://www.biorxiv.org/content/early/2019/10/07/796599>.

- 2489 Chen, Tsai-Wen et al. (July 2013). “Ultrasensitive fluorescent proteins for imaging neuronal  
2490 activity”. In: *Nature* 499, 295–300. DOI: [10.1038/nature12354](https://doi.org/10.1038/nature12354). URL: <https://doi.org/10.1038/nature12354>.
- 2492 Churchland, Mark M. et al. (2010). “Stimulus onset quenches neural variability: a widespread  
2493 cortical phenomenon”. eng. In: *Nature neuroscience* 13.3. 20173745[pmid], pp. 369–378.  
2494 ISSN: 1546-1726. DOI: [10.1038/nn.2501](https://doi.org/10.1038/nn.2501). URL: <https://pubmed.ncbi.nlm.nih.gov/20173745>.
- 2496 Cohen, Marlene R. and Adam Kohn (2011). “Measuring and interpreting neuronal correla-  
2497 tions”. In: *Nature Neuroscience* 14.7, pp. 811–819. ISSN: 1546-1726. DOI: [10.1038/nn.2842](https://doi.org/10.1038/nn.2842). URL: <https://doi.org/10.1038/nn.2842>.
- 2499 Cohen, Marlene R. and John H. R. Maunsell (2009). “Attention improves performance pri-  
2500 marily by reducing interneuronal correlations”. eng. In: *Nature neuroscience* 12.12. 19915566[pmid],  
2501 pp. 1594–1600. ISSN: 1546-1726. DOI: [10.1038/nn.2439](https://doi.org/10.1038/nn.2439). URL: <https://pubmed.ncbi.nlm.nih.gov/19915566>.
- 2503 Dana, Hod et al. (Sept. 2014). “Thy1-GCaMP6 Transgenic Mice for Neuronal Population  
2504 Imaging In Vivo”. In: *PloS one* 9, e108697. DOI: [10.1371/journal.pone.0108697](https://doi.org/10.1371/journal.pone.0108697).
- 2506 deCharms, R. Christopher and Michael M. Merzenich (1996). “Primary cortical represen-  
2507 tation of sounds by the coordination of action-potential timing”. In: *Nature* 381.6583,  
2508 pp. 610–613. ISSN: 1476-4687. DOI: [10.1038/381610a0](https://doi.org/10.1038/381610a0). URL: <https://doi.org/10.1038/381610a0>.
- 2510 Deneux, Thomas et al. (July 2016). “Accurate spike estimation from noisy calcium signals  
2511 for ultrafast three-dimensional imaging of large neuronal populations in vivo”. In: *Nature  
2512 Communications* 7.1. DOI: [10.1038/ncomms12190](https://doi.org/10.1038/ncomms12190). URL: <https://doi.org/10.1038/ncomms12190>.
- 2514 Dombeck, Daniel A. et al. (2010). “Functional imaging of hippocampal place cells at cellular  
2515 resolution during virtual navigation”. In: *Nature Neuroscience* 13.11, pp. 1433–1440.  
2516 ISSN: 1546-1726. DOI: [10.1038/nn.2648](https://doi.org/10.1038/nn.2648). URL: <https://doi.org/10.1038/nn.2648>.
- 2518 Faas, Guido C. et al. (2011). “Calmodulin as a direct detector of Ca<sup>2+</sup> signals”. In: *Nature  
2519 Neuroscience* 14.3, pp. 301–304. ISSN: 1546-1726. DOI: [10.1038/nn.2746](https://doi.org/10.1038/nn.2746). URL:  
2520 <https://doi.org/10.1038/nn.2746>.
- 2521 Fiala, John C. and Kristen M. Harris (1999). *Dendrite Structure*.

- 2522 Flach, Boris (Sept. 2013). “A Class of Random Fields on Complete Graphs with Tractable  
2523 Partition Function”. In: *IEEE transactions on pattern analysis and machine intelligence*  
2524 35, pp. 2304–6. DOI: [10.1109/TPAMI.2013.99](https://doi.org/10.1109/TPAMI.2013.99).
- 2525 Forney, G. D. (1973). “The viterbi algorithm”. In: *Proceedings of the IEEE* 61.3, pp. 268–  
2526 278. ISSN: 1558-2256. DOI: [10.1109/PROC.1973.9030](https://doi.org/10.1109/PROC.1973.9030).
- 2527 Fosdick, Bailey et al. (Aug. 2016). “Configuring Random Graph Models with Fixed Degree  
2528 Sequences”. In: *SIAM Review* 60. DOI: [10.1137/16M1087175](https://doi.org/10.1137/16M1087175).
- 2529 Friedrich, Johannes and Liam Paninski (2016). “Fast Active Set Methods for Online Spike  
2530 Inference from Calcium Imaging”. In: *Advances in Neural Information Processing Systems* 29. Ed. by D. D. Lee et al. Curran Associates, Inc., pp. 1984–1992. URL: <http://papers.nips.cc/paper/6505-fast-active-set-methods-for-online-spike-inference-from-calcium-imaging.pdf>.
- 2534 Ganmor, Elad, Ronen Segev, and Elad Schneidman (2011). “Sparse low-order interaction  
2535 network underlies a highly correlated and learnable neural population code”. In: *Proceedings of the National Academy of Sciences* 108.23, pp. 9679–9684. ISSN: 0027-8424. DOI:  
2536 [10.1073/pnas.1019641108](https://doi.org/10.1073/pnas.1019641108). eprint: <https://www.pnas.org/content/108/23/9679.full.pdf>. URL: <https://www.pnas.org/content/108/23/9679>.
- 2540 Girard, P., J. M. Hupé, and J. Bullier (2001). “Feedforward and Feedback Connections Be-  
2541 tween Areas V1 and V2 of the Monkey Have Similar Rapid Conduction Velocities”. In:  
2542 *Journal of Neurophysiology* 85.3. PMID: 11248002, pp. 1328–1331. DOI: [10.1152/jn.2001.85.3.1328](https://doi.org/10.1152/jn.2001.85.3.1328). eprint: <https://doi.org/10.1152/jn.2001.85.3.1328>. URL: <https://doi.org/10.1152/jn.2001.85.3.1328>.
- 2545 Greenberg, David et al. (Nov. 2018). “Accurate action potential inference from a calcium  
2546 sensor protein through biophysical modeling.” in: DOI: [10.1101/479055](https://doi.org/10.1101/479055).
- 2547 Gründemann, Jan et al. (2019). “Amygdala ensembles encode behavioral states”. In: *Science*  
2548 364.6437. ISSN: 0036-8075. DOI: [10.1126/science.aav8736](https://doi.org/10.1126/science.aav8736). eprint: <https://science.sciencemag.org/content/364/6437/eaav8736.full.pdf>. URL: <https://science.sciencemag.org/content/364/6437/eaav8736>.
- 2552 Hodgkin, A. L. and A. F. Huxley (1939). “Action Potentials Recorded from Inside a Nerve Fi-  
2553 bre”. In: *Nature* 144.3651, pp. 710–711. ISSN: 1476-4687. DOI: [10.1038/144710a0](https://doi.org/10.1038/144710a0).  
2554 URL: <https://doi.org/10.1038/144710a0>.

- 2555 Humphries, Mark et al. (Jan. 2019). “Spectral rejection for testing hypotheses of structure in  
2556 networks”. In:
- 2557 Humphries, Mark D. (2011). “Spike-Train Communities: Finding Groups of Similar Spike  
2558 Trains”. In: *Journal of Neuroscience* 31.6, pp. 2321–2336. ISSN: 0270-6474. DOI: [10.1523/JNEUROSCI.2853-10.2011](#). eprint: <https://www.jneurosci.org/content/31/6/2321.full.pdf>. URL: <https://www.jneurosci.org/content/31/6/2321>.
- 2562 Jun, James J. et al. (2017). “Fully integrated silicon probes for high-density recording of  
2563 neural activity”. In: *Nature* 551.7679, pp. 232–236. ISSN: 1476-4687. DOI: [10.1038/nature24636](#). URL: <https://doi.org/10.1038/nature24636>.
- 2565 Kadane, Joseph B. (June 2016). “Sums of Possibly Associated Bernoulli Variables: The  
2566 Conway–Maxwell-Binomial Distribution”. In: *Bayesian Anal.* 11.2, pp. 403–420. DOI:  
2567 [10.1214/15-BA955](#). URL: <https://doi.org/10.1214/15-BA955>.
- 2568 Kilhoffer, Marie-Claude et al. (Sept. 1992). “Use of Engineered Proteins With Internal Tryp-  
2569 tophean Reporter Groups and Perturbation Techniques to Probe the Mechanism of Ligand-  
2570 Protein Interactions: Investigation of the Mechanism of Calcium Binding to Calmod-  
2571 ulin”. In: *Biochemistry* 31.34, pp. 8098–8106. DOI: [10.1021/bi00149a046](#). URL:  
2572 <https://doi.org/10.1021/bi00149a046>.
- 2573 Koch, Christoff (1999). *Biophysics of Computation: Information Processing in Single Neu-  
2574 rons*. Oxford University Press. ISBN: ISBN 0-19-510491-9.
- 2575 Kolaczyk, Eric and Haiying Huang (Sept. 2010). “Multiscale Statistical Models for Hier-  
2576 archical Spatial Aggregation”. In: *Geographical Analysis* 33, pp. 95 –118. DOI: [10.1111/j.1538-4632.2001.tb00439.x](#).
- 2578 Lee, Suk-HO et al. (July 2000). “Differences in Ca2+ buffering properties between excitatory  
2579 and inhibitory hippocampal neurons from the rat”. In: *The Journal of Physiology* 525.  
2580 DOI: [10.1111/j.1469-7793.2000.t01-3-00405.x](#).
- 2581 Litwin-Kumar, Ashok, Maurice Chacron, and Brent Doiron (Sept. 2012). “The Spatial Struc-  
2582 ture of Stimuli Shapes the Timescale of Correlations in Population Spiking Activity”.  
2583 In: *PLoS computational biology* 8, e1002667. DOI: [10.1371/journal.pcbi.1002667](#).
- 2585 Maravall, M et al. (May 2000). “Estimating intracellular calcium concentrations and buffer-  
2586 ing without wavelength ratioing”. In: *Biophysical Journal* 78.5, pp. 2655–2667. DOI:  
2587 [10.1016/S0006-3495\(00\)76809-3](#). URL: [https://doi.org/10.1016/S0006-3495\(00\)76809-3](https://doi.org/10.1016/S0006-3495(00)76809-3).

- 2589 Maugis, Pa (Jan. 2014). “Event Conditional Correlation: Or How Non-Linear Linear Depen-  
2590 dence Can Be”. In:
- 2591 Meilă, Marina (2007). “Comparing clusterings—an information based distance”. In: *Journal*  
2592 of *Multivariate Analysis* 98.5, pp. 873 –895. ISSN: 0047-259X. DOI: <https://doi.org/10.1016/j.jmva.2006.11.013>. URL: <http://www.sciencedirect.com/science/article/pii/S0047259X06002016>.
- 2595 Murray, John D. et al. (2014). “A hierarchy of intrinsic timescales across primate cortex”.  
2596 In: *Nature Neuroscience* 17.12, pp. 1661–1663. ISSN: 1546-1726. DOI: [10.1038/nn.3862](https://doi.org/10.1038/nn.3862). URL: <https://doi.org/10.1038/nn.3862>.
- 2598 Neher, E. and G. J. Augustine (1992). “Calcium gradients and buffers in bovine chromaffin  
2599 cells”. eng. In: *The Journal of physiology* 450. 1331424[pmid], pp. 273–301. ISSN: 0022-  
2600 3751. DOI: [10.1113/jphysiol.1992.sp019127](https://doi.org/10.1113/jphysiol.1992.sp019127). URL: <https://pubmed.ncbi.nlm.nih.gov/1331424>.
- 2602 O’Donnell, Cian et al. (Jan. 2017). “The population tracking model: a simple, scalable statis-  
2603 tical model for neural population data”. English. In: *Neural Computation* 29.1, pp. 50–  
2604 93. ISSN: 0899-7667. DOI: [10.1162/NECO\\_a\\_00910](https://doi.org/10.1162/NECO_a_00910).
- 2605 Okun, Michael et al. (2015). “Diverse coupling of neurons to populations in sensory cortex”.  
2606 In: *Nature* 521.7553, pp. 511–515. ISSN: 1476-4687. DOI: [10.1038/nature14273](https://doi.org/10.1038/nature14273).  
2607 URL: <https://doi.org/10.1038/nature14273>.
- 2608 Ouzounov, Dimitre G. et al. (2017). “In vivo three-photon imaging of activity of GCaMP6-  
2609 labeled neurons deep in intact mouse brain”. eng. In: *Nature methods* 14.4. 28218900[pmid],  
2610 pp. 388–390. ISSN: 1548-7105. DOI: [10.1038/nmeth.4183](https://doi.org/10.1038/nmeth.4183). URL: <https://pubmed.ncbi.nlm.nih.gov/28218900>.
- 2612 Patterson, Carlyn A. et al. (2014). “Similar adaptation effects in primary visual cortex and  
2613 area MT of the macaque monkey under matched stimulus conditions”. In: *Journal of Neu-  
2614 rophysiology* 111.6. PMID: 24371295, pp. 1203–1213. DOI: [10.1152/jn.00030.2013](https://doi.org/10.1152/jn.00030.2013). eprint: <https://doi.org/10.1152/jn.00030.2013>. URL: <https://doi.org/10.1152/jn.00030.2013>.
- 2617 Peron, Simon P. et al. (2015). “A Cellular Resolution Map of Barrel Cortex Activity during  
2618 Tactile Behavior”. In: *Neuron* 86.3, pp. 783–799. ISSN: 0896-6273. DOI: [10.1016/j.neuron.2015.03.027](https://doi.org/10.1016/j.neuron.2015.03.027). URL: <https://doi.org/10.1016/j.neuron.2015.03.027>.
- 2621 Pnevmatikakis, E.A. et al. (Jan. 2016). “Simultaneous Denoising, Deconvolution, and Demix-  
2622 ing of Calcium Imaging Data”. In: *Neuron* 89.2, pp. 285–299. DOI: [10.1016/j.neuron.2016.09.021](https://doi.org/10.1016/j.neuron.2016.09.021).

- 2623       neuron. 2015. 11. 037. URL: <https://doi.org/10.1016/j.neuron.2015.11.037>.
- 2624
- 2625 Pnevmatikakis, Eftychios et al. (Nov. 2013). “Bayesian spike inference from calcium imaging data”. In: *Conference Record - Asilomar Conference on Signals, Systems and Computers*.  
2626  
2627 DOI: [10.1109/ACSSC.2013.6810293](https://doi.org/10.1109/ACSSC.2013.6810293).
- 2628 Pnevmatikakis, Eftychios et al. (Sept. 2014). “A structured matrix factorization framework  
2629 for large scale calcium imaging data analysis”. In:
- 2630 Schneidman, Elad et al. (2006). “Weak pairwise correlations imply strongly correlated net-  
2631 work states in a neural population”. eng. In: *Nature* 440.7087. 16625187[pmid], pp. 1007–  
2632 1012. ISSN: 1476-4687. DOI: [10.1038/nature04701](https://doi.org/10.1038/nature04701). URL: <https://pubmed.ncbi.nlm.nih.gov/16625187>.
- 2633
- 2634 Shannon, C. E. (1948). “A Mathematical Theory of Communication”. In: *Bell System Techni-  
2635 cal Journal* 27.3, pp. 379–423. DOI: [10.1002/j.1538-7305.1948.tb01338.x](https://doi.org/10.1002/j.1538-7305.1948.tb01338.x).  
2636 eprint: <https://onlinelibrary.wiley.com/doi/pdf/10.1002/j.1538-7305.1948.tb01338.x>. URL: <https://onlinelibrary.wiley.com/doi/abs/10.1002/j.1538-7305.1948.tb01338.x>.
- 2637
- 2638 Shimazaki, Hideaki et al. (2012). “State-space analysis of time-varying higher-order spike  
2639 correlation for multiple neural spike train data”. eng. In: *PLoS computational biology* 8.3.  
2640 22412358[pmid], e1002385–e1002385. ISSN: 1553-7358. DOI: [10.1371/journal.pcbi.1002385](https://doi.org/10.1371/journal.pcbi.1002385). URL: <https://pubmed.ncbi.nlm.nih.gov/22412358>.
- 2641
- 2642 Staude, Benjamin, Sonja Grün, and Stefan Rotter (2010). “Higher-Order Correlations and  
2643 Cumulants”. In: *Analysis of Parallel Spike Trains*. Ed. by Sonja Grün and Stefan Rotter.  
2644 Boston, MA: Springer US, pp. 253–280. ISBN: 978-1-4419-5675-0. DOI: [10.1007/978-1-4419-5675-0\\_12](https://doi.org/10.1007/978-1-4419-5675-0_12). URL: [https://doi.org/10.1007/978-1-4419-5675-0\\_12](https://doi.org/10.1007/978-1-4419-5675-0_12).
- 2645
- 2646 Stein, Astrid von and Johannes Sarnthein (2000). “Different frequencies for different scales  
2647 of cortical integration: from local gamma to long range alpha/theta synchronization”. In:  
2648 *International Journal of Psychophysiology* 38.3, pp. 301 –313. ISSN: 0167-8760. DOI:  
2649 [https://doi.org/10.1016/S0167-8760\(00\)00172-0](https://doi.org/10.1016/S0167-8760(00)00172-0). URL: <http://www.sciencedirect.com/science/article/pii/S0167876000001720>.
- 2650
- 2651 Steinmetz, Nick, Matteo Carandini, and Kenneth D. Harris (2019). ”Single Phase3” and  
2652 ”Dual Phase3” Neuropixels Datasets. DOI: [10.6084/m9.figshare.7666892.v2](https://doi.org/10.6084/m9.figshare.7666892.v2). URL: [https://figshare.com/articles/dataset/\\_Single\\_Phase3\\_Neuropixels\\_Dataset/7666892/2](https://figshare.com/articles/dataset/_Single_Phase3_Neuropixels_Dataset/7666892/2).
- 2653
- 2654
- 2655
- 2656

- 2657 Steinmetz, Nick et al. (Mar. 2019). “Eight-probe Neuropixels recordings during sponta-  
2658 neous behaviors”. In: DOI: [10.25378/janelia.7739750.v4](https://doi.org/10.25378/janelia.7739750.v4). URL: [https://janelia.figshare.com/articles/Eight-probe\\_Neuropixels\\_recordings\\_during\\_spontaneous\\_behaviors/7739750](https://janelia.figshare.com/articles/Eight-probe_Neuropixels_recordings_during_spontaneous_behaviors/7739750).
- 2661 Stringer, Carsen et al. (2019). “Spontaneous behaviors drive multidimensional, brainwide ac-  
2662 tivity”. In: *Science* 364.6437. ISSN: 0036-8075. DOI: [10.1126/science.aav7893](https://doi.org/10.1126/science.aav7893).  
2663 eprint: <https://science.sciencemag.org/content/364/6437/eaav7893.full.pdf>. URL: <https://science.sciencemag.org/content/364/6437/eaav7893>.
- 2666 Tada, Mayumi et al. (2014). “A highly sensitive fluorescent indicator dye for calcium imag-  
2667 ing of neural activity in vitro and in vivo”. In: *European Journal of Neuroscience* 39.11,  
2668 pp. 1720–1728. DOI: [10.1111/ejn.12476](https://doi.org/10.1111/ejn.12476). eprint: <https://onlinelibrary.wiley.com/doi/pdf/10.1111/ejn.12476>. URL: <https://onlinelibrary.wiley.com/doi/abs/10.1111/ejn.12476>.
- 2671 Tian, Lin et al. (2009). “Imaging neural activity in worms, flies and mice with improved  
2672 GCaMP calcium indicators”. eng. In: *Nature methods* 6.12. 19898485[pmid], pp. 875–  
2673 881. ISSN: 1548-7105. DOI: [10.1038/nmeth.1398](https://doi.org/10.1038/nmeth.1398). URL: <https://pubmed.ncbi.nlm.nih.gov/19898485>.
- 2675 Tkačik, Gašper et al. (2014). “Searching for collective behavior in a large network of sen-  
2676 sory neurons”. eng. In: *PLoS computational biology* 10.1. 24391485[pmid], e1003408–  
2677 e1003408. ISSN: 1553-7358. DOI: [10.1371/journal.pcbi.1003408](https://doi.org/10.1371/journal.pcbi.1003408). URL:  
2678 <https://pubmed.ncbi.nlm.nih.gov/24391485>.
- 2679 Treves, Alessandro and Stefano Panzeri (1995). “The Upward Bias in Measures of Informa-  
2680 tion Derived from Limited Data Samples”. In: *Neural Computation* 7.2, pp. 399–407.  
2681 DOI: [10.1162/neco.1995.7.2.399](https://doi.org/10.1162/neco.1995.7.2.399). eprint: <https://doi.org/10.1162/neco.1995.7.2.399>. URL: <https://doi.org/10.1162/neco.1995.7.2.399>.
- 2684 Vinh, Nguyen Xuan, Julien Epps, and James Bailey (Dec. 2010). “Information Theoretic  
2685 Measures for Clusterings Comparison: Variants, Properties, Normalization and Correc-  
2686 tion for Chance”. In: *J. Mach. Learn. Res.* 11, 2837–2854. ISSN: 1532-4435.
- 2687 Vogelstein, Joshua T. et al. (Oct. 2010). “Fast nonnegative deconvolution for spike train infer-  
2688 ence from population calcium imaging”. In: *Journal of neurophysiology* 104.6, 295–300.  
2689 DOI: [10.1152/jn.01073.2009](https://doi.org/10.1152/jn.01073.2009). URL: <https://dx.doi.org/10.1152%2Fjn.01073.2009>.

- 2691 Wierzynski, "Casimir M. et al. (2009). ““State-Dependent Spike-Timing Relationships be-  
2692 tween Hippocampal and Prefrontal Circuits during Sleep””. In: "Neuron" "61"."4", "587  
2693 –596". ISSN: "0896-6273". DOI: "<https://doi.org/10.1016/j.neuron.2009.01.011>". URL: "<http://www.sciencedirect.com/science/article/pii/S0896627309000786>".
- 2696 Zariwala, Hatim A. et al. (2012). “A Cre-dependent GCaMP3 reporter mouse for neuronal  
2697 imaging in vivo”. eng. In: *The Journal of neuroscience : the official journal of the Society  
2698 for Neuroscience* 32.9. 22378886[pmid], pp. 3131–3141. ISSN: 1529-2401. DOI: [10.1523/JNEUROSCI.4469-11.2012](https://doi.org/10.1523/JNEUROSCI.4469-11.2012). URL: <https://pubmed.ncbi.nlm.nih.gov/22378886>.
- 2701 Zou, Hui and Trevor Hastie (2005). “Regularization and variable selection via the Elastic  
2702 Net”. In: *Journal of the Royal Statistical Society, Series B* 67, pp. 301–320.
- 2703 Éltes, Tímea et al. (2019). “Improved spike inference accuracy by estimating the peak am-  
2704 plitude of unitary [Ca<sub>2+</sub>] transients in weakly GCaMP6f-expressing hippocampal pyra-  
2705 midal cells”. In: *The Journal of Physiology* 597.11, pp. 2925–2947. DOI: [10.1113/JP277681](https://doi.org/10.1113/JP277681). eprint: <https://physoc.onlinelibrary.wiley.com/doi/pdf/10.1113/JP277681>. URL: <https://physoc.onlinelibrary.wiley.com/doi/abs/10.1113/JP277681>.